LANCASTER UNIVERSITY

Investigations into Colour Reconnection Effects in W^+W^- Events from 183GeV to 202GeV with the ALEPH Detector at LEP2.

Nicholas Andrew Robertson *B.Sc.(Hons)*

August 1st, 2000

Thesis submitted in partial fulfillment of the requirements for the degree of Doctor of Philosophy. No part of this thesis has been, or will be, submitted elsewhere.

Abstract

WW events recorded by the ALEPH detector from 183GeV to 202GeV have been tested for the effects of colour reconnection between the two hadronically decaying systems. Average charged track event multiplicities and fragmentation functions from fully hadronic WW events were tested against semi-leptonic data as well as Monte Carlo, with and without the phenomena present. All of the Monte Carlo simulations were found to be compatible with the data, therefore no evidence for, or against colour reconnection's existence was observed with the present level of statistics. Further studies were instigated into a new technique, believed to be more sensitive to colour reconnection effects, which used Lorentz invariant particle distributions. It was concluded that this preliminary study 'shows promise'.

Acknowledgments

First I would like to thank the Particle Physics group here at Lancaster for giving me the opportunity to do this PhD, and PPARC for the financial assistance. I would especial like to thank Roger ('The Boss') for being not only a superb supervisor, but becoming a good friend too and always having time to explain the physics, again (and sign all those forms). I also wish to thank other members of the group (past and present) who helped me so much when I first arrived, and Terry, Gareth, Tim, and Rob for various, physics, computing, and statistical based discussions, and of cause Alex 'The Guru' Finch for knowing/fixing everything. How could I possibly leave out the other students/drinking partners like, the utterly disgraceful Paul 'Lift Coiler' Buck for many an evening of nonsense, Gareth 'The Big G' for taking that damn bar of my hands(!), and Glen, see I told you I'd finish first.

During my time at CERN I was fortunate enough to work with many physicists and I would like to thank them: Bolek for all his assistance during my analysis and Glen Cowan too in the early stages. I would also like to thank other members of the Colour Reconnection group for working on the subject, and the members of the WW group for making the analysis so much more enjoyable. And of cause all the people who donated their computer code and explained how to use it, such as Evelyn, Helenka (a fellow May sixer), and anyone else I forgot.

I also made a lot of friendships while in Geneva, so thanks to all the people that kept me (in)sane, such as Jon 'Horrible' Hays for buying a playstation, and being such a good mate when things went wrong. Andy, for always talking about motorbikes and Leanne (¨I can see the pub from here¨), good luck guys!! Futyand for always knowing the weather, Parsonsh for being so loud and all the other guilty parties who went skiing (SKI!), sat in my flat drinking tea, or used zwrite constantly.

I finally want to thank all my other friends, before my time in Geneva, which are now scattered around the country and I am sorry for neglecting you all recently, all my friends from Graduate Bar after my return and of course, Sergeant Dave Velcro, Warwick and Carla, for being especially good friends, and Marina for going through her PhD blues simultaneously - enjoy Holland!

Lastly but obviously far from least, I would like to thank my Parents and brother Tim, for always being there and listening when I need them. And Sue, the girl who really has kept me going for the last eight months, by being so truly wonderful, patient, supportive and supplying me with endless cups of tea and bacon sarnies and even reading this thesis, twice! Gosh, its great having a girlfriend who studied Linguistics!

-N-

Contents

List of Figures

List of Tables

Chapter 1

The Standard Model and Colour Reconnection

1.1 Introduction

This chapter begins by describing the fundamental ideas behind the Standard Model of elementary particles, further details can be found in [1, 2, 3]. Subsequently it concentrates on the physics examined by the LEP collider and considers how the W boson can be used to investigate an element of Quantum Chromodynamics known as Colour Reconnection. It then goes on to explain the phenomena, and philosophy of examining its effects. Later chapters will detail the tools and methods used by the author in the search for colour reconnection, as well as presenting the results obtained.

1.2 The assiduity of man.

Throughout recorded history, man has been slowly but diligently increasing his knowledge of the world around him, driven by the fundamental questions of why and how. Certainly within the last two hundred years, many great achievements have been accomplished which have led to a greater understanding of the universe, which we are a part of. Our knowledge of the microscopic world has now passed far beyond the stage of atoms and molecules which were believed to be fundamental at the end of the 19^{th} Century. The electron was discovered by J.J. Thompson [4], and later, the atomic nucleus by Rutherford [4]; both used the newly combined theories of electrostatics and magnetism by Maxwell [5], in the form of electromagnetism, to assist their efforts. This, subsequently paved the way for further discoveries early in the 20^{th} Century, such as the proton and neutron. In addition, Quantum Mechanics was developing alongside these discoveries, which assisted in the understanding of this new and exciting microscopic world. By the 1960's, a further level of subatomic particles was being investigated, namely the quark. These quarks made up the protons and neutrons, which made up the atomic nucleus, which together with the electron made up the atoms, which made up the molecules, which make up the objects we see in the macroscopic world.

After centuries of perseverance and diligent scrutiny, the assiduity of man finally arrived at the Standard Model of Particle Physics [1]. This was an accomplishment unsurpassed in its genius, and is at present the limit of mankind's knowledge of all that is incomprehensibly tiny.

Family	**Particle**	**Symbol**	**Charge**	**Mass(MeV/c^2)**
Quarks	up	u	$+\frac{2}{3}$	1.5 - 5
	down	d	$-\frac{1}{3}$	3 - 9
	charm	c	$+\frac{2}{3}$	1100 - 1400
	strange	s	$-\frac{1}{3}$	60 - 170
	top	t	$+\frac{2}{3}$	173.8 $\pm$ 5.2 GeV
	bottom	b	$-\frac{1}{3}$	4100 - 4400
Leptons	electron	e	-1	0.511
	electron neutrino	ν_e	0	$< 10^{-5}$
	muon	μ	-1	105.66
	muon neutrino	ν_μ	0	< 0.17
	tau	τ	-1	1777.05 $\pm$ 0.29
	tau neutrino	ν_τ	0	< 18.2

Table 1.1: *Fundamental fermions of the Standard Model*

Force	**No. of Bosons**	**Boson**	**Charge**	**Mass(GeV/c^2)**
Electromagnetic	1	photon(γ)	0	0
Weak	3	W^+,W^-	$\pm$1	80.41 $\pm$ 0.10
		Z^0	0	91.187 $\pm$ 0.007
Strong	8	gluon(g)	0	0

Table 1.2: *Fundamental forces of the Standard Model*

1.3 Quarks, Leptons, Bosons and Forces

1.3.1 The particles that matter

At present, the Standard Model contains two different types of fundamental particles: the matter building blocks are called fermions because they have spin equal to $\frac{1}{2}$, and the gauge bosons have integer spin and mediate the forces. Table 1.1 lists all the fundamental fermions of the Standard Model, Table 1.2 lists the gauge bosons.

There are two types of fermion: the quarks and the leptons. There are believed to be six quark flavours, and six leptons. Each fermion has an anti-particle, which has opposite quantum numbers. The three neutrinos are a sub-group of the leptons and are believed to have a near zero mass, while the other three have finite masses. Quarks are the only particles to interact with the strong force because they have colour charge. The quarks are always confined into larger colourless particles called hadrons, for example, the proton. There are two forms of hadron: mesons and baryons. A meson is composed of a quark anti-quark pair, of any flavour, while a baryon is composed of any three quarks.

1.3.2 The Four Forces of the Apocalypse

The four forces and their gauge bosons are as follows:

- **Electromagnetic**. The gauge boson that mediates the force is the photon, and this has infinite range. Any particle with an electric charge is susceptible to electromagnetism. The interactions are explained by the theory of Quantum Electrodynamics (QED), which was the original gauge theory [1].

- **Weak.** There are three gauge bosons which mediate the weak force: the electrically charged W^+ and W^- particles, and the neutral Z^0. These particles are all massive and only travel short distances. All fundamental

fermions are susceptible to the weak force, and during the exchange of a W particle, the fermions involved will actually change into another particle. The origin of investigations into the interaction lie in radioactive decays. At high energies, the weak force and the electromagnetic force are united and can be explained by the Electroweak gauge theory [1].

- **Strong.** This is the force that holds the quarks together to form larger hadronic matter such as atomic nucleons. Quarks possess one of three colour charges, and exchange gluons as mediators. The gluons also carry a colour charge, and therefore interact with themselves, which reduces the effective distance over which the force acts, to 10^{-15}m. Quantum Chromodynamics (QCD) [1] is the non-abelian gauge theory which explains the interaction.

- **Gravity.** The fourth force, Gravity, is explained by Einstein's Theory of General Relativity [6], this though is not incorporated into the Standard Model and consequently will not be discussed any further in this work.

1.4 Quantum Electrodynamics and Gauge Invariance

The description of the three interactions of the Standard Model are in terms of Quantum Field Theory [7], which combines Quantum Mechanics and Special Relativity [4] in order to explain the interactions between two particles. Quantum numbers and 4-momentum are transferred between fundamental fermions by the exchange of gauge bosons. The fermion must possess the property that allows the interaction to occur, for example, an electron possesses an electric charge, thus it can interact electromagnetically via the exchange of a photon (this being the gauge particle of QED) with another electron. The electrons are viewed as electromagnetic currents, and it is the electric field between the currents that conjures the photon from the vacuum, therefore allowing the electrons to be

perturbed from their original path. To understand how this occurs, we must first consider some fundamental concepts in Physics.

Conservation laws and symmetries are very important notions in Particle Physics. Every exact conservation law corresponds to a symmetry in the physical description of the system. If a system is invariant under a translation or rotation, then following either a quantum or classical mechanical argument, this will lead directly to the conservation of linear or angular momentum. This is known as a global invariance.

Moving to the case for QED, it is global invariance under a phase change of the wave function which tells us that the charge current is conserved. However, when we consider a local phase transformation, such that the transformation of the system now depends on position, we find that in order to produce an invariance of the wave function, we must introduce a vector field called the gauge field (which can be interpreted as the photon propagator). Now, in the macroscopic world, we only observe the real physical properties of the E and B field and not the absolute potentials used to describe them. We have just introduced an arbitrary potential, hence, we are able to choose its value as long as the final result remains unchanged, this is called gauge invariance. It is for this reason that QED is called a gauge theory.

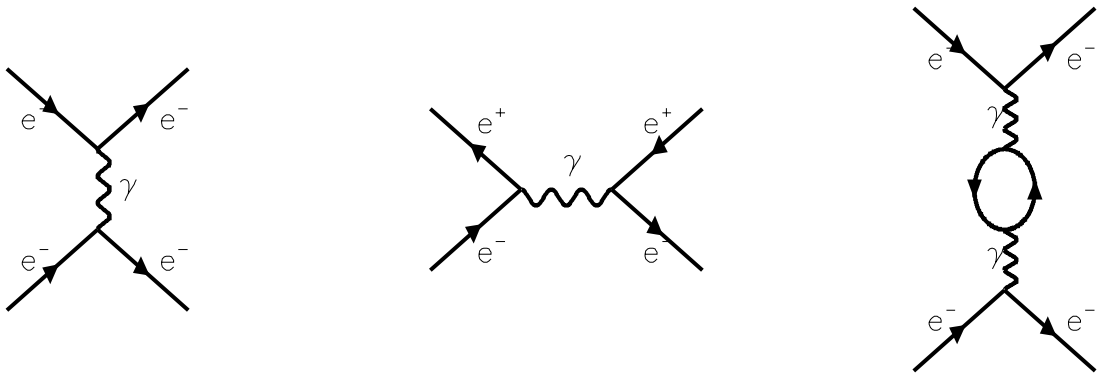

Figure 1.1: *Fundamental Feynman diagrams of QED.*

QED has further interesting features embedded in its theoretical framework, of which electron-positron (e^+e^-) annihilation is noteworthy, see the Feynman di-

agram in the middle of Figure 1.1. A positron is the anti-particle of the electron, which means that essentially it is an electron with a positive charge. Feynman however, interpreted these positrons as negative energy electrons flowing backwards in time, and predicted the phenomenon of an electron scattering from a photon backwards in time, so that to us it looks like a positron and electron meeting and then annihilating into a photon. This is the driving force behind the building of machines such as LEP, which collides electrons and positrons.

Quantum Field Theory predicts that a photon is subject to vacuum polarisations, which means it can fluctuate into an electron-positron pair for a short time, see the right-hand Feynman diagram of Figure 1.1. Clearly, the process of electron scattering is now more complicated than it first appeared, as there are many diagrams to describe the same process. The solution to this is to add the amplitudes of the diagrams together to form a prediction of the observed electron scattering cross-section. Unfortunately, infinities arise in the equations, which cause problems, and this leads to the intriguing conclusion that it is essential to redefine the electric charge on the electron. This procedure is known as renormalisation, and the phenomenon is referred to as charge shielding. Essentially, the electron is actually surrounded by e^+e^- pairs from the polarised vacuum, so that the charge is shielded. However, if a more energetic probe is used, it will cut through the shield and is then subjected to a larger electric charge. The electromagnetic coupling increases with the energy Q^2, this is known as the running coupling constant.

The success of QED, which has now been accurately tested experimentally to approximately 7 significant figures, paved the way for the development of Quantum Field Theories for the other fundamental forces.

1.5 Electroweak Interactions

The weak charged current interactions were first observed in radioactive nuclear decays, specifically in beta decay, which was studied intensively in the early 20$^{\text{th}}$ Century. Fermi was the first to formulate any type of theory of weak interactions, but it was modified by the V-A theory in the 1950's following the discovery of parity violation. This stated that the interaction between fermions and the weak charged current had the form of a vector, minus an axial vector, rather than the simple vector form that Fermi postulated, which was based upon the electromagnetic interaction. This means the weak interaction only couples to left-handed particles (right-handed anti-particles), and that neutrinos are only found in left-handed states. The leptons can now be grouped into doublets of the weak interaction for each generation,

$$\begin{pmatrix} e \\ \nu_e \end{pmatrix}_L \quad \text{and} \quad \begin{pmatrix} \mu \\ \nu_\mu \end{pmatrix}_L , \tag{1.1}$$

so that a flavour changing charged current interaction (now represented at first order by a single W exchange) can interchange leptons within a doublet, and both doublets have identical coupling strength. However, problems occur when this is extended to weak interactions involving quarks, because it is tempting to propose doublets constructed simply from the two quarks of a generation, but, there are observed cases of strange decays into u quarks. Cabibbo suggested a solution to this [8] by realising that the weak eigenstates were not the mass eigenstates, and that the doublets were actually,

$$\begin{pmatrix} u \\ d' \end{pmatrix}_L \quad \text{and} \quad \begin{pmatrix} c \\ s' \end{pmatrix}_L , \tag{1.2}$$

where,

$$\begin{aligned} d' &= d\cos\theta_c + s\sin\theta_c, \\ s' &= -d\sin\theta_c + s\cos\theta_c. \end{aligned} \tag{1.3}$$

The parameter θ_c, or Cabibbo's quark mixing angle implies that the coupling of the u to d quark is reduced by a factor $\cos\theta_c$, and the coupling of the u to s quark

is reduced by a factor $\sin\theta_c$ from the coupling of the leptons. Experimentally θ_c is measured to be approximately 12.5^o.

Weak interaction theory was taking shape, and eventually intermediate vector bosons were postulated, these predicted the existence of a neutral current (Z^0) in addition to the already observed charged currents ($W^{\pm}$). During the early 1970's, the neutral current was observed and was found not to possess the ability to change particle flavours.

However, there were still problems with this attempt to produce a gauge theory of weak interactions, due to its non-renormalisability. This means that when higher order diagrams are included in cross-section calculations, quadratic divergences arise with catastrophic consequences, which cannot be absorbed by redefining parameters like the process used in QED. Electroweak unification solves this problem though, because new diagrams are introduced, mainly self coupling of propagators, which cancel the divergences, and therefore makes the theory a non-abelian gauge theory.

The three mediators of the weak force were first observed in 1983 [9, 10, 11, 12]: the $W^{\pm}$ and the Z^0, which have experimentally measured masses of 80.41 ± 0.10GeV and 91.187 ± 0.007GeV, respectively [13]. It is the fact that the bosons have mass, which causes the weak force to be weak at low energy, and is not due to the couplings being weak. In fact, at energies in the order of the mass of the bosons, it is not that weak at all, and is comparable in strength to the electromagnetic force because the coupling strengths are actually the same. This is the essence of combining the two interactions together to form the electroweak gauge theory.

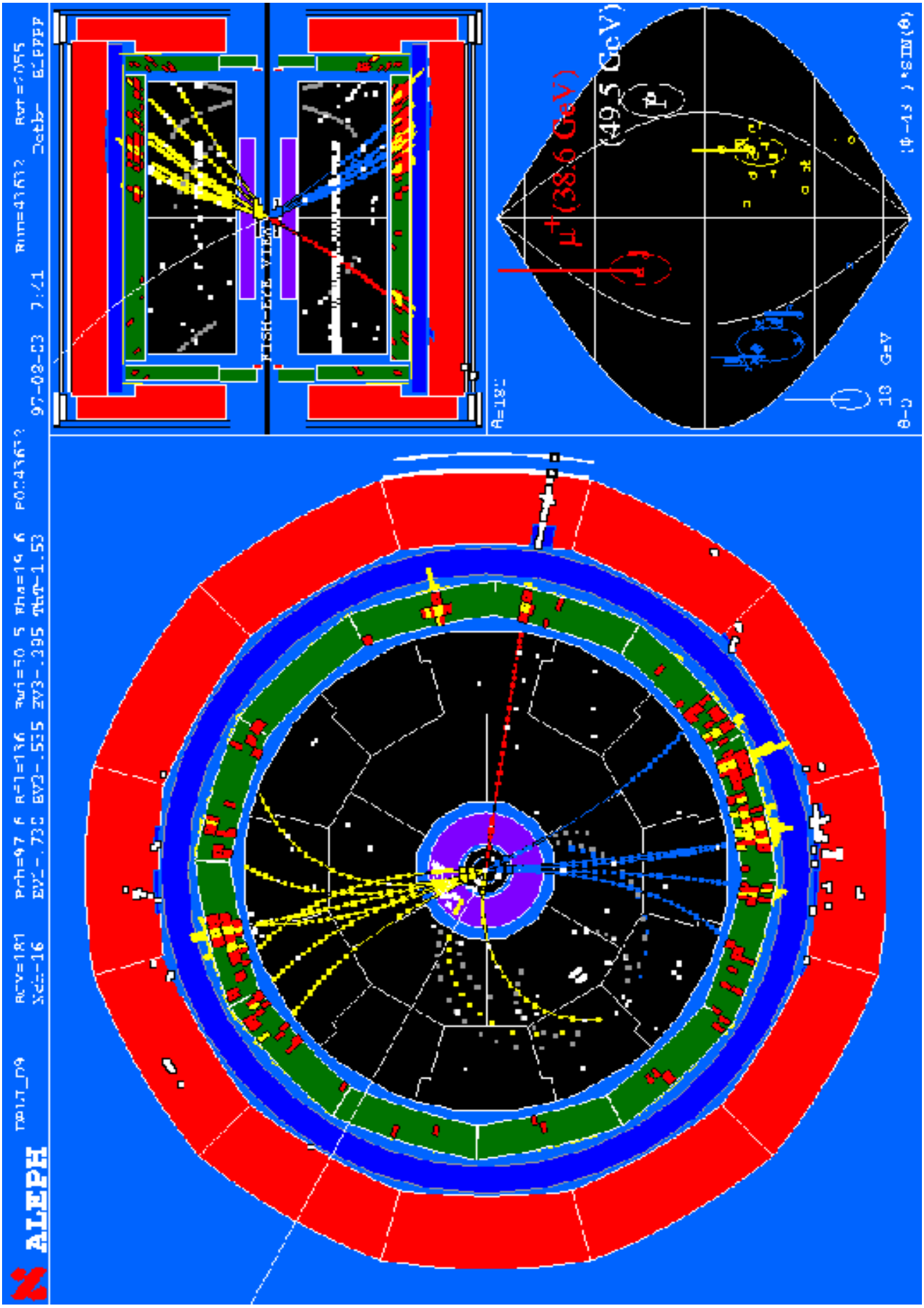

Figure 1.2: *A $W^+W^- \rightarrow q\bar{q}\mu\nu_\mu$ event recorded by ALEPH in 1997 at 183GeV.*

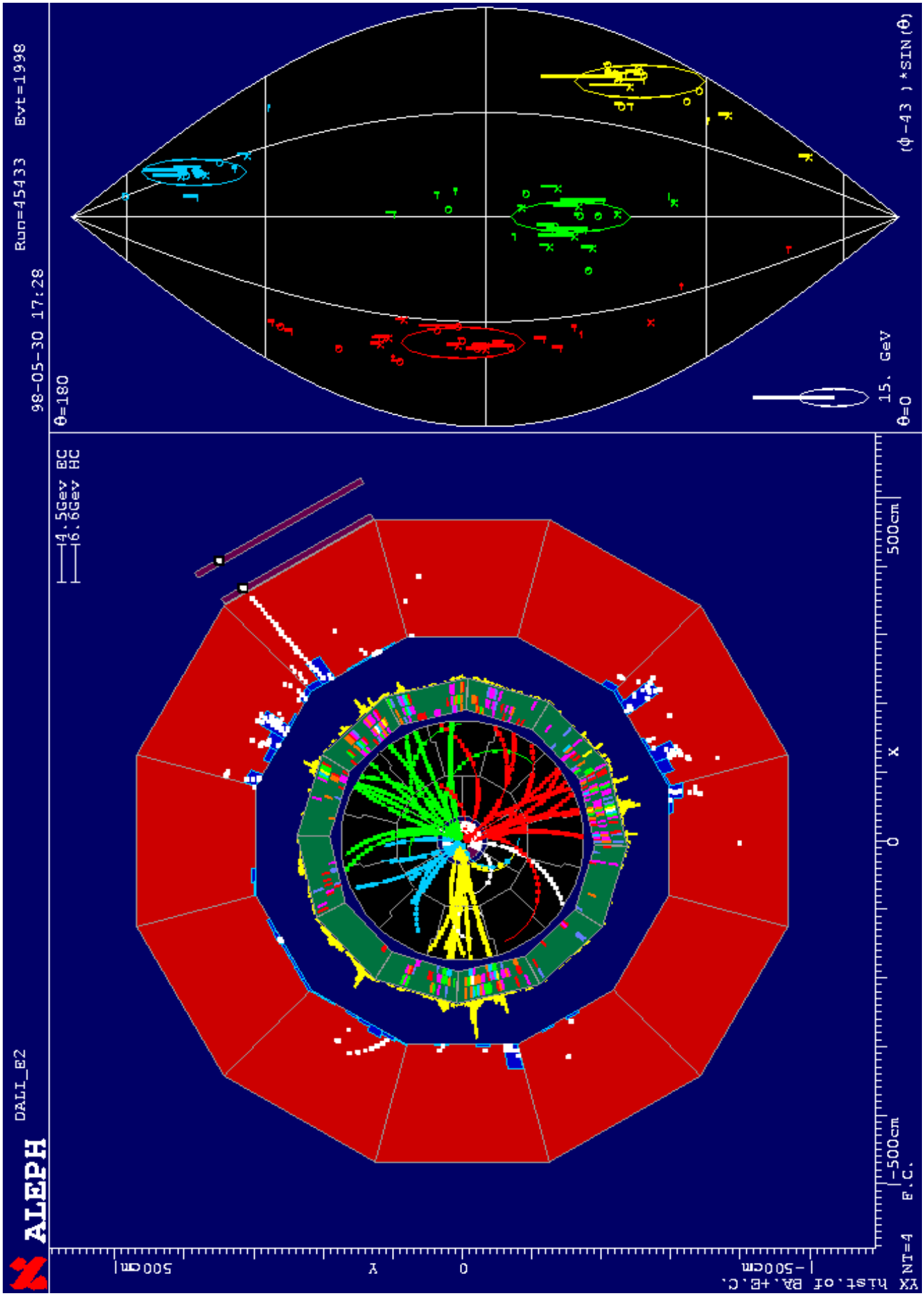

Figure 1.3: *A $W^+W^- \to q\bar{q}q\bar{q}$ event recorded by ALEPH in 1998 at 189GeV.*

1.6 WW Production at LEP2

From 1989 through to 1995, LEP ran at centre-of-mass energies around the Z^0 peak at 91.2GeV, and investigated many areas of the Standard Model with phenomenal precision. Throughout these six years, there were approximately 16 million recorded hadronic decays of the Z^0 boson between the four LEP experiments, predominantly as a result of the large production cross-section and low backgrounds.

In 1996, LEP entered the second stage of its investigations into the electroweak sector of the Standard Model: the production of W boson pairs at centre-of-mass energies above the production threshold of 161GeV. However, as a result of the small cross-section and there being many background processes only limited statistics could be collected. More information on the backgrounds can be found in Section 4.2 and the Feynman diagrams can be found in Reference [14]. The experiments rely on the increased luminosity delivered by the LEP machine in order to obtain an acceptable number of W pair events. From 1996, until the end of LEP2 in the Year 2000, the centre-of-mass energy and luminosity have steadily increased from a measly 20pb^{-1} at 161GeV and 172GeV, to an enormous 230pb^{-1} at around 200GeV in 1999.

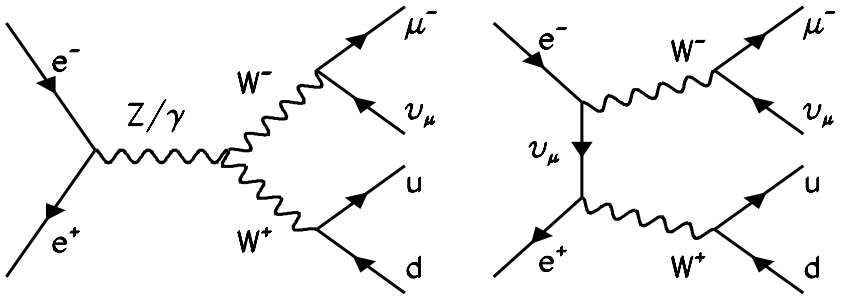

Figure 1.4: *The CC03 diagrams of W^+W^- pair production at LEP2.*

W pairs are produced at LEP2 by the three charged current diagrams (CC03 diagrams) shown in Figure 1.4. At threshold, the ν exchange dominates the cross-section and increases linearly with centre-of-mass energy, while the s channel

diagrams dominate at higher energies. The ALEPH event displays in Figures 1.2 and 1.3 show a semi-leptonic muon event recorded in 1997 at 183GeV and a fully hadronic event recorded in 1998 at 189GeV, respectively.

1.7 Quantum Chromodynamics and Colour

Following the discovery of the proton in the atomic nucleus in 1914, it was essential to postulate the existence of a new force, which had to be strong enough to overcome the electromagnetic repulsion between the protons, and thus hold the nucleus together. Early in the development of the theory of strong interactions, it was believed that hadrons experienced the force via pion exchange, but this was before the underlying component structure of the hadrons was understood. The concept of colour was first introduced to solve the Pauli Exclusion Principle's apparent violation [4, 2] in some baryons, where all three quarks appeared to be in the same state. It simply implied that the quarks now had a new quantum number, and therefore were no longer in identical states. As the quark model developed it was realised that the strong interaction between hadrons was actually the remainder of the colour force between the quarks within those hadrons[1].

Making a gauge theory to explain the strong colour force between quarks proves to be more straight-forward than for the electroweak case because QCD [1, 3] turns out to be renormalisable in quite a similar way to QED. The main features of QCD are that the quark possesses one of three colour charges, and that the gauge of the field, called the gluon, couples to the colour of the quark; the quark flavour here being irrelevant. There are eight gluons which are bi-coloured. The colour charge on the gluon is the essential feature causing QCD to be a non-abelian gauge theory, and allows gluons to couple to each other as well as the quarks. This self coupling creates a three and four gluon vertex as shown

[1] Analogous to the Van de Waal Forces that hold molecules together in some chemicals, being the remainder of the electromagnetic force holding the atoms together.

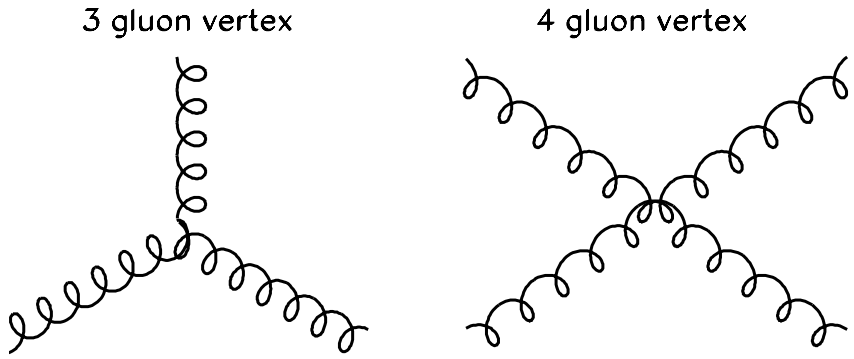

Figure 1.5: *The non-abelian nature of gluon self coupling.*

in Figure 1.5.

The non-abelian nature of QCD leads to several interesting physical features of the interaction, and while being related to QED, it is also subtly different. Beginning with vacuum polarisations, a gluon can fluctuate into a quark anti-quark pair, or into a gluon pair (because of the self coupling), when two quarks scatter. This results in a larger number of diagrams needing to be considered for calculations of the process, and when they are, the resulting colour force between the two quarks is found to increase with distance. This can be interpreted in two ways: firstly either the quarks are moving apart, for example, after an e^+e^- collision, in which case the gluons form a colour tube of increasing strength as they move apart; or, if one quark is viewed as a test charge scattering off the other, then the more energy it is given, the closer it gets but the weaker the attraction becomes. If the approaching quark is given sufficient energy, then at zero distance the two quarks will be free from each other's influence, this is called asymptotic freedom. This occurs because the coupling strength of the interaction, α_s, decreases with energy, and this is known as the running of the strong coupling constant.

Let us consider again, the case of the two quarks from an e^+e^- collision moving apart, and how they evolve into two jets. In the region where α_s is small, low order perturbation theory in powers of α_s can be used reliably to combine

the higher order loop diagrams. This allows relatively accurate simulations of the parton-shower[2] that arises as the quarks move apart. But, this introduces a problem because this implies that quarks can be at large separations with large forces between them. We know though that this is clearly untrue because in the macroscopic world, quarks and gluons are confined inside hadrons. In QCD, as the energy is reduced α_s increases until it is of such a value that perturbation theory stops working; no calculations are possible and this is dubbed the non-perturbative regime. Simple phenomenological models view the gluon strings as snapping, thus forming quark anti-quark pairs which manifest themselves as hadrons.

1.8 Colour Reconnection

In hadronic W pair events at LEP2, the W's space-time separation is roughly 0.5fm when they decay, which is within the QCD scale. This could be viewed as being two separate QCD point sources, which evolve into jets independently. In any standard simulation program this is naively assumed for the sake of simplicity. However, if we consider the problem further, it is realised that this view may be a little too simplistic, and thus we are led to the phenomenon of colour reconnection [14, 15, 16]. Essentially, this is the reconnecting of the colour-flow from the region of one W particle's evolution to the other W particle so that the decays are no longer independent. This could occur in either the perturbative phase, with gluon 'strings' reconnecting partons, or the non-perturbative phase allowing any pair of quarks to combine to form hadrons, rather than being confined to the quarks of a single W. It depends entirely upon the model chosen to simulate its effects. Various models of colour reconnection are discussed in the next chapter.

Colour reconnection is an interesting phenomenon in its own right and if it is investigated and evidence found of its existence, it will then be possible

[2]Parton-showers are discussed in Section 2.4.1.

to delve deeper into the mysteries of QCD. This would possibly enable us to test predictions of the perturbative parton-shower, or could simply further our knowledge of the non-perturbative hadronisation dynamics which are still not fully understood. However, one of the main reasons colour reconnection is of interest is because it could affect the W mass measurements, which is one of the main aims of the entire LEP2 project. In the hadronic WW channel, the mass measurement [17] relies heavily on the correct reconstruction of the multi-particle final state and the assignment of the particles to the correct W decay. If cross-talk between the two colour systems is occurring, it would almost certainly affect the final value of the W mass obtained. Consequently, it is essential to assign a systematic error to the W mass due to the unknown effect of colour reconnection. This thesis is concerned with searching for the effect for its own interest and has only tangential involvement in the hadronic W mass measurement.

The philosophy with which to scrutinise colour reconnection is still open to debate because the theoretical predictions vary from model to model, and therefore the most sensitive variables to look at are not known. However, all predictions are now united in their belief that the effects are small and that particle momenta and event multiplicities will be affected, though these variables may not be the best place to look. Chapter 4 deals with the experimental examination of charged event multiplicities and momentum distributions, while Chapter 5 investigates a set of variables with the aim of identifying regions sensitive to colour reconnection effects. Finding the best variable to observe an effect can only be achieved by using the reconnection models available to produce such a variable, and clearly this is dependent on the model itself. It must also be noted that there is no way of knowing if a Monte Carlo, either with or without the effect, is correct.

To allow the data to be checked against a sample which is independent of the effects of colour reconnection, the hadronic part of semi-leptonic events are used, and this is discussed in Chapter 4. In the case of average charged particle event multiplicities, there is no correct prediction of what the value for the hadronic

case should be, so twice the hadronic part of semi-leptonic events is used to test if the value is affected. The same argument holds for the momentum distribution and the ratio of the hadronic to twice the hadronic part of the semi-leptonics is checked.

Chapter 2

Monte Carlo Simulation Software

2.1 Introduction

This chapter is dedicated to the explanation of the various Monte Carlo programs used within this thesis to simulate the types of events recorded by the ALEPH detector. These include several samples of hadronic and semi-leptonic signal WW decays, a full simulation of the backgrounds to 4-fermion WW events, and the production of a range of colour reconnection models. First, the need for a Monte Carlo simulation is discussed and all the programs are listed, their main features are subsequently discussed, and any theoretical models of colour reconnection available are described. The size of all the generated samples used are shown in Table 2.1.

2.2 The need for Monte Carlo Simulation

Monte Carlo simulations incorporate theoretical information based on approximations of the Standard Model. They are used to produce artificial data in such a form that it is comparable to the observed physics, thus allowing the theory's compatibility to be tested. Yet, it must be realised that the Monte Carlo simulation is not initially produced in a form which can be compared to the raw data recorded by the detector.

Any Monte Carlo production is started by generating the pure underlying physics events from the Feynman diagrams and evolving the particles into pseudo-stable[1] final state hadrons and leptons. This 'underlying physics event' is believed to develop inside the detector for real data when an electron-positron annihilation occurs. Unfortunately, the detector is not perfect and the 'underlying physics event' will be distorted because some particles will be measured incorrectly or even missed entirely, therefore making the simulation and the data incompatible.

To solve this problem, a computer simulation of the detector is used to alter the Monte Carlo generated events in order to produce the required form, which is compatible with the data recorded by the detector. The ALEPH detector simulation is called GALEPH [18], and is based on the GEANT program [19], which is a general purpose detector modelling package. GEANT is a selection of routines allowing the user to 'build' a detector - inputting sizes and materials along with cracks and other inefficient regions. After GALEPH, the simulation is run through the ALEPH reconstruction package, JULIA[2] [20], as if it were real data; this produces the information stored in data banks to be analysed by ALPHA [21], the ALEPH physics analysis interface. ALPHA is a library of subroutines which allow the user to easily access, or calculate the information about event and

[1] A particle is considered stable if it has a lifetime greater than 3×10^{-10}s. This leaves pions, neutrons, kaons and muons, none of which are actually stable, but which are visible to the detector because they exist long enough to escape the beam-pipe region.

[2] JULIA is explained in Section 3.6.

particle properties such as momenta, angular, tracking and calorimetry, which are stored on the tapes produced by JULIA.

There are now two levels of simulation: the *generated physics level*, and the *reconstructed detector level*. The *generated physics level* is the underlying physics event with information about all multi-particle final state pseudo-stable particles, which are free from any influence of the detector, as explained earlier. The *reconstructed detector level* is the information about the particles in the form that they would be expected to be observed by the detector, and includes decays of the pseudo-stable particles such as kaons.

This means that the Monte Carlo simulation can be used for much more than just simple comparisons with data at the detector level. In this thesis, Monte Carlo simulated data is used to:

- correct the recorded data from the detector level to the generated physics level, by locating regions of detector inefficiency, and then removing them;
- estimate the proportion of background within a sample and correcting for its effects;
- remove any topological bias introduced by using the event selections;
- study sources of systematic uncertainty.

2.3 Monte Carlo Programs

2.3.1 PYTHIA 5.7

PYTHIA 5.7 [22] is a multi-purpose generator, and when used in conjunction with JETSET, is probably the most common High Energy Physics simulation in current use. In this case, it is used to generate all of the relevant backgrounds, such as $e^+e^- \rightarrow \mathrm{Z^0Z^0}$, and $e^+e^- \rightarrow \mathrm{Z^0e^+e^-}$, which produce 4-fermion final states[3]. In fact, some events in the ZZ sample possess the same 4-fermion final state as a generated WW event; such events are discarded from the ZZ background sample when the KORALW/JETSET WW sample is considered because they are already included in this WW sample[4]. However, this is not true for any of the other WW Monte Carlo samples investigated. High energy QCD events, $e^+e^- \rightarrow \mathrm{Z^0}/\gamma \rightarrow \mathrm{q\overline{q}}(\gamma)$, are also generated by PYTHIA. For some of the systematic studies, Monte Carlo at the $\mathrm{Z^0}$ peak generated in 1997 is used; this was manufactured using PYTHIA and JETSET.

2.3.2 JETSET 7.4

JETSET [22] was the original implementation of the Lund Model [23]. JETSET is now incorporated into PYTHIA, and evolves the quarks from any generated process into a multi-hadronic final state. The perturbative part of the Lund scenario utilises a phenomenological parton-shower model, while the hadronisation is achieved via string fragmentation. The JETSET Monte Carlo incorporates the three colour reconnection descriptions by Sjöstrand and Khoze [15, 16, 24, 25], and are used in conjunction with hadronic WW events generated with EXCALIBUR; this will be discussed in detail in Section 2.4.1. JETSET is used in con-

[3] A 4-fermion final state refers to the particles produced by the production Feynman diagram before any particle evolution is conducted.

[4] For example, $\mathrm{Z^0Z^0} \rightarrow u\bar{u}d\bar{d}$ has the same four fermions as $\mathrm{W^+W^-} \rightarrow u\bar{d}d\bar{u}$, and is included in the WW sample.

junction with PYTHIA for background simulation and with the WW generators, KORALW and EXCALIBUR.

2.3.3 KORALW 1.21

KORALW [26] is used to generate signal W pairs, and to produce their 4-fermion final states. It contains information about the W pair production and decay matrix elements, initial state radiation (ISR), comprehensive kinematics, and full 4-momentum conservation of decay products. Bremsstrahlung of W decay leptons is modelled, and hadronisation of quarks from W decays is achieved using JETSET. This combination of generating with KORALW, and evolving to hadrons using JETSET is relatively complete and regarded in the subsequent analysis as the standard Monte Carlo simulation. There is no colour reconnection in the KORALW/JETSET sample. KORALW is also used to generate the W pairs, but only from the CC03 diagrams, for the ARIADNE Monte Carlo samples.

2.3.4 EXCALIBUR

EXCALIBUR [27] is an alternative generator of all Standard Model 4-fermion final states, including WW's. Events are generated using spinorial helicity techniques [28], and are assigned a weight. All backgrounds have their weights set to zero so as to eliminate them, consequently only the CC03 signal diagrams remain[5]. Hadronisation is achieved using an interface to JETSET, which allows the three colour reconnection models of Sjöstrand and Khoze [15, 16, 24, 25] to be incorporated. Section 2.4.1 contains further details on these models.

[5]The CC03 WW production Feynman diagrams are shown in Figure 1.4 on page 23.

2.3.5 HERWIG 6.1

HERWIG 6.1 [29] is a multipurpose generator, which also includes perturbative and non-perturbative QCD simulations. In this instance, it is used to fully simulate the WW events, but only from the direct CC03 diagrams, rather than the full 4-fermion ones. However, this simplification still includes matrix elements and spin calculations. HERWIG takes great care during the parton-shower, to reproduce the angular distributions of the partons created at each branch, for example, the opening angle between partons at a branch is always smaller than it is at the previous branch so as to manufacture a cone-like structure for the shower. An alternative phenomenological method of evolving the partons to hadrons via the Cluster Model is incorporated into HERWIG rather than the usual JETSET scenario. Colour reconnection [15, 16] is achieved during this non-perturbative phase of the hadronic evolution, further details on this model can be found in Section 2.4.4.

2.3.6 ARIADNE 4.10

ARIADNE 4.10 [30] is not a WW generator, it is an alternative method for producing a parton-shower, via the Dipole Cascade Model [31, 32]. Colour reconnection [15, 33, 34] is achieved through connections made during the perturbative phase of the evolution. The ARIADNE Monte Carlo samples are generated by KORALW before the Dipole Model is instigated. ARIADNE then has to be interfaced with JETSET for non-perturbative hadronisation of the products from the dipole parton-shower. The Dipole Model and the colour reconnection models are discussed in more detail in Section 2.4.3.

2.4 Colour Reconnection Models

2.4.1 The Sjöstrand and Khoze Models

The colour reconnection models by Sjöstrand and Khoze [15, 16, 24, 25] are included as part of the JETSET Monte Carlo program [22] that simulates perturbative and non-perturbative QCD. In this study, the EXCALIBUR Monte Carlo generator [27] is used to simulate events before they are interfaced to the standard version of JETSET, which evolves the events into multi-particle final states. The same events are then evolved using a modified version of JETSET, which incorporates a colour reconnected model to produce a modified multi-particle final state.

Sjöstrand and Khoze state that while reconnection effects do occur in the perturbative stage, they are negligible. They arise because the colour singlets from the original W decays are rearranged from $q_1\bar{q}_2$ and $q_3\bar{q}_4$, to $q_1\bar{q}_4$ and $q_3\bar{q}_2$, but when hard perturbative gluons are emitted, there is a kinematic suppression related to the number of gluons, $\frac{1}{N_c^2-1} = \frac{1}{8}$ [24, 35]. Thus, this emission of hard gluons only results in interference to second order and is therefore strongly suppressed.

However, in the non-perturbative regime the effect of colour reconnection can be of much greater significance. Yet, due to the insufficient knowledge about hadronisation, rigorous calculations do not exist and only phenomenological studies are possible. The JETSET program is based on the Lund Model [23] of QCD evolution, which views the W's decaying as follows: the W^+ and W^- fly apart from their production vertex and decay at some separation smaller than 1 fermi. A perturbative parton-shower develops separately around each W from its primary $q\bar{q}$ pair. The parton-shower can be viewed as a gluon string stretched between the quark and anti-quark via a number of intermediate gluons. The strings expand, and at the pre-determined point in parton energy where the model enters

the non-perturbative region, they fragment into hadrons and disappear. This is the original unconnected scenario; though if any of the strings from the two different W parton-showers overlap there is the possibility that a reconnection can be made and the fragmentation will be modified appropriately.

In the original Lund Model without colour reconnection, the strings are chosen to be nothing more than an abstract concept because their nature is irrelevant in the model. However, now that we have introduced the concept of strings interacting when they cross, it is clearly essential to define what a string is [36]. At one extreme, the string is viewed as a flux tube with definite size and shape; the tube has no influence outside of its volume and the inside of the tube has no pronounced structure. At the other extreme, the string is viewed as an infinitely thin vortex line, the core of which contains all of the topological information, while the string's influence falls with distance from its core. The two views of a string will produce different effects when they cross, which lead Sjöstrand and Khoze (SK) to develop several colour reconnection scenarios.

SK I - The strings are viewed as flux tubes and the probability to reconnect is proportional to the space-time volume overlap of the two tubes and saturates at unity. By default, the cut on reconnection probability is set to 35%. A variant of this model is used by the ALEPH collaboration where the probability to reconnect is set to unity, hence ensuring there are always reconnections. Every hadronic event generated by EXCALIBUR can now be considered as a colour reconnected event. However, this is dubbed an 'unphysical' model due to the numerous forced reconnections [37].

SK II - The strings are viewed as vortex lines and reconnect when they cross; only the first crossing of a string is allowed to reconnect.

SK II′ - This is a variant on SK II but with the additional constraint that to reconnect, the new combination must be of lower energy than the original configuration.

2.4.2 Geiger and Ellis Model

The Geiger and Ellis Model [38, 39] provoked a particular flurry of experimental checks for colour reconnection because previous theoretical studies suggested that the effects would be too small to observe, whereas this model predicted large observable changes in variables, such as the W boson mass, the hadronic WW charged multiplicity and momentum distribution. Yet, it must be noted the model was not used in this study because following investigations by the four LEP collaborations [40-46], it was found the model implemented into the VNI Monte Carlo [47] could not correctly predict simple event properties such as multiplicities or thrust distributions. Also, the original predictions put forward by the authors [38, 39] were not reproducible by any of the collaborations. However, overlooking its failures, the model did introduce a rather provocative interpretation of colour reconnection in the hadronisation phase, which is noteworthy.

The model worked to reconnect purely in the non-perturbative region, and was based on the assumption that partons had no 'colour memory' to tell them which W they came from, and to which partons they should coalesce with in order to form hadrons. As the shower develops in time, each pair of partons is assigned a probability to convert to a hadron, which depends upon their separation. It is at this stage that no restrictions are applied to prevent exogamous unions of partons with different parent W's, over endogamous ones. If a pair of partons are chosen to reconnect, there are two variations of how this can be achieved: the 'colour-full' scenario and the 'colour-blind' scenario. In the 'colour-full' scenario the full colour-flow of each parton is recorded and any pair of coloured partons can combine with the emission of additional non-perturbative gluons. The 'colour-blind' version is not concerned with the colour of the partons when they combine, hence no further gluons are emitted.

None of the collaborations have continued to investigate the VNI Monte Carlo or its colour reconnection model as no updated versions of the code were created to

challenge the experimentalists' criticism, following the untimely and unfortunate death of its main author in the Swiss Air crash on 2nd September 1998.

2.4.3 ARIADNE

There are two colour reconnection models [15, 33, 34] included within the ARIADNE program [30]. Both work in a similar way to reconnect the products of the two separate W decays in the perturbative region. ARIADNE relies on the Colour Dipole Cascade Model to produce a perturbative parton-shower before hadronisation is completed using the JETSET program [22] as described in Section 2.3.2.

In the Dipole Cascade Model, the emission of a primary hard gluon is seen as being radiated from the colour dipole between the parent $q\bar{q}$ pair. The subsequent emission of a softer gluon is viewed as being radiated from two colour dipoles between the previous gluon and either the quark or the anti-quark. The probability of emission from the original $q\bar{q}$ again, is suppressed by a factor of $\frac{1}{N_c^2}$. Further gluons are thus emitted from three dipoles and so on, until a chain of dipoles between the quark and anti-quark is formed and transferred to JETSET for hadronisation.

The first colour reconnection model was created by Gustafson and Häkkinen [15, 33] and aimed to reconnect partons from different parent W's, so that the 'string length', or λ measure [48, 49], would be minimised in the new configuration. First, the high energy gluons are emitted independently from the original W $q\bar{q}$ pairs until the gluon energy falls to 2GeV. In this model, gluons below 2GeV are ignored as they are believed to have unknown interference effects while only accounting for 4% of the total energy. Once all the gluon chains have been formed they are cut and each end is reconnected to any possible state, irrespective of which W it originated from and also disregarding the parton colours so that the λ measure is minimised. This occurs only once per event.

The second model is by Lönnblad [15, 34] and is more extreme than the aforementioned. First, colour indices are assigned to partons as they are emitted, and gluons down to the 2GeV cut-off point are produced via the standard Colour Dipole Model. Reconnections are then turned on for the production of gluons below 2GeV. Multiple reconnections per event are possible, but only if it is allowed by the colour indices which were assigned to the partons earlier on. Each reconnection is assigned a probability to reconnect of $\frac{1}{N_c^2}$, if the new string will be shorter. It is also possible to create reconnections within a single W system, which could lead to spurious results when generating semi-leptonic events.

In future reference to the ARIADNE colour reconnection samples the abbreviations AR2 and AR3 will be used to refer to the Lönnblad and the Gustafson and Häkkinen models, respectively.

2.4.4 HERWIG

The HERWIG Monte Carlo [29] uses an entirely different model of hadronisation to the standard string picture in JETSET, called the Cluster Model. It includes an additional step between the perturbative and non-perturbative regions called pre-confinement, and it is here that the colour reconnection models take effect. Immediately after the parton-shower has finished, all remaining gluons are split into a quark anti-quark pairs and the colour lines are traced so that every quark is linked to its anti-quark partner no matter where it is in the shower. They are then combined to form a colour singlet cluster, after which the hadronisation process can commence. The clusters are allowed to decay into hadrons, as governed by the flavour of the $q\bar{q}$ pair, if the mass of the cluster is low. However, if the mass of the cluster is large enough, two hadrons can be produced and the flavour of the two extra quarks needed will be chosen at random.

The colour reconnection model [15, 16] adds another step before the usual cluster formation stage. The original version of the Cluster Model forms a colour

singlet cluster, ij, from a $q\bar{q}$ pair linked by a colour line. However, the algorithm searches for another cluster, kl, which can be used to form two new colour singlet clusters, il and jk. This new configuration is only permitted if the sum of the two new cluster configurations are smaller in size than the original cluster. The size of a cluster is defined as being the separation of the production vertices of the component quark and anti-quark. It must be noted that it is possible to form colour reconnections within a W system, which will affect results of the semi-leptonic channel when the model is switched on.

2.4.5 Semi-leptonic Events

Special notice is given here to semi-leptonic events used in conjunction with the reconnected WW samples. In both ARIADNE and HERWIG the colour reconnection model changes the description of semi-leptonic event production, while EXCALIBUR leaves them unchanged.

In the case of ARIADNE, the authors deem the reconnection model to be inappropriate in its description of semi-leptonic events, and recommend that in any analysis, the results from the normal semi-leptonic sample should be used [50]. In the case of HERWIG, the colour reconnection model description of semi-leptonic events is perfectly valid once the Monte Carlo has been retuned to reproduce the Z^0 properties with the reconnections active.

For EXCALIBUR/SK the colour reconnection is inactive in semi-leptonic events, hence, only one semi-leptonic sample is necessary. Even for the hadronic decays, only some hadronic events are affected by the models, which are then stored. Therefore, to create a full sample, care must be taken to mix the connected hadronics with the correct remaining unconnected hadronic events, as well as the semi-leptonics.

2.5 Summary

KORALW and EXCALIBUR are used to generate the W pairs and the 4-fermion products of their decays, JETSET is then used to simulate the QCD parton shower and hadronisation, which produces a multi-particle final state. The KORALW/JETSET sample is the standard simulation and has no colour reconnection, while the EXCALIBUR/JETSET combination allows four samples to be constructed, three with colour reconnection models, and one without.

ARIADNE is an alternative model of the perturbative QCD parton-shower and is used to replace this part of the JETSET program. Within ARIADNE, there are two colour reconnection models, so three samples are made including the standard one. Events are generated using KORALW, before being passed to ARIADNE and then JETSET for hadronisation. HERWIG is an entire stand-alone simulation used to both generate W pairs, and to produce the multi-particle final state. Two samples are generated, one with, and one without the HERWIG colour reconnection model. PYTHIA is used to generate all three background samples, and JETSET is used to evolve the primary fermions into the multi-particle final states.

The widest variety of Monte Carlo samples was produced to model the 189GeV data recorded during 1998, and consisted of all of the above. However, no HERWIG samples were produced at 183GeV, and at the time of writing only the KORALW/JETSET samples exist for the 1999 data. The size of each sample generated is listed in Table 2.1.

MC Sample		No. events generated	Cross-section (pb)	Luminosity (pb^{-1})
183GeV	KORALW	80000	16.15	4953.9
	PYTHIA $q\bar{q}$	80000	107.25	745.9
	PYTHIA ZZ	29999	2.545	11787.0
	PYTHIA Zee	60000	6.709	8943.2
	EXCALIBUR	99997	15.73	6357.1
	ARIADNE	49999	15.73	3178.6
189GeV	KORALW	100000	16.95	5891.4
	PYTHIA $q\bar{q}$	100000	98.69	1013.3
	PYTHIA ZZ	80000	2.768	28901.7
	PYTHIA Zee	99998	6.845	14608.9
	EXCALIBUR	99993	16.620	6016.4
	ARIADNE	49995	16.620	3008.1
	HERWIG	99992	16.620	6016.4
192GeV	KORALW	100000	17.265	5792.1
	PYTHIA $q\bar{q}$	100000	95.820	1043.6
	PYTHIA ZZ	49997	2.823	17710.6
	PYTHIA Zee	80000	6.897	11599.2
196GeV	KORALW	100000	17.588	5685.7
	PYTHIA $q\bar{q}$	100001	91.014	1098.7
	PYTHIA ZZ	49998	2.855	17512.4
	PYTHIA Zee	80000	6.997	11433.5
200GeV	KORALW	100000	17.823	5610.7
	PYTHIA $q\bar{q}$	99996	86.584	1154.9
	PYTHIA ZZ	49995	2.847	17560.6
	PYTHIA Zee	80000	7.072	11312.2
202GeV	KORALW	100000	17.902	5586.0
	PYTHIA $q\bar{q}$	100000	84.537	1182.9

Table 2.1: *Monte Carlo samples*

Chapter 3

The ALEPH Experiment at LEP

3.1 Introduction

ALEPH is one of the four particle detectors on the Large Electron-Positron Collider (LEP) situated at CERN, near Geneva. ALEPH along with the other detectors, DELPHI, OPAL and L3, was built to record events produced from the collisions of the high energy electrons and positrons accelerated by LEP, thus furthering our knowledge of the Standard Model. In particular, it allows experimentalists to search for the elusive Higgs Boson, and for an incredible array of Super Symmetric particles, work in the fields of QCD, $\gamma\gamma$ and electro-weak physics, but also to measure free parameters of the Standard Model more accurately than ever before.

This chapter will begin with a brief description of the LEP collider, and then the ALEPH detector will be considered; all of its sub-detectors will be described in turn and their main features and purposes will be explained.

3.2 The LEP Collider

It is situated approximately 6km from Geneva (at its nearest point), straddling the Swiss/French border at the foot of the Jura mountains on the northern shore of Lake Geneva. LEP is listed in the Guinness Book of Records as being the largest machine in the world; it is an incredible 8.5km in diameter and is housed in a circular tunnel 27km in circumference and is buried up to 140 metres at its deepest point below the surface.

CERN has a wide variety of accelerators and storage rings which are arranged along with the four experiments as shown in Figure 3.1. In their heyday, these accelerators hosted many experiments themselves, but now, they have been 'recycled' into stepping stones, for the insertion of electrons and positrons into LEP. This then accelerates them to final physics energies, where they are left to coast for several hours. The acceleration is achieved by using radio frequency (RF) cavities, which are also used once the particles are at the required energy of collision to combat energy lost due to synchrotron radiation.

The electrons and positrons are made to circulate around LEP in bunches by dipole magnets all around the ring. The bunches also have to be focused every so often on their journey, which is achieved by quadrapole magnets. Normally, there are four electron and four positron bunches in the machine, circulating anticlockwise and clockwise respectively, and these are brought into collision at the centre of the four detectors every 22μs.

LEP was brought on-line in 1989, and entered the first phase of its ten year life, to produce centre-of-mass energies on the Z^0 resonance. The beam energies were approximately 45.6GeV and LEP delivered about 4 million hadronically decaying Z^0 particles to each of the four experiments in the six years to follow. In 1996, LEP entered its second phase, so-called LEP2, which involved running at higher energies. Centre-of-mass energies of 161GeV and 172GeV were investigated in the first year, allowing W pair production for the first time in an e^+e^- machine.

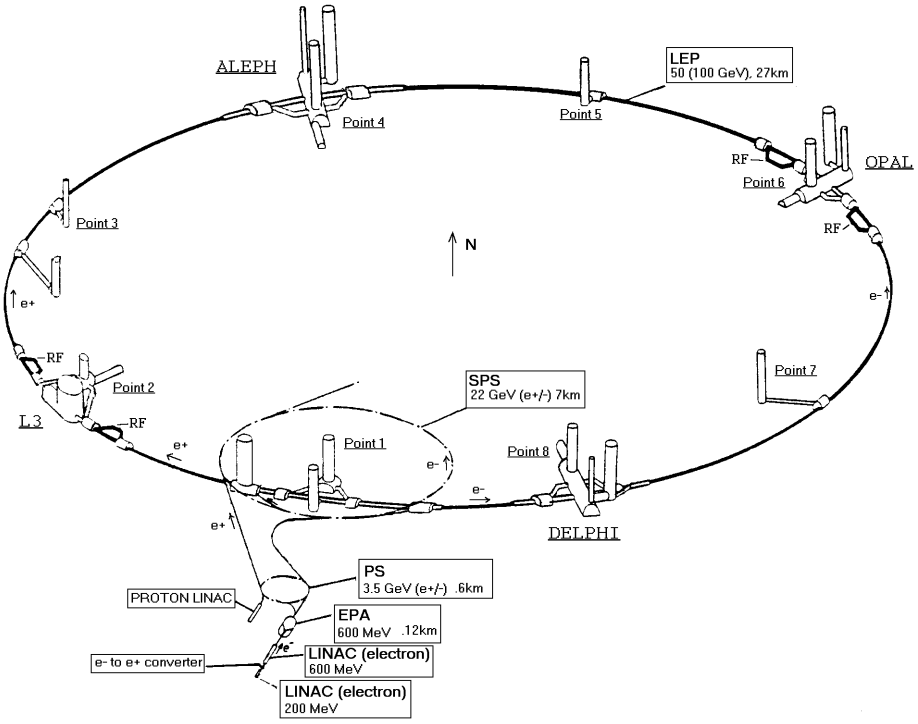

Figure 3.1: *The LEP Collider.*

In 1997 and 1998, $\sqrt{s} = 183$GeV and $\sqrt{s} = 189$GeV energies were achieved. Each year of LEP2 has seen huge increases in the luminosity delivered to each experiment, which is largely due to the replacement of the RF cavities in the LEP tunnel. In 1998, a massive 175pb^{-1} was delivered to each detector, compared to only 57pb^{-1} the year before. LEP2 will end with the decommissioning of the machine in the Year 2000 and it is estimated that over 600pb^{-1} will have been collected by each experiment over the entire LEP2 run. In 1999 each detector received approximately 240pb^{-1} and centre-of-mass energies in excess of 200GeV were achieved for the first time in an e^+e^- machine.

3.3 Introducing the ALEPH Detector

The ALEPH detector [51, 52, 53] is located at the deepest point on the LEP ring, in a $70 \times 16 \times 16\text{m}^3$ cavern, 143 metres under the foot of the Jura mountains, next to the small French village of Echeneveux. From inside the cavern, ALEPH can be seen as a 12 metre long cylinder, with a diameter of 12 metres. The LEP beam-pipe goes through the centre of the detector some 6 metres above the cavern floor; at this point, and for several hundred metres either side of the detector, the LEP beam-line is actually straight. ALEPH can be seen to be made of three parts: the barrel, and the two end-caps. During service periods, such as the winter shutdown, the end-caps can be rolled back against the cavern walls so as to allow access to some of the components held deep within the centre of ALEPH's barrel region.

Rather than categorising the detector in terms of barrel and end-caps, it is better to consider it in terms of its component sub-detectors, and their purposes, as shown in Figure 3.2. The sub-detectors can be collected at this stage, into tracking detectors (Section 3.4), and calorimetry (Section 3.5), each having very different purposes. The tracking detectors are found inside the barrel; it is their job to record the trajectories of charged particles by the ionisation that they cause. The calorimeters surround the tracking detectors and are located in both the end-caps and the barrel; it is their job to measure the energy of particles and to provide the only position measurement of neutral particles. In addition, there are also various other detectors to measure the luminosity and the backgrounds from the LEP machine, these are located at small angles to the beam-pipe.

ALEPH however, is not only a sophisticated particle detector, it is also a collaboration of over 400 physicists, from 32 institutes representing 11 nations from Europe, China and the USA. It is these physicists who designed and built ALEPH, and who are responsible for maintaining it so that data can be collected to be analysed by other members of the collaboration.

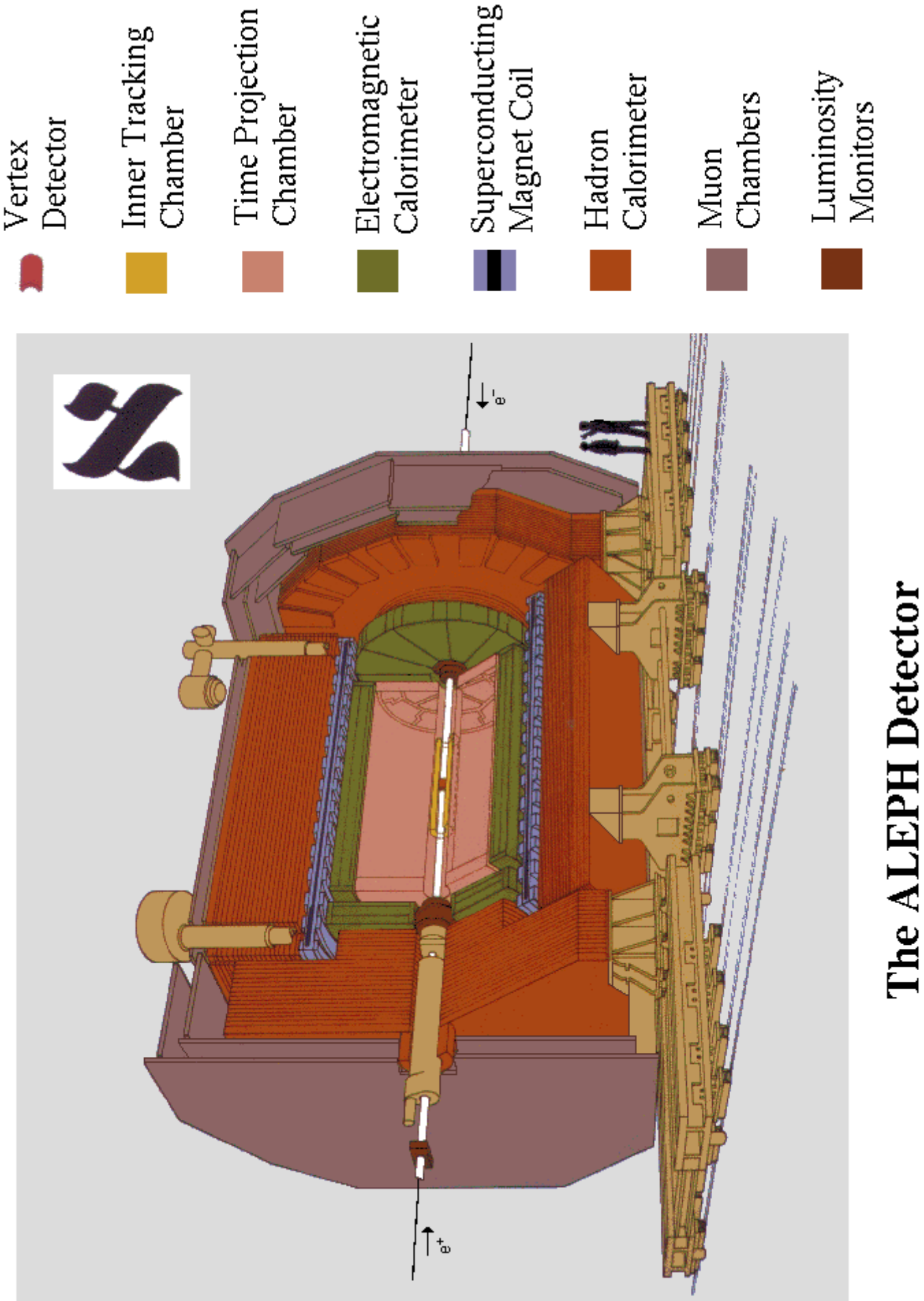

Figure 3.2: *The ALEPH Detector.*

3.3.1 The ALEPH Co-ordinate System

ALEPH uses three co-ordinate systems that will be referred to in later sections of this thesis, the origin of each is the theoretical interaction point. They are:

- **Cartesian -** The x axis points towards the centre of the LEP ring, the y axis is vertical and the z axis is along the e^- direction.
- **Cylindrical -** The radius co-ordinate, r, is measured from the point to the z axis, ϕ is the azimuthal angle, measured from the x axis towards the y axis and the z axis points along the e^- direction.
- **Polar -** The polar angle, θ, is measured from the z axis to the point. The azimuthal angle, ϕ, is measured from the x axis towards the y axis and the z axis points along the e^- direction.

3.4 Tracking Detectors

3.4.1 The Vertex Detector

In 1991, the first Vertex Detector[1] (VDET) [52] was installed to allow the trajectories of charged particles to be measured extremely close to the interaction point, and with extremely high precision. Thus, this allows better measurements of track impact parameters for the identification of short-lived particles with decay lengths of a few millimetres.

During the late summer of 1995, the VDET was replaced with the VDET2 [52], this had an improved design over its predecessor so as to increase the angular coverage and survive the higher demands of the LEP2 running. It is this detector that is described here and displayed in Figure 3.3.

[1]The location of the VDET is shown in Figure 3.2.

The active detecting volume of the VDET2 consists of two concentric cylinders, 40.0cm in length enclosing the beam-pipe, the first has a radius of 6.3cm, the second, 11.0cm. Each cylinder is made from double-sided silicon wafers, 5.26cm $\times$ 6.54cm, and six of these are joined to form a 40.0cm long face. There are nine faces on the inner cylinder, and fifteen on the outer one, the faces are arranged in such a way that they overlap in the $r\phi$ projection by approximately 2mm so as to increase coverage at the edge of the face.

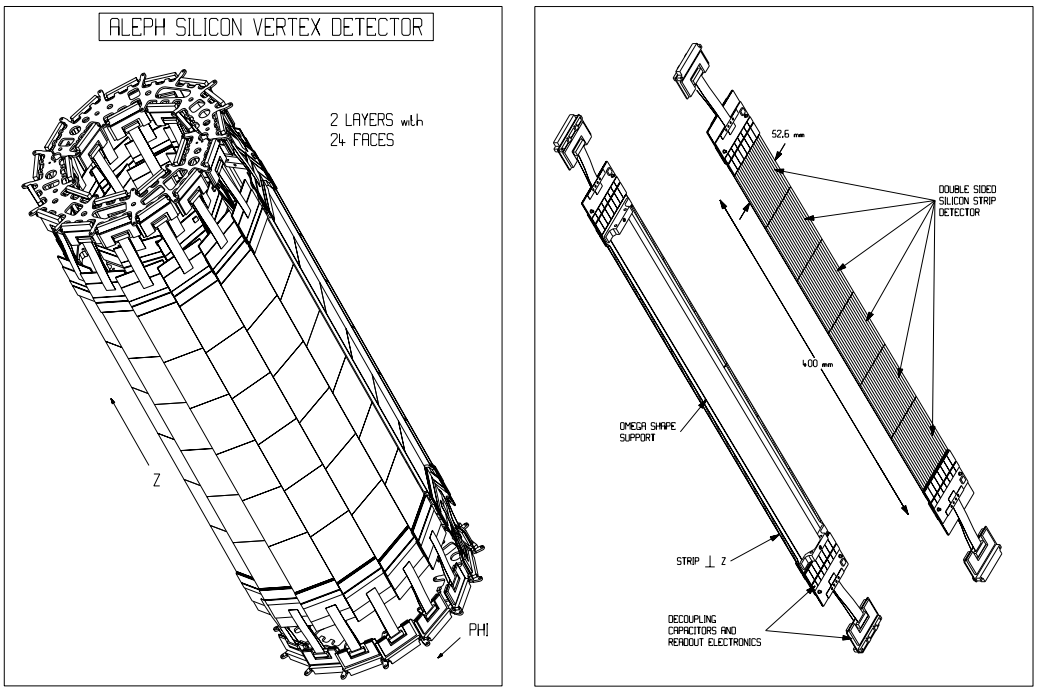

Figure 3.3: *The Vertex Detector II and one of its component strips.*

The original VDET was one of the first silicon detectors to utilise double-sided silicon technology, and the design of the wafers remains largely unchanged between the two detectors. On one side of the wafer, read-out strips are arranged parallel to the beam direction to measure the azimuthal angle ϕ. The z co-ordinate of the track is measured by the read-out strips on the other side of the wafer, arranged perpendicular to the azimuthal strips. The co-ordinate of the track in r comes from the mechanical structure of the detector. The VDET2 possesses the ability to measure particle positions with a resolution of $\sigma_{r\phi} \approx 12\mu$m and $\sigma_z \approx 14\mu$m. The angular coverage of the detector for tracks with only one

hit is $|\cos\theta < 0.95|$, where θ is the polar angle between the track and the beam direction. The angular coverage for the old VDET was only $|\cos\theta| < 0.85$ because it was only 20.0cm in length.

3.4.2 The Inner Tracking Chamber

The Inner Tracking Chamber (ITC) [51] is a cylindrical multi-wire drift chamber and surrounds the VDET in the centre of ALEPH, as shown in Figure 3.2. The active length of the chamber is 2 metres and has inner and outer radii of 128mm and 285mm, respectively. The ITC is the only tracking detector that provides information to the level one triggering system, this is possible because of its fast read-out. It also provides up to eight reasonably accurate tracking co-ordinates and has an angular coverage of $|\cos\theta| < 0.97$.

There are a total of 4800 wires in the ITC, all run parallel to the beam and are connected to aluminium end plates. The 960 sense wires are strung to form eight concentric layers of fixed radii; the inner four layers each have 96 sense wires, the outer four have 144. Each sense wire is surrounded by six of the 3840 field wires to form a hexagonal cell, with two field wires being shared by two neighbouring cells. The field wires are earthed at zero volts, and the sense wires are held at a positive potential of approximately 2kV during running to attract electrons ionised in the gas, which is 20% carbon dioxide and 80% argon. Additionally there are three cylindrical wire-mesh cages used to contain any snapped wires and also to stop them from falling into the rest of the detector.

The z co-ordinate of a charged track passing through a cell is obtained by measuring the time difference between the pulse at either end of the sense wire, giving a resolution of $\sigma_z \approx 7$cm as an average over the entire chamber. The $r\phi$ co-ordinate is obtained from the drift time of the ionised electrons produced in the gas to the sense wire and has a resolution of $\sigma_{r\phi} \approx 150\mu$m averaged over the drift cell.

3.4.3 The Time Projection Chamber

The Time Projection Chamber (TPC) [51] is the largest and main ALEPH tracking detector, and provides the most information towards momentum and $\frac{dE}{dx}$ measurements. It adds up to a further twenty-one three-dimensional tracking points to charged particles traversing its full acceptance, and like the other tracking detectors, the TPC is cylindrical in design. It has an internal radius of 31cm, which houses the ITC and VDET, as shown in Figure 3.2. The TPC has an overall length of 4.7 metres and an outer radius of 1.8 metres.

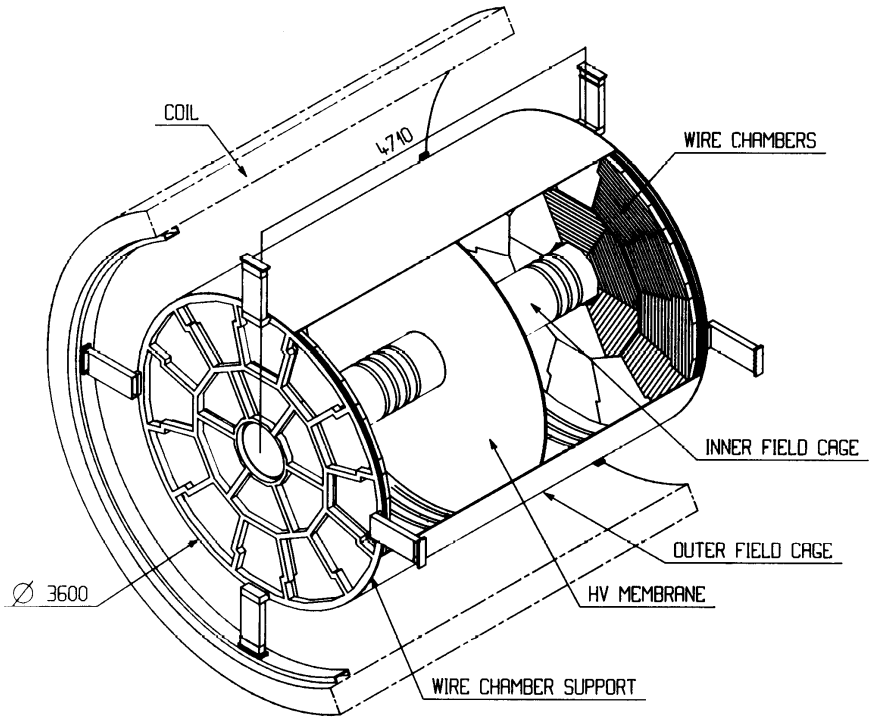

Figure 3.4: *The Time Projection Chamber*

The basic design of the TPC is quite simple: it is hollow. Filled with a gas mix of 91% argon and 9% methane, any charged tracks passing through this volume of the TPC will ionise the gas, and produce electrons which drift in the z direction towards the wire chamber sectors located at either end of the cylinder. The drifting of the ionised electrons is achieved by an ingenious arrangement of electrodes to manufacture a homogeneous E field inside the entire drift volume,

with only a component in the z direction. Firstly, a toroidal mylar membrane cuts the cylinder in half and has a voltage of -27kV on it; this results in electrons drifting towards the nearest end-cap. The inner and outer cylindrical walls of the TPC form a field cage, electrodes run circularly around them all down their length, and have voltages placed on them to keep the electric field parallel down the cylinder axis. The electric field is 115V/cm and the drift velocity is 5.2cm/μs.

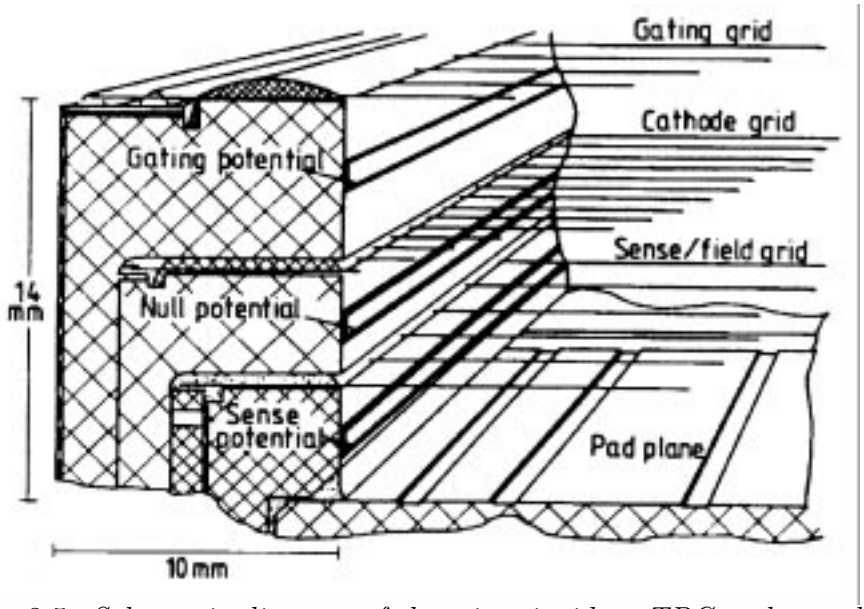

Figure 3.5: *Schematic diagram of the wires inside a TPC end-cap chamber.*

The final important component of the TPC is the wire chamber sectors, located on the end-caps of the cylinder, as shown in Figure 3.4. They complete the electric field requirements, and are also the detectors of the ionisation electrons. Both ends of the TPC are divided into 18 sectors, six inner and twelve outer ones. The joins between the sectors cause a dead region of 24mm; in order to limit particles being completely missed in regions of particular ϕ, a zig-zag was deemed necessary between the outer sectors. Each sector is essentially the same and consists of the cathode sensing pads and three planes of wires: gating, cathode shield, and the sense/field grid. A schematic diagram of the arrangement of the wires inside a TPC end-cap chamber is shown in Figure 3.5. The first plane of wires encountered by the drifting electrons is the gating grid. This is used to prevent ions produced inside the wire chamber sector (from the avalanche near

the sense wires) from entering the drift volume and thus corrupting the electric field homogeneity. The gate is closed by producing a dipole between alternate wires 2mm apart, which the positive ions cannot cross. The gate is only open for a few micro-seconds before and after a beam-crossing, it is then closed unless the level one trigger is positive, in which case the gate remains open for a further 45μs, this being the maximum drift time for electrons travelling the full 2.2 metres from the mylar membrane. The cathode wire plane is 6mm beyond the gating grid and consists of grounded wires 1mm apart; these help to shape the electric field. The final wire plane is 4mm behind the cathode grid and consists of alternate sense and field wires 2mm apart. When the electrons avalanche near the sense wires, they induce a charge on the pads located a further 4mm beyond. The pads are 6.2mm in $\delta r\phi$ and 30mm in δr, and are arranged in annular rings 6.4cm apart; there are twenty-one pad rows between the inner and outer field cages. The TPC has a total of 41004 pads.

The z co-ordinate is measured from the drift time of the ionised electrons, and has a resolution of 1.2mm for the wires, and 0.8mm for the pads. The r and ϕ co-ordinates can be found because the exact locations of the pads are well known, the resultant resolution is 180μm.

3.4.4 The Super-Conducting Coil

To complement the tracking detectors of ALEPH, a magnetic field is required to bend the charged particles to measure their momenta. A field of 1.5T is provided by a super-conducting 7 metre long solenoid [51], with an inner and outer radii of 2.48 metres and 2.92 metres, respectively. Its location is shown in Figure 3.2. The magnetic field homogeneity in the z direction, $\frac{\Delta B_z}{B_z}$ throughout the TPC volume, is better than 0.2%, with r and ϕ components of less than 0.4 and 0.04%, respectively. The iron structure of the hadron calorimeter acts as the return yoke for the magnetic field. The coil operates at 5000 amps, at a

temperature of approximately 4 kelvin, where the niobium-titanium alloy wires are superconducting.

Charged tracks traversing the tracking detectors follow helical paths because of the magnetic field[2]. The projection of this helix on the wire chamber sectors of the TPC is the arc of a circle. Measuring the sagitta of this arc provides information about the radius of the projected circle, and therefore, the momentum of the charged particle. Studies have shown [53] that for 45GeV muons from Z^0 decays which have traversed all twenty-one TPC pad rows, a momentum resolution of $\Delta p/p^2 = 1.2 \times 10^{-3}(GeV/c)^{-1}$ is obtained using only the information from the TPC. If the ITC is used as well, $\Delta p/p^2 = 0.8 \times 10^{-3}(GeV/c)^{-1}$, and if all three tracking detectors are used to measure the momentum, then a resolution of $\Delta p/p^2 = 0.6 \times 10^{-3}(GeV/c)^{-1}$ is achieved. For tracks with smaller momenta, the resolution tends to improve due to the fact that the track is more curved and consequently it is easier to measure the sagitta.

3.5 Calorimetry

3.5.1 The Electromagnetic Calorimeter

Surrounding the TPC inside the solenoid (as shown in Figure 3.2), is ALEPH's ECAL, or Electromagnetic Calorimeter [51]. The ECAL's purpose is to measure the energy of electrons and photons leaving the tracking volume. When electrons pass through matter, they undergo Bremsstrahlung and produce photons. When photons pass through matter they produce electron-positron pairs; thus a shower of particles develops. Therefore, the ECAL is made from thin layers of lead, to produce such a shower; then high voltage wires detect the showering particles and induce a charge capacitively onto cathode pads. The total induced charge is proportional to the energy of the initial incoming particle.

[2]For more information about track helices, see Section 4.5.7.

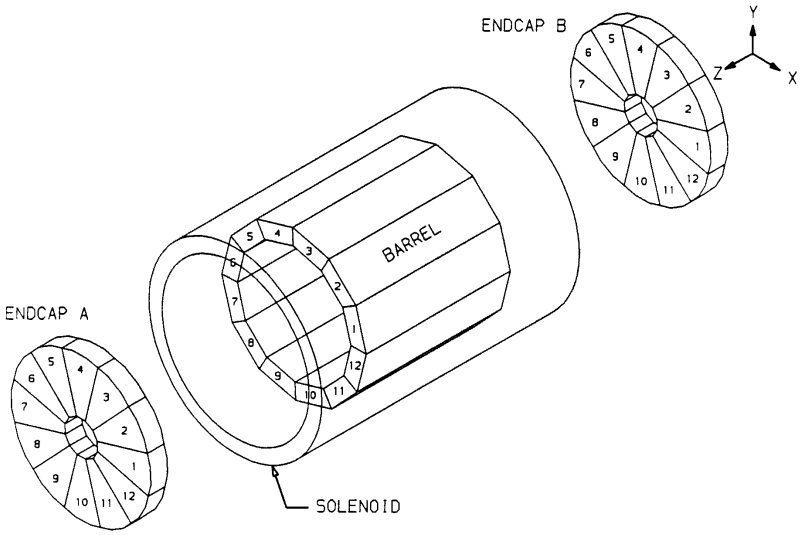

Figure 3.6: *The Electromagnetic Calorimeter*

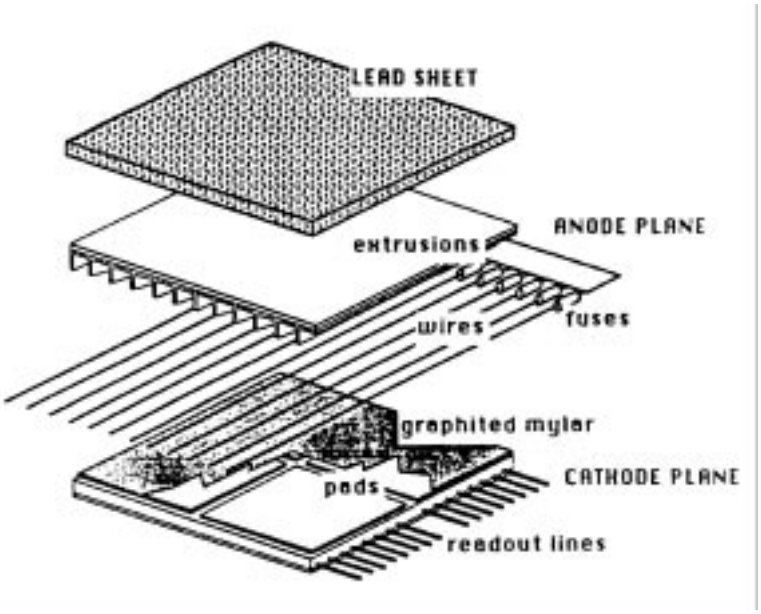

Figure 3.7: *An Electromagnetic Calorimeter stack layer*

The ECAL barrel is 4.77 metres long, with internal and external radii of 18.5 metres and 22.5 metres, respectively. The total solid angular coverage of 3.9π is completed by the two end-caps, giving a total weight of 194.4 tons. The barrel and each end-cap is made from twelve modules, as shown in Figure 3.6; the end-caps are rotated by 15^o with respect to the barrel so that the cracks between modules, where no read-out is possible, do not align. A module is filled with an 80% xenon and 20% CO^2 gas mix at 60mbar above atmospheric pressure, and is constantly circulated.

The simplest unit that is repeated throughout the ECAL is the stack layer shown in Figure 3.7. A stack consists of: a sheet of lead which develops the electromagnetic shower; a plane of 25μm diameter gold-plated tungsten anode wires, to amplify the signal in an avalanche; a layer of aluminium extrusions to form the wire chambers; and the cathode read-out pads, which have a resistive graphite mylar coating and have charge capacitively induced onto them. This stack unit is repeated 45 times to form a tower which points directly at the interaction region, there are 4096 towers in a barrel module, and 1024 towers in an end-cap module. Each tower is split into 3 storeys for read-out purposes; however, it is worth noting that the thickness of the lead changes in each storey. The first storey has ten layers of 2mm lead, the second has twenty-three 2mm layers and the third has twelve 4mm layers; each pad is approximately 30mm $\times$ 30mm.

3.5.2 The Hadronic Calorimeter and Muon Detectors

The final and largest sub-detector of ALEPH is the HCAL, or Hadronic Calorimeter [51], which encloses the remainder of the sub-detectors described above, as shown in Figures 3.2 and 3.8. Like the ECAL, it is constructed from a barrel and two end-caps, the barrel being made from 12 modules, and each end-cap from 6. Unlike the ECAL however, it uses 5cm thick iron slabs, rather than lead sheets

in order to produce a shower, therefore making the HCAL weigh in at a colossal 2580 tons. The barrel is 7.3 metres in length and has internal and external radii of, 300cm and 468cm, respectively. The end-caps have a diameter of 870cm and are 168cm thick inside the barrel, and 118cm thick at the barrel region.

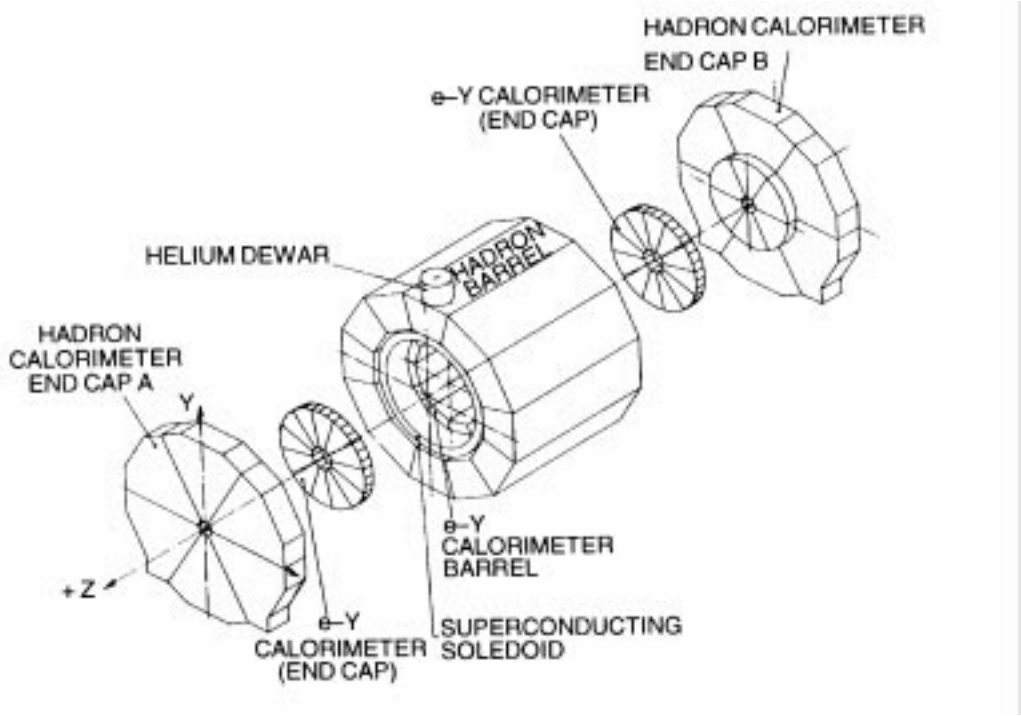

Figure 3.8: *The Electromagnetic and Hadronic Calorimeters*

In the barrel there are twenty-two iron layers; between each, and in front of the first, are placed detectors called streamer tubes. A streamer tube is made from a length of PVC plastic split into eight channels 0.9cm square. The internal surface is coated in graphite, and a high voltage 100μm diameter wire runs the length of the tube. The pulses on the wires are read out capacitively on copper pads, which are arranged so that the different layers form towers with an angular width of approximately 3.7^o. Each tower points at the interaction region. On the other side of the wires, 4mm wide aluminium strips run the full length of the tubes; a capacitative signal is used as a logical bit if the tube has been fired at least once. The gas used is a mixture of argon(22.5%), CO_2(47.5%), and isobutane(30.0%).

The iron layers are held in position by iron rods placed between them, which

unfortunately occupies space where the streamer tubes should be, consequently causing insensitive regions in azimuthal of 3.4%. Other insensitive regions are to be found at each end of a barrel module, where all the cables from inner detectors are found, the helium pipes in the top module and obviously at the edges of all the modules too. To remove any inefficient regions occurring in the same place in both ECAL and HCAL, they are rotated by 1.9^o with respect to each other.

The very outer part of HCAL is often categorised as a separate sub-detector, called the muon chambers, but they are actually two additional layers of the streamer tubes used throughout the rest of the HCAL. Any particle triggering a muon chamber will have crossed all the iron HCAL layers and can therefore be identified as a muon. The two layers of streamer tubes are positioned 50.0cm apart in the barrel region, and 40.0cm in the end-caps, which allows the angle of the muon trajectory to be measured. The arrangement of the capacitative read-outs is different to the rest of the HCAL; the pads are replaced with strips positioned perpendicularly to the wires. This improves the spatial resolution as required because the muon chambers are seen as tracking detectors rather than as calorimeters.

3.5.3 Luminosity Monitors

It is essential to measure the luminosity [53] delivered to the ALEPH experiment, as it is used in experimental measurements of cross-sections, and for normalisations in other physics analyses. The method used is to count the number of low angle Bhabha events because this pure QED process is very well understood theoretically.

The goal during LEP1 was to measure the luminosity to 0.1%, this was achieved using SICAL, or the Silicon Tungsten Calorimeter [52], which has an angular coverage between 1.4^o and 3.3^o due to its location 2.5 metres (at either end of the TPC) from the interaction point. This is the most accurate of the

luminosity monitors, unfortunately though, SICAL is not used during LEP2 running because it is obscured by the shields which were placed to protect the inner detectors from the higher cynclotron radiation.

LCAL, or the Luminosity Calorimeter [52] is used for luminosity measurements at LEP2, but only a precision of 0.4% is possible because LCAL has a worse angular resolution than SICAL. LCAL has essentially the same design as the ECAL, with wire planes and lead sheets used to form layers. LCAL is located behind SICAL at a distance of 2.67 metres from the interaction point and has an angular coverage from 2.6^o to 9.2^o.

The third luminosity calorimeter is called BCAL or the Bhabha calorimeter [52], and is located outside the main volume of ALEPH, beyond the quadrapole magnets, some 7.7 metres from the interaction region. It has an angular coverage from 0.3^o to 0.5^o, which allows 20 times the number of Bhabha events to be recorded than in LCAL, due to the increased cross-section at low angles. Unfortunately, because the electrons have travelled through the quadrapole magnet, their actual polar angle is unknown, therefore BCAL can only be used for on-line luminosity monitoring during data taking.

3.6 From raw data to fully reconstructed events

Clearly, the signals produced by the sub-detectors are not quite in a form which is ready to be analysed off-line. For this reason, there is a complex chain of data processing which has to be conducted in order to prepare the data for analysis.

3.6.1 Triggering System

It is essential to have a trigger system [52, 53] in a LEP experiment because it is not just e^+e^- annihilations which can occur when the bunches cross. Backgrounds include the following: interactions between the beam and gas in the beam-pipe,

because the vacuum is not perfect (beam gas events); off-momentum particles hitting collimators or the beam-pipe; and cosmic rays. There is no need to record such events, not just because they are of very little interest, but also because they leave the detector in a state which is unable to record a true event from the next beam-crossing. It takes 45μs for drifting ionisation electrons to reach the end-caps of the TPC, which is the slowest detector; it is therefore essential to decide whether it is worth waiting to read this out as there is a beam crossing every 22μs.

ALEPH uses a three-level triggering system. The first two are controlled by hardware devices for fast decision-making on the raw signals from the ECAL, HCAL, ITC, and TPC, while the Level Three Trigger is a software analysis of the event before it is written to tape.

The Level One Trigger delivers a decision within 5μs, based on any one of the following criteria being true:

1. energy deposited in the ECAL of greater than 6GeV in the barrel, 3GeV in one end-cap, or 1.5GeV in both end-caps;
2. a track segment in the ITC in coincidence with an energy deposit in the ECAL of greater than 200MeV;
3. a track segment in the ITC in coincidence with hits in the HCAL;
4. two back-to-back track segments in the ITC.

The Level Two Trigger works to verify the fast Level One Trigger using the increased resolution of the TPC rather than the ITC. It takes 50μs after a beam-crossing to make a decision. If a positive decision is obtained then the detector is read-out in its entirety, and the full event is analysed by the Level Three Trigger. The Level Three Trigger is software based, and makes a decision once the event has been combined from the sub-detector information by the DAQ. The Level

One Trigger fires at approximately 2Hz and the final rate of events written to tape is just less than 1Hz after the Level Three Trigger.

3.6.2 Data Acquisition

During the mid 1980's when ALEPH was being designed, computers were not as sophisticated as they are now. Consequently, it was not possible to read out all of the sub-detector components, to then combine, analyse and reconstruct information into events, without using many smaller computers. Hence, the DAQ, or Data Acquisition [52], was designed to be modular so as to work with all the individual components of ALEPH, which are read out in parallel before travelling up the DAQ chain to be combined to form full events. After a level two 'yes' has occurred, data proceeds along the following DAQ architecture:

- Read-Out Controllers (ROCs) are the first level of the DAQ. There are many ROCs; they are responsible for small parts of sub-detectors. They initialise the sub-detector electronics to be read out and formatted, and use simple calibration constants if needed.

- Event Builders (EBs) combine the signals from several ROCs to form a sub-event at the sub-detector level.

- Main Event Builder (MEB) collects all the sub-events from the EBs and reorganises the information to form one complete event. This event information is then sent via an optic fibre to the surface computers.

- The Event Processor is actually the Level Three Trigger, and rejects unwanted events after they have been combined by the MEB.

- The Main Read-Out Computer essentially copies the accepted complete events onto tapes and discs for subsequent analysis and storage. It also runs the on-line event display.

- FALCON. Once an entire run is completed (either 2 hours of data or 600Mbytes), all of the events within it are analysed by the FALCON computers, which run the ALEPH reconstruction program JULIA [20].

3.6.3 Event Reconstruction

The ALEPH reconstruction program, JULIA [20], takes the digital signals from the sub-detectors and converts them into two types of objects, both to be used in experimental analyses, tracks and calorimeter clusters. Further details on the event reconstruction can be found in Reference [53].

Calorimeter clusters are found by joining together adjacent storeys if they have an energy deposit of more than 30MeV. The same method is used for both the hadron, and the electromagnetic calorimeters.

Tracks have to be formed by using the hit information from the three tracking detectors. Many initial track segments are formed by joining nearby hits in the TPC, then, starting at the outer region of the TPC, track segments are added together following a helical hypothesis whilst moving towards the interaction region. This procedure is then extrapolated inwards, and compatible hits in the ITC and VDET may also be included. Now that some rudimentary tracks have been produced, a fit is done accounting for errors on the hits, and multiple scattering.

Once these fitted tracks have been obtained, momenta and position-related variables, and the $\frac{dE}{dx}$ are calculated and stored in BOS data banks on POT data tapes, ready to be analysed by the ALEPH physics analysis interface, ALPHA [21]. ALPHA is a library of subroutines allowing the user to easily access, or calculate, information about event or particle properties.

3.6.4 Energy Flow

The energy flow algorithm [53] aims to improve the overall energy resolution of the detector by creating energy flow objects, which are a combination of information from the individual sub-detectors. This association is achieved by taking advantage of the separate photon, electron, muon and hadron identification capabilities as well as the track momenta information available.

The first stage of the energy flow algorithm is called 'cleaning', because it attempts to identify only genuine charged tracks and calorimeter clusters from the under-lying physics event, rather than from misbehaviours of the front-end electronics, data acquisition system or the reconstruction chain. Charged tracks are used if they have four or more hits in the TPC and originate from a cylinder 20cm in length, and radius 2cm, centred around the interaction vertex. Tracks with reconstructed momentum above 15GeV must have at least eight TPC coordinates and an additional hit in the drift chamber. Identified V^0 particles are only considered if they originate from a cylinder of 30cm in length and radius 5cm around the interaction vertex. Occasionally there is noise in a calorimeter channel for several consecutive events, but this can be easily identified and removed with hindsight. Also, occasional fake energy deposits are removed if the signal in the towers is inconsistent with the independent measurement from other wire planes.

The second stage of the energy flow algorithm is to extrapolate charged tracks into the calorimeters and combine them with topologically compatible clusters. This is first done for identified particles, e, μ, γ, π^0, and they are then discarded leaving only calorimeter clusters originating from charged or neutral hadrons. Once the charged hadrons, which are assumed to be pions, have been combined with energy deposits they too are discarded, leaving only the neutral hadron energy deposits which are then assigned accordingly. Finally, neutrino trajectories can be implied from any missing energy in the detector.

The introduction of the energy flow algorithm is seen to improve the energy

resolution for data taken at the Z peak from approximately 12% to under 7% and leaves a list of particles per event, which are realistic representations of the true particles produced. These reconstructed objects are the starting point of most physics analyses.

Chapter 4

Colour Reconnection studies of Multiplicity and Momentum

4.1 Introduction

In 1997, data was recorded with the ALEPH detector at a centre-of-mass energy of 183GeV; the following year the centre-of-mass energy was increased to 189GeV. From this data volume, it transpires that marginally less than one thousand W pair decays were recorded during 1997, and approximately three thousand during 1998, of which approximately half were fully hadronic decays.

This chapter is devoted to explaining the analysis chain used to examine these WW events in the first of the two colour reconnection studies. This colour reconnection investigation is relatively straight-forward; it considers the event multiplicities and lab-frame momentum distributions to be the important properties and investigates the effect of colour reconnection on them. The distributions are corrected and compared to Monte Carlo models, both with and without colour reconnection.

4.2 Event Selections

In order to conduct this investigation, it is essential to examine fully hadronic WW events, *i.e.* when both W's decay into jets, because it is these events where colour reconnection is predicted to occur. However, it is also necessary to scrutinise semi-leptonic WW events, where only one W decays hadronically, and the other decays leptonically. Colour reconnection cannot occur in semi-leptonic events, consequently, they can be used as a reference data sample which is free from its effects. This allows data to be compared with data, as opposed to being dependent on theoretical predictions. More information about the effects of colour reconnection and the philosophy of searching for it can be found in Section 1.8 and in Chapter 2.

This study utilises the event selection tools originally developed by the ALEPH W mass measurement group [54]. The hadronic selection procedure was changed slightly from its original design to acknowledge the different aim in this analysis. The semi-leptonic event selections remain as standard [54, 55, 56]. From 1997 to 1998, the event selections remained unchanged except that the neural network hadronic selection was retrained on 189GeV Monte Carlo.

4.2.1 Hadronic Event Selection

Fully hadronic WW events are generally high multiplicity 4-jet events, which are produced when both W bosons decay to two quarks; each quark then evolving into a jet. These four jets are distributed reasonably spherically in the detector. The main source of background to the $e^+e^- \rightarrow \mathrm{W}^+\mathrm{W}^- \rightarrow q\overline{q}q\overline{q}$ is the $e^+e^- \rightarrow \mathrm{Z}^0/\gamma \rightarrow q\overline{q}(\gamma)$ high energy QCD annihilations, which generally have a 2-jet like structure. Some QCD events are also subject to initial state radiation (ISR), also known as radiative returns to the Z^0 via photon emission. These can be easily detected and eliminated; either they have a large missing momentum when the ISR photon is not detected, or if it is detected, a high energy γ: the rest of

the event has a total mass near the Z^0 mass and a large boost. Other processes which form a much smaller fraction of the total background are $e^+e^- \rightarrow Z^0Z^0$, $e^+e^- \rightarrow Z^0ee$, and $e^+e^- \rightarrow W^+W^- \rightarrow q\overline{q}l\nu$.

Pre-selection

Hadronic candidates must first pass a set of pre-selection criteria, with the aim of removing all background which is significantly different from the required signal, whilst retaining a high efficiency for the hadronic events. The first step is to ensure candidates are, what is known as *class 16* events, which are defined as having five or more good charged tracks[1] in the TPC, and that the total energy of these tracks is over 10% of the centre-of-mass energy. Essentially, this is selecting events with hadronic tracks, and rejecting low multiplicity backgrounds such as two photon, leptonic, cosmic ray, and beam gas events. After forcing to 4-jets, using the DURHAM algorithm[2], the rest of the pre-selection to further remove more complex QCD backgrounds proceeds as follows:

- The total longitudinal momentum relative to the beam-line must be less than 95% of the difference between the total visible mass and the mass of the Z^0. This cut is to remove radiative returns to the Z^0 and essentially works because these events, if no ISR γ is seen, will have a strong boost down the beam-line.

- The sphericity[3] must be greater than 0.03. This cut identifies and removes clear non-spherical, and hence QCD events.

- $y_{34} < 0.001$, [4] this cut is to remove QCD events which are easy to convert to 3-jets because they are more planar than hadronic WW events.

[1] A good charged track is defined in Section 4.4.1.

[2] General information on jet-finding is presented in Appendix A.2.

[3] Sphericity is defined in Appendix A.1.

[4] y_{34} is the criterion where a 4-jet event becomes a 3-jet event, see Appendix A.1.

- The electromagnetic energy in a jet must be less than 95% of the total jet energy to identify an electromagnetic jet from an ISR γ.

Neural Network Selection

A neural network is now used on the pre-selected events to extract even more of the background, and thus further increase the purity of the signal. Nineteen variables including event shapes, properties of jets, WW kinematics, and heavy flavour tagging are fed into the neural network.

The nineteen input variables are as follows:

- **Global event properties:**

  1 - Missing energy in the event (*EM*);
  2 - Sum of the squared transverse momenta of tracks in the second jet (*SUMPT2*);
  3 - Sphericity[5] (*SPH*);
  4 - Fox-Wolfram moment H0[5] (*H0*);
  5 - Fox-Wolfram moment H2[5] (*H2*);
  6 - Fox-Wolfram moment H4[5] (*H4*);

- **Heavy flavour tagging:**

  7 - Sum of the b-tag probabilities of the four jets (*SUMPROB*);

- **Properties of jets, which are energy ordered, highest first:**

  8 - Number of tracks in first jet (*NTK1*);
  9 - Highest energy of any object in first jet (*OBJ1*);
  10- Highest energy of any object in second jet (*OBJ2*);
  11- Highest energy of any object in third jet (*OBJ3*);
  12- Sum of angles between highest energy track and all other tracks in first jet (*COS1J*);
  13- Sum of angles between highest energy track and all other tracks in second jet (*COS2J*);

[5]See Appendix A.1 for explanation.

- **W^+W^- Kinematics:**

  14- Total energy of the most energetic jet (*EJ1*);

  15- Energy of the second jet (*EJ2*);

  16- Momentum of jet 4 (*EJ4*);

  17- Sum of the cosines of the six angles between the jets (*ANGTOT*);

  18- Cosine of the angle between the second and third jets (*ANG4*);

  19- Asymmetry[6], A_{12}, between the second and third jets (*ASY2*).

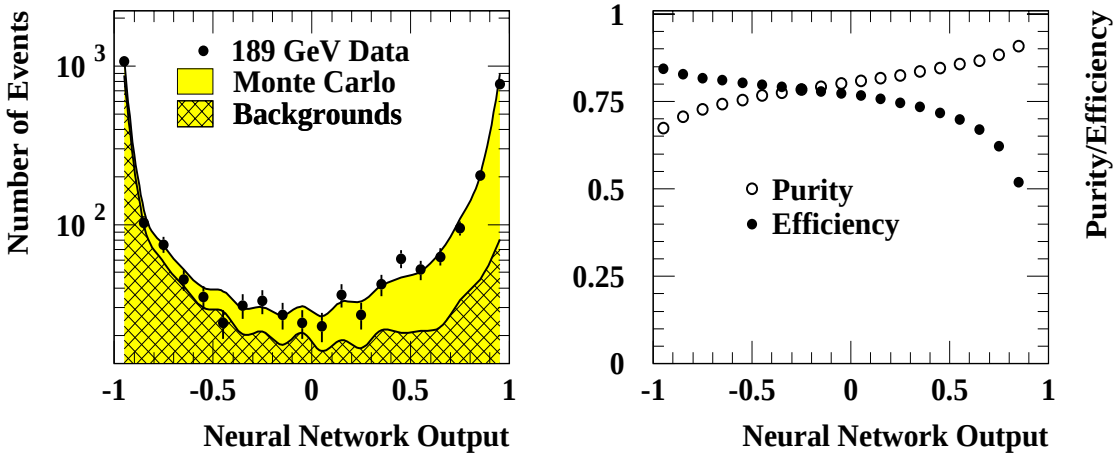

Figure 4.1: *Data/Monte Carlo agreement of hadronic neural network output and selection efficiencies/purities.*

Distributions of the nineteen variables at 183GeV and 189GeV can be found in Reference [55] and Appendix B, respectively; the data/Monte Carlo agreement can be seen to be acceptable. The neural network outputs a value (*outnn*) for every pre-selected event between -1 and 1, which is used as the final discriminant between signal and background; Figure 4.1 shows the distribution of the neural network output, and the purity and efficiency of the selection as a function of *outnn*. For the W mass analysis [54, 57], and WW cross-section measurements [55, 58], a cut is applied so that events with an output greater than -0.3 were selected (the background is clustered at negative values, as shown in Figure 4.1). In this analysis however, this output cut is moved to a more efficient region, at

[6]The asymmetry between two jets of momentum $\vec{p_1}$ and $\vec{p_2}$ is defined as, $A_{12} = \frac{|\vec{p_1}-\vec{p_2}|}{|\vec{p_1}+\vec{p_2}|}$.

the sacrifice of a lower hadronic purity, of -0.9, Figure 4.2 shows the increased efficiency of events with small inter-jet opening angles. This change to the neural network is justified in Section 4.2.2.

4.2.2 Changes to the Neural Network

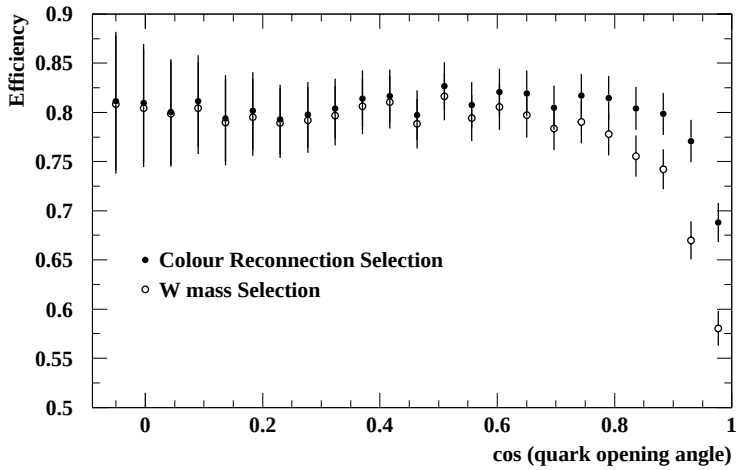

Figure 4.2: *Selection efficiency as a function of the cosine of the opening angle between primary quarks from different W decays in simulated hadronic events, for the original and improved selections.*

Early theoretical studies of colour reconnection [33, 38, 39] suggested the effect would be enhanced when two jets originating from different W's evolved almost on top of each other. Or more practically, if the angle between two jets from different W's was very small, then it seems plausible that colour reconnection would be more apparent. These studies were originally conducted at the W pair production threshold (162GeV), where there was no boost of the W particles involved, which produced two back-to-back jets. Yet, in 183GeV and 189GeV events, the W's are boosted, therefore, the two jets from a W decay tend not to be back-to-back in the lab frame. Given this new information about the higher energy WW events, the argument for the increase of colour reconnection still holds, except that the events now take on a more planar (3-jet like) shape when two jets are close together, rather than the linear (2-jet like) shape at 162GeV. In

fact, the two jets from the same W decay at 183GeV cannot be produced closer than approximately 120°, as shown by the angular distribution on the right of Figure 4.3.

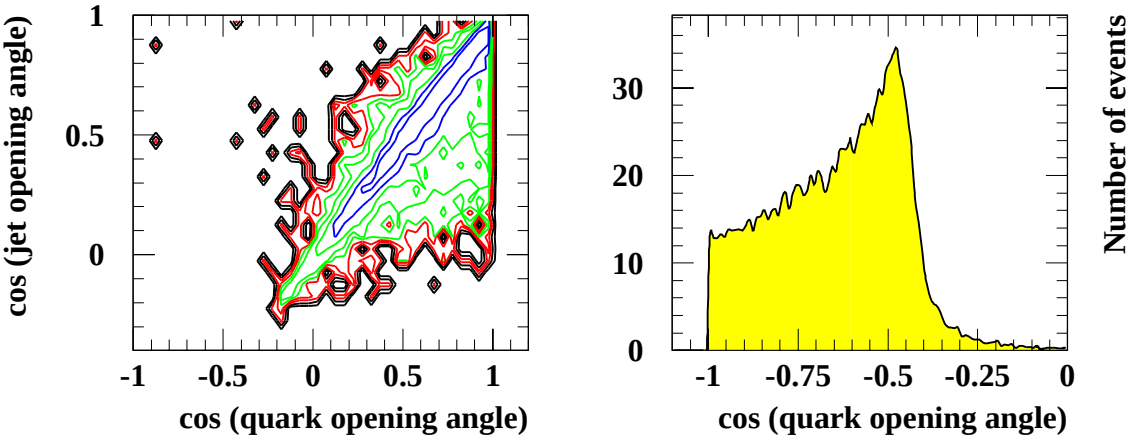

Figure 4.3: *Left) KORALW description of the correlation between minimum jet opening angle, and the minimum quark opening angle in hadronic events, showing smearing at small quark opening angles. Right) KORALW description of the cosine of opening angle of quarks with the same parent W.*

This suggests that events which have the potential to yield larger colour reconnection effects look more like the background QCD events, and therefore could be more difficult to select. The smallest jet-jet opening angles' dependence on the neural network output (*outnn*) was studied, and it was discovered that generally, smaller angle events tended to be found in the background region, and were being rejected by the W mass and WW cross-section analysis cut of $outnn > -0.3$. In order to reclaim these events, it is essential to make a softer cut on *outnn*. A cut of $outnn > -0.9$ was chosen because the purity can be seen to drop quite sharply[7] for cuts any softer than this. Moving into this region would bring very little benefit, but the region $-0.9 > outnn > -0.3$ is certainly worth examining because the background is not too large, and also the signal contains many small angle events.

The efficiency of the new, and original selections as a function of the jet

[7]See Figure 4.1.

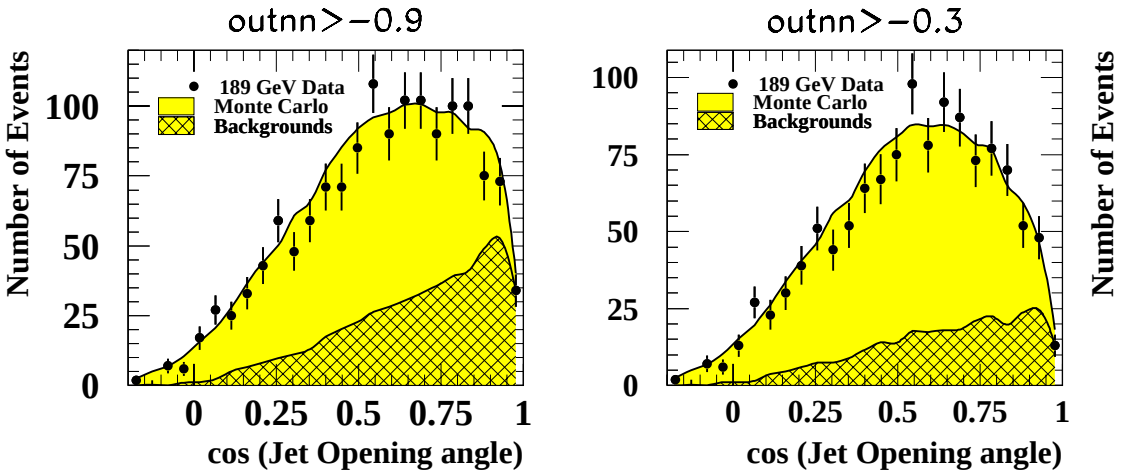

Figure 4.4: *Opening angle of jets from different W decays for selected hadronic events, for (left) new selection and (right) old selection.*

opening angle are shown in Figure 4.2. This indicates that we are now selecting more small angle events than previously. To reinforce this point further, the distribution of the jet opening angle for both selections is shown in Figure 4.4, which shows the increase in the number of events selected in the small angle region but the increased background in the new selection also. The deterioration of the distribution at small angles is believed to emanate from the jet-finding algorithm's failure to correctly resolve the two parton systems. This smearing from small quark angles to larger jet angles can be seen on the left of Figure 4.3 for simulated WW hadronic events.

4.2.3 $W^+W^- \to e\nu q\overline{q}$, and $W^+W^- \to \mu\nu q\overline{q}$ Event Selections

Electron and muon events [54, 55] are characterised by the following: a high energy isolated lepton, a large missing momentum (from the neutrino) roughly[8] opposite the lepton, and two hadronic jets. Due to its rather unique signal, it is relatively straight-forward to obtain a fairly pure sample of semi-leptonic events, based mainly on the lepton identification, and the missing momentum vector.

[8]The angular separation of the lepton and neutrino lies between 120^o and 180^o and follows a similar distribution displayed on the right of Figure 4.3.

However, there are still backgrounds rising from $e^+e^- \rightarrow \mathrm{Z}^0\mathrm{Z}^0$, $e^+e^- \rightarrow \mathrm{Z}^0ee$, and $e^+e^- \rightarrow \mathrm{Z}^0/\gamma \rightarrow q\overline{q}(\gamma)$. It is worth noting that the $q\overline{q}(\gamma)$ events can be more similar to the signal appearance-wise, due to the ISR photon producing missing energy and momentum in the event and there being two none anti-parallel jets.

Pre-selection

Events are first selected to be *class 16* events[9], then the missing momentum and missing energy are used to discriminate between the signal and background with the equation below [56],

$$\not{p}_3 < maximum \left(\begin{array}{l} \sqrt{s}\left(1 - \frac{m_Z^2}{s}\right) - \sqrt{|\not{E}^2 - \not{p}_T^2|} - 6.0 \\ \frac{\sqrt{s}}{2}\left(1 - \frac{m_Z^2}{s}\right) - 27.5 \end{array} \right), \tag{4.1}$$

where $\not{p}_3$ is the z component of the missing momentum vector, $\not{p}_T$ is the transverse missing momentum, and $\not{E}$ is the missing energy of the event. This cut essentially uses the different angular distribution of the missing 4-vectors in the detector between the signal and the backgrounds. Also, it automatically scales to whichever centre-of-mass energy is being analysed. The pre-selection is more than 99% efficient and approximately 6% pure.

Lepton Identification

The candidate lepton is taken to be the charged track which has the highest momentum component anti-parallel to the missing momentum vector; this is the best estimate of the neutrino direction. At centre-of-mass energies above threshold, the neutrino and lepton do not have to be produced back-to-back due to the boost of the W; however, this method is still found to be extremely efficient [56]. In background events, the lepton candidate track tends to have rather different properties to that of the signal, thus making it relatively easy to discriminate between the two. Firstly, it is less likely that a background track will

[9] *class 16* events are described in the hadronic pre-selection on page 67.

pass lepton identification criteria, and secondly, they are usually low energy and poorly isolated, while in signal events the track is of higher energy and isolated.

Lepton identification criteria [53, 56] are imposed on the lepton candidate to separate the electron and muon channels and to help further eliminate backgrounds. For the electron, these criteria consist of momentum exceeding 2GeV, and then comparing $\frac{dE}{dx}$ measurements in the TPC and shower profiles in the ECAL, to those expected for an electron. The muon identification is based on the information from the muon chambers, and from consistent shower profile checks in the HCAL for tracks exceeding 3GeV. Events with lepton candidates which fail these criteria are discarded.

The electron is then corrected for Bremsstrahlung by adding the 4-vectors of photons within 2.5^o of the electron deposit in the ECAL to the electron track, but only if there is a total energy of less than 5GeV deposited within a 6^o cone of the electron. This requirement is to establish that the electron is isolated. A similar correction is made for final state radiation (FSR) in both electron and muon events. Care is taken to identify photons as FSR, and not ISR, or simply originating from a hadronic jet, by imposing the condition that it is not near the beam-line or a hadronic jet. The final corrected lepton energy must now exceed 21GeV.

The isolation of the lepton[10], its corrected energy, and the total missing transverse momentum are used to discriminate signal and background by calculating an event probability from a three-dimensional probability distribution function (pdf)[59, 60]. Finally, a cut of greater than 0.4 is placed on this event probability in order to determine electron and muon semi-leptonic events. This gives a final efficiency and purity at 183GeV of 82.4% and 89.9% for the $e\nu q\overline{q}$ channel, and 84.9% and 95.0% for the $\mu\nu q\overline{q}$ channel.

[10]The isolation of the lepton, I, is defined as $\mathrm{I} = \log(\tan(\alpha_{\mathrm{jet}}/2)) + \log(\tan(\alpha_{\mathrm{ch}}/2))$, where α_{jet} and α_{ch} are the angles between the lepton, and the nearest jet or charged track, respectively.

4.2.4 $W^+W^- \to \tau\nu q\overline{q}$ Event Selection

It is more difficult to select tau ($\tau\nu q\overline{q}$) events than it is to select the other two lepton flavours because the tau lepton decays into one or more neutrinos, and an odd number of lower energy charged tracks. This affects the reconstruction of both the tau neutrino, and the tau trajectories. The missing momentum vector need no longer be anti-parallel to the tau direction, nor is it a good approximation of the tau neutrino direction due to the presence of the other neutrino(s). The trajectory of the tau lepton is also more difficult to reconstruct than the isolated high energy electron or muon was, as essentially it is now just another jet.

The selection is based on global event variables and a topological search for a τ jet. An event is selected if it passes the pre-selection, and then either the topological or the global cuts. The event must also *not* be selected as an electron or muon event.

Events first undergo a pre-selection, which consists of:

- *class 16* event;
- the number of charged tracks must be larger than 6;
- the total energy deposited in a 30^o cone around isolated neutrals must be non-zero;
- the total energy deposited in a 12^o cone around the beam-pipe must be less than 2.5% of the centre-of-mass energy;
- the missing momentum vector must have a polar angle satisfying $|\cos\theta| \leq 0.95$;
- the acolinearity[11] of the event hemispheres must be less than 170^o.

The global event property cuts are as follows:

- the acoplanarity[11] of the event hemispheres must be less than 175^o;
- sum of momenta of tracks located in a wedge of half angle 30^o centred on the missing momentum direction in the xy plane must be less than 12.5% $\sqrt{s}$;

[11]Defined in Appendix A.1.

- maximum energy deposited in a cone of 20^o around the missing momentum vector must be 2.5% $\sqrt{s}$;
- primary neutrino energy estimated to be smaller than 65GeV;
- a visible mass cut, $80 < M_{vis} < 140\text{GeV/c}^2$;
- missing mass < 80GeV.

The topological method locates a tau jet, which consists of 1 to 3 tracks, and is the most anti-parallel jet to the missing momentum. The following cuts are also imposed:

- sum of charged track momenta in tau jet must be above 2.5% $\sqrt{s}$;
- the minimum allowed angle between the tau jet and any other jet is 25^o;
- maximum energy of quark jet must be less than 65GeV;
- acolinearity of quark jets must be greater than 110^o;
- invariant mass of the quark jets must be greater than 60GeV;
- energy in a wedge centred on the missing momentum direction $< 20\%$ $\sqrt{s}$.

The $\tau\nu q\overline{q}$ selection is seen to be more than 65% pure, and approximately 60% efficient for the 183GeV LEP run during the summer of 1997.

4.2.5 Jet Containment

A further cut is added to all the events selected, irrespective of the channel, which requires that all jets be well contained within the experimental apparatus. The additional constraint of jet containment is applied because the aim of the analysis is to study event multiplicities and track momenta. However, it is clear that events with one or more jets lying in the beam-pipe region will produce spurious results requiring large efficiency corrections, due to tracks not being detected. Events of this type are included in the original event selections and therefore have to be removed by imposing the requirement that $|\cos\theta_{jet}| < 0.9$, for all jets in the event; θ_{jet} is the polar angle of the jet-vector. It is found that

roughly 12% of selected events in any channel will fail this cut, thus reducing the selection efficiencies.

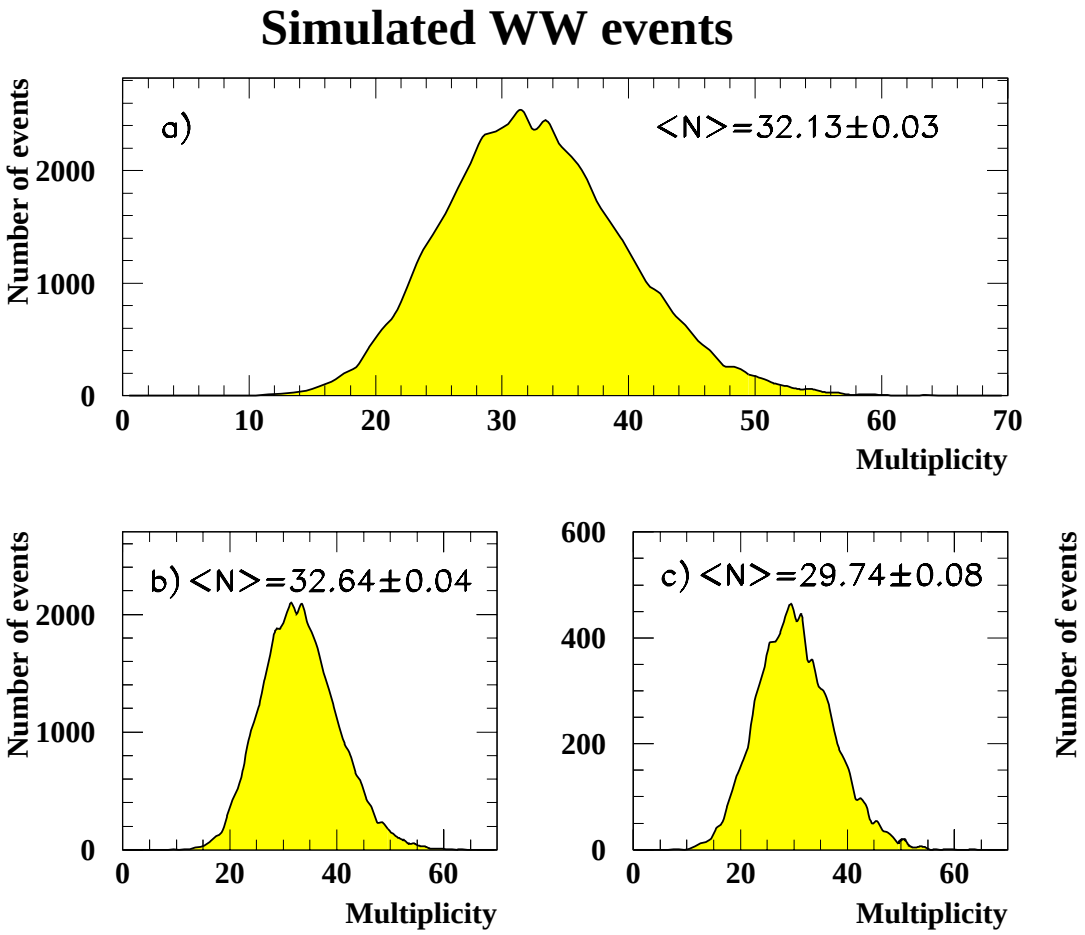

Figure 4.5: *Multiplicity distributions for reconstructed WW hadronic events produced by the KORALW Monte Carlo; a) all simulated events, b) events with all jets well contained, ($\cos\theta_{jet} < 0.9$), c) events with one or more jets failing containment cut ($\cos\theta_{jet} > 0.9$), showing the fall in the number of tracks for events with a jet near to the beam-line.*

4.3 ALEPH data recorded during 1997, 1998 and 1999

Energy	**183GeV**	**189GeV**	**192GeV**	**196GeV**	**200GeV**	**202GeV**
Lumi (pb^{-1})	56.81	174.20	28.93	79.86	86.28	41.89
data N_{evt}^{semi}	288	926	148	405	417	190
data N_{evt}^{had}	490	1429	272	672	685	332
MC N_{evt}^{semi}	304.14	926.87	154.85	412.84	410.45	193.63
MC N_{evt}^{had}	467.85	1575.28	260.35	719.82	760.28	377.72
back N_{evt}^{semi}	13.43	53.34	9.67	25.10	22.40	10.60
back N_{evt}^{had}	142.98	524.27	84.43	227.94	230.82	119.55
efficiency semi	66.7%	62.1%	61.0%	57.8%	53.5%	50.5%
efficiency had	77.3%	78.6%	78.2%	76.9%	76.5%	76.1%
purity semi	86.8%	85.6%	85.2%	85.5%	85.8%	85.4%
purity had	69.4%	66.7%	67.6%	68.3%	69.6%	68.4%

Table 4.1: *Number of events selected in data and predicted number in MC and backgrounds.*

During 1997, an integrated luminosity of 56.81 ± 0.11 pb^{-1} was recorded by the ALEPH detector at a mean centre-of-mass energy of 182.655GeV. Collectively, this data sample is referred to as the 183GeV data, but it actually consists of 0.1661pb^{-1} at 180.83GeV, 3.9241pb^{-1} at 181.72GeV, 50.7945pb^{-1} at 182.69GeV, and 1.9270pb^{-1} at 183.81GeV.

The 189GeV data-set recorded during 1998 consisted of 174.20 ± 0.20 pb^{-1} at a mean centre-of-mass energy of 188.628 ± 0.20 GeV. Further details of the ALEPH LEP2 data-sets can be found at [61].

In 1999 data was recorded at four energies, 192GeV, 196GeV, 200GeV and 202GeV. More specifically this data-set consisted of 28.931 ± 0.083 pb^{-1} at 191.584GeV, 79.857 ± 0.141 pb^{-1} at 195.519GeV, 86.277 ± 0.150 pb^{-1} at 199.516GeV

and 41.893 ± 0.106 pb^{-1} at 201.625GeV.

Table 4.1 shows the number of selected hadronic and semi-leptonic events for the six data samples and the number predicted by the fully reconstructed detector level simulation; remembering that this means the KORALW/JETSET sample plus all the background processes.

4.4 Analytical Method

Given the data and Monte Carlo samples of selected hadronic and semi-leptonic events, momentum distributions and multiplicities are obtained as follows:

1. Good charged tracks are selected to avoid modelling systematics.

2. Charged track momentum distributions are obtained for the hadronic and semi-leptonic channels. The semi-leptonic distribution only includes particles from the hadronic part of the event; any charged tracks from the leptonic decay are ignored.

3. The data momentum distributions are corrected for detector inefficiencies and background impurities using the Monte Carlo simulation, but not for the topological bias introduced by the event selections, or for missing particles which have momentum transverse to the beam-line, p_t, of less than 200MeV.

4. The ratio of the hadronic to twice the semi-leptonic momenta spectra are obtained; it is this variable which is believed to be sensitive to colour reconnection effects. Comparisons with Monte Carlo simulations both with and without colour reconnection are made.

5. Average charged track event multiplicities are calculated by integrating the corrected momentum distributions for both channels; note, particles from the leptonic part of semi-leptonic events are ignored.

6. The difference between the hadronic event multiplicity and twice the multiplicity of the hadronic part of semi-leptonic events is calculated for both the corrected data and the standard simulation[12] because it is believed to be sensitive to colour reconnection effects. The simulation is subtracted from the data to remove any topological bias that may have been introduced by the event selection. The variable should now be compatible with zero if colour reconnection is absent, while most colour reconnected models predict a negative value.

7. Statistical errors and systematic uncertainties will be evaluated.

4.4.1 Charged Track Selection

It is essential to impose criteria for selecting the charged tracks which are to be analysed. This is because the detector and the reconstruction techniques described in Chapter 3 are not perfect. For example, tracks with low momentum, or which form small angles to the beam direction, are generally missed by the detector and any which are seen are not regarded as being reliable. These regions of inefficiency are removed by the following set of cuts, which define a 'good' charged track:

- $\mathbf{N}_{TPC} \geq 4$. The number of hits in the TPC used to reconstruct the track must be at least four. This removes random alignments of 2 or 3 hits;

- $|\cos\theta| < 0.95$. The absolute value of the cosine of the polar angle of the track must be smaller than 0.95. This essentially removes tracks which are within an 18^o cone of the beam-line;

- $|d_0| > 2cm$, $|z_0| > 10cm$. The track must originate inside a cylinder centred around the event interaction vertex, of radius 2cm and length 20cm. This

[12]The standard simulation comprises of KORALW v1.02 WW event generator and JETSET v7.4 parton-shower and hadronisation.

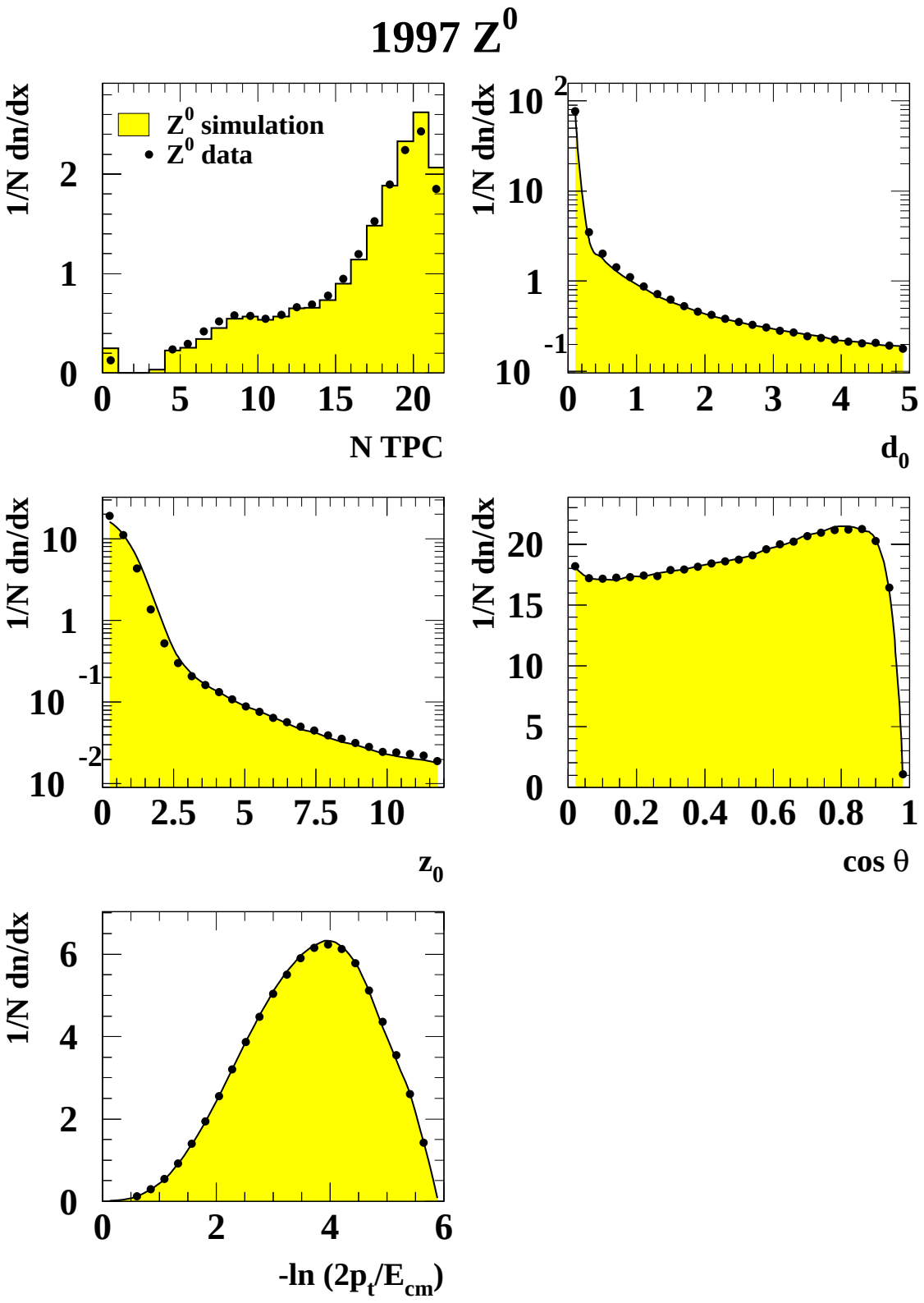

Figure 4.6: *Tracking distributions from 1997 Z^0 data and simulation. Notice, only tracks which pass the other four cuts are entered into a distribution.*

suggests that all tracks were produced from vertices in the centre of the detector;

- $p_t > 200\mathbf{MeV}$. The component of the tracks momentum transverse to the beam-line must be larger than 200MeV. This removes tracks which form multiple spirals inside the tracking detectors.

Monte Carlo simulation predicts that on average, roughly 14% of the total generated hadronic charged tracks are lost from an event after running the event through the detector simulation software. In the data, these tracks are either removed by the above cuts, or else are never even recorded by the apparatus. The distributions of these five charged track selection criteria are shown for the 1997 Z^0 data and Monte Carlo samples in Figure 4.6.

4.4.2 Data Correction

After events have been selected and tracks from those events chosen, it is clear that there will be a set of signal events and tracks which will not have been analysed. These events/tracks fall into particular regions of phase-space which are difficult to obtain for various reasons. Also present in this selected sample will be a set of events originating from the background processes. It is clear that these two factors will have an adverse effect on any results obtained. It is therefore a necessity to correct the data using the Monte Carlo simulation; this is achieved via a bin-by-bin correction of the momentum distribution. However, two limitations must be addressed:

1. If colour reconnection is present in the inefficient regions of the hadronic event selection, then correcting for the effect of these missing events using standard Monte Carlos is not going to recover any information about its effects. In fact, it is possible that any small effects present may be removed. The same argument holds true if the correction is done using a colour re-

connected Monte Carlo model - that the results will depend on the model chosen.

2. The tracks which are most susceptible to the effects of colour reconnection lie in the low momentum region, which includes tracks that the detector is not physically capable of recording. Simple Monte Carlo studies[13] have shown that the fall of the distribution at low particle momenta is essentially due to the track momentum transverse to the beam-line, p_t, cut imposed in the track selection. Any corrections to the number of tracks obtained in this region of phase-space by a standard or colour reconnected Monte Carlo will merely result in a statement about the model itself.

To make explicit event selection inefficiency limitations, no corrections are made to the data for the topological bias introduced by the event selection. This applies to both the hadronic and the semi-leptonic channels. However, events lost due to the event containment criteria are corrected for as there is no suggestion that colour reconnection is dependent on the minimum jet polar angle. Corrections for the unwanted background included in the sample are made by simply subtracting the amount of background predicted in the Monte Carlo, from the data collected. Track selection inefficiencies are corrected to an acceptance limited by the criteria that only tracks with a true transverse momentum, p_t, greater than 200MeV, are included. This means that all the 'good' charged track cuts/inefficiencies are corrected for, except transverse momentum [62].

For each Monte Carlo sample and the data, a detector level ξ distribution is produced for both hadronic and semi-leptonic channels. ξ is defined by,

$$\xi = -\ln(x_p), \tag{4.2}$$

where x_p is the scaled momentum of a particle,

$$x_p = \frac{2p_i}{\sqrt{s}}, \tag{4.3}$$

[13]See Figure 4.7.

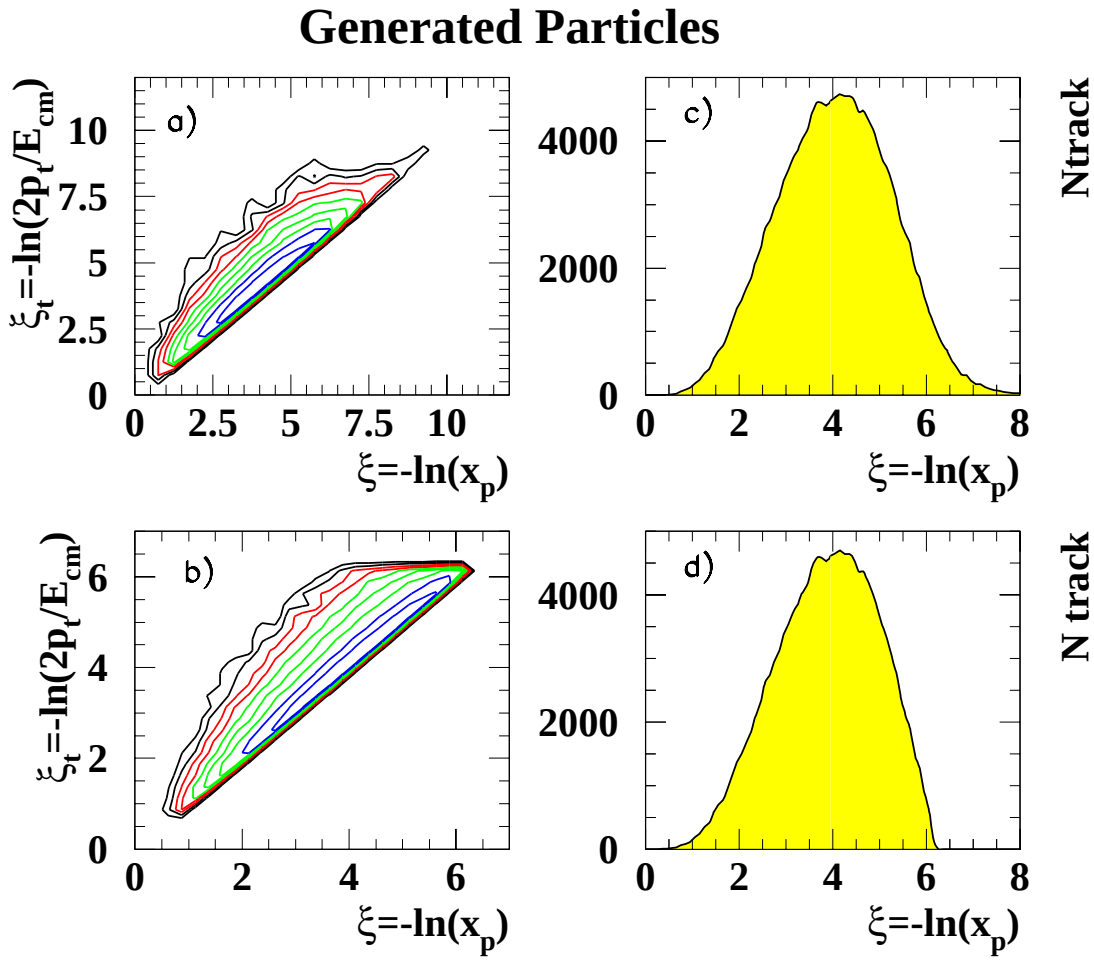

Figure 4.7: *Generated particle momentum distributions to show dependence of* $\xi = -\ln(x_p)$ *on transverse momentum, here plotted as* $\xi_t = -\ln(2p_t/E_{cm})$*. The contour plots show the correlation between* ξ *and* ξ_t*, a) for all true particles and b) for all particles with true* $p_t > 200 MeV$*. Plot c) shows the* ξ *distribution for all true generated particles, and d) shows the distribution with a cut at* $p_t < 200 MeV$*.*

if p_i is the total momentum of the particle i, and $\sqrt{s}$ is the centre-of-mass energy of the e^+e^- collision. The semi-leptonic distribution only includes particles from the hadronic part of the event; any charged tracks from the leptonic decay are ignored.

Subsequently, each Monte Carlo ξ distribution is normalised bin-by-bin, to the luminosity of the appropriate data sample, via,

$$n_{mc}^{ex} = \frac{L_{data}}{L_{mc}} n_{mc}. \tag{4.4}$$

Where n_{mc}^{ex} is the expected number of tracks in the data as predicted by Monte Carlo, n_{mc} is the number of tracks from the original Monte Carlo sample, and L_{data} is the luminosity of the data recorded. L_{mc} is the equivalent luminosity of the Monte Carlo sample, which is calculated from the theoretical cross-section of the sample and the number of events generated in the sample, so that,

$$L_{mc} = \frac{N_{gen}}{\sigma_{mc}}. \tag{4.5}$$

The luminosity normalised ξ distributions of the simulated backgrounds are now added together bin-by-bin to obtain a total predicted background distribution. Care is taken to include non-signal WW events even though it is from the same Monte Carlo sample as the signal. A Monte Carlo reconstructed detector level distribution, ξ_{rec}^{mc}, is obtained from the sum of the signal, ξ_{signal}^{ww}, and the total background Monte Carlos, which can now be compared directly with the detector level data distribution, ξ_{rec}^{data}, where,

$$\xi_{rec}^{mc} = \xi_{signal}^{ww} + \left(\xi_{zz} + \xi_{zee} + \xi_{qcd} + \xi_{back}^{ww}\right), \tag{4.6}$$

(the term in brackets is the total reconstructed detector level background distribution, ξ_{back}^{mc}). The agreement between data and the fully reconstructed Monte Carlo is seen to be good, at both 183GeV (Figure 4.8), and 189GeV (Figure 4.9).

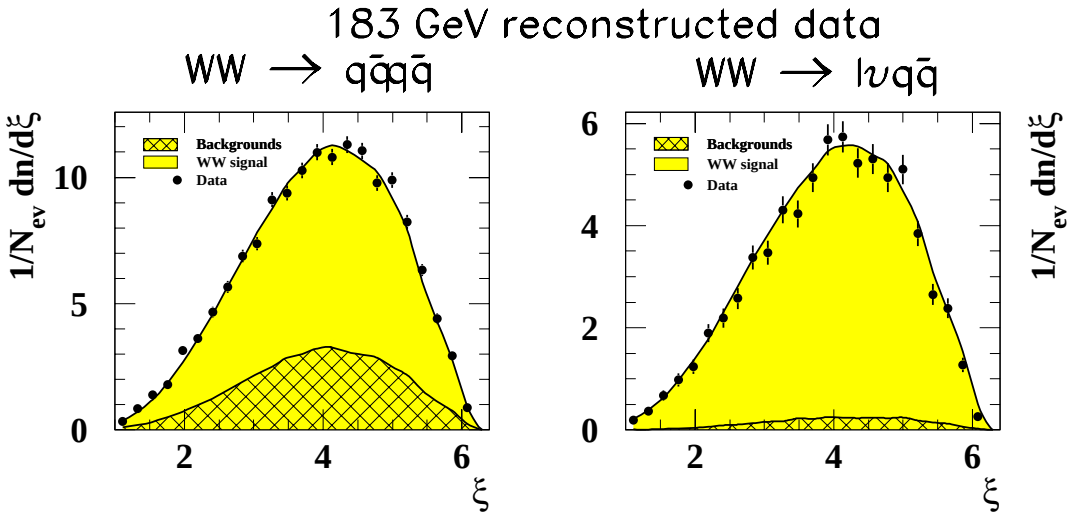

Figure 4.8: *ξ distributions for semi-leptonic and hadronic detector level 183GeV data, with fully reconstructed Monte Carlo and background. Error bars are statistical only.*

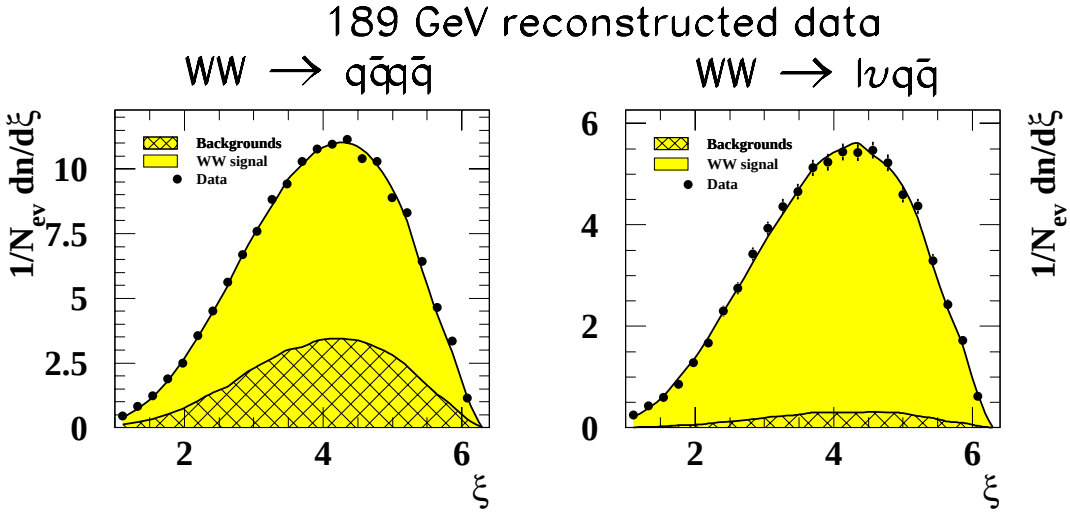

Figure 4.9: *ξ distributions for semi-leptonic and hadronic detector level 189GeV data, and fully reconstructed Monte Carlo and background. Error bars are statistical only.*

The background distribution, ξ^{mc}_{back}, is subtracted from the detector level data distribution ξ^{data}_{rec}, bin-by-bin to produce the background subtracted data distribution,

$$\xi^{data}_{backsub} = \xi^{data}_{rec} - \xi^{mc}_{back}. \tag{4.7}$$

This is the first step of the data correction procedure. The background subtracted data distribution, $\xi^{data}_{backsub}$, and its comparable Monte Carlo, the reconstructed WW signal, ξ^{ww}_{signal}, are normalised bin-by-bin to a differential cross-section, via,

$$n'_i = \frac{1}{N_{ev}} \frac{dn_i}{d\xi_i}. \tag{4.8}$$

Where, n'_i is the number of normalised entries in bin i of the ξ distribution in question, N_{ev} is the number of events that relates to the sample (following the same luminosity and background subtraction criteria as the distribution). dn_i and $d\xi_i$ are the number of tracks in bin i and the width of the bin, respectively. The differential cross-section normalisation essentially removes any explicit dependence of the ξ distribution on the number of events obtained in the data, and produces a distribution which is easily comparable to other data samples of different size and energy.

The data is now in a form where it can be corrected for detector inefficiencies using the distribution for all true generated particles in the WW Monte Carlo sample, within the topological acceptance defined by the event selections, ξ^{true}_{accept}. This does not include tracks whose momentum transverse to the beam-line, p_t, is less than 200MeV. This is the second step of the data correction procedure and is achieved via,

$$\xi_{cor} = \xi^{data}_{backsub} \frac{\xi^{true}_{accept}}{\xi^{ww}_{signal}}, \tag{4.9}$$

where ξ_{cor} is the momentum distribution for either hadronic or semi-leptonic WW data events corrected for background contamination and detector inefficiencies, but which is still within the limited acceptance of the event selections and only for tracks with true $p_t > 200$MeV. The hadronic and semi-leptonic ξ_{cor} distributions corrected to this limited acceptance are both displayed at 183GeV and 189GeV in

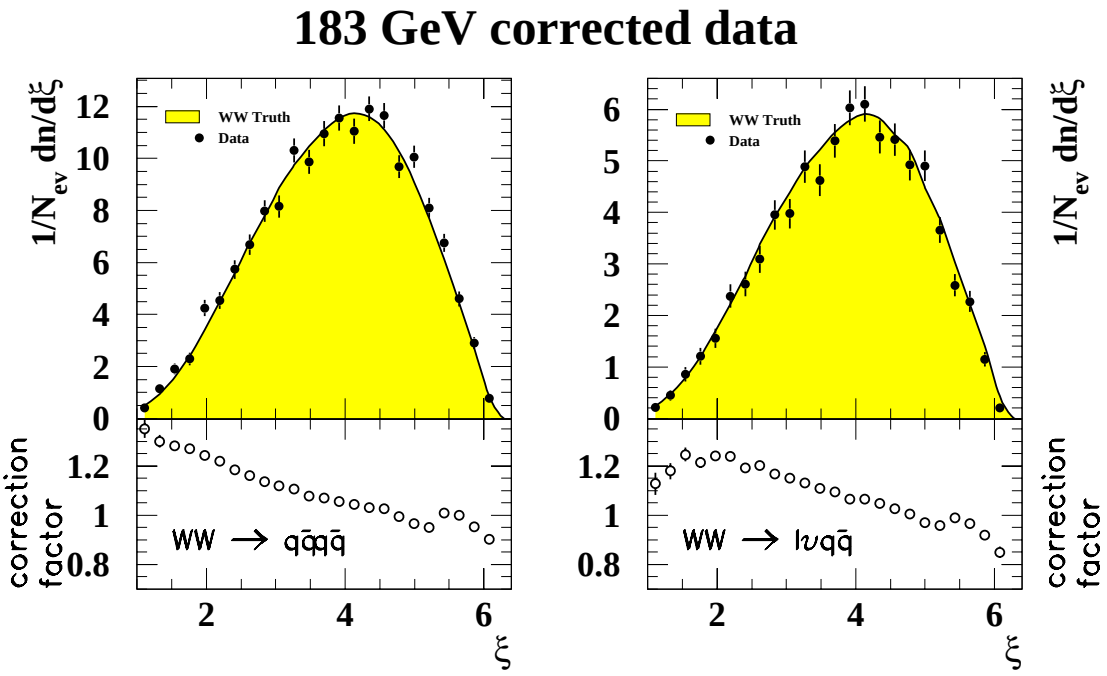

Figure 4.10: *Semi-leptonic and hadronic ξ distributions for 183GeV data, corrected to the limited acceptance defined in the text. The correction factor is the ratio* $\frac{\xi^{true}_{accept}}{\xi^{ww}_{signal}}$. *Error bars are statistical only.*

Figures 4.10 and 4.11; also shown are the correction factors from equation 4.9 for each bin of the distribution. Further distributions of the corrected data against the various Monte Carlo simulations can be seen in Figures 4.17 - 4.24 on pages 110 - 117.

The mean charged track event multiplicity is now calculated from the integral of the appropriate ξ distribution, including the underflow bin, *i.e.* tracks with ξ less than 1; there are no overflows.

$$<N^{ch}>= \int_{-\infty}^{\xi^{max}} \xi \; d\xi = \sum_{i=1}^{n_{bin}} (n'_i \; d\xi_i) + \frac{n^{tk}_{underflow}}{N_{ev}} \qquad (4.10)$$

where $n^{tk}_{underflow}$ is the number of tracks in the sample with $\xi < 1.0$. This number has been normalised by the luminosity, undergone detector inefficiency and background contamination corrections, but has not been normalised to a differential cross-section because the bin width, $d\xi$, is infinite. It must be noted that the semi-leptonic multiplicities are for the hadronic part of the events only, and that any tracks from the leptonic decay are ignored. The quoted multiplicity values

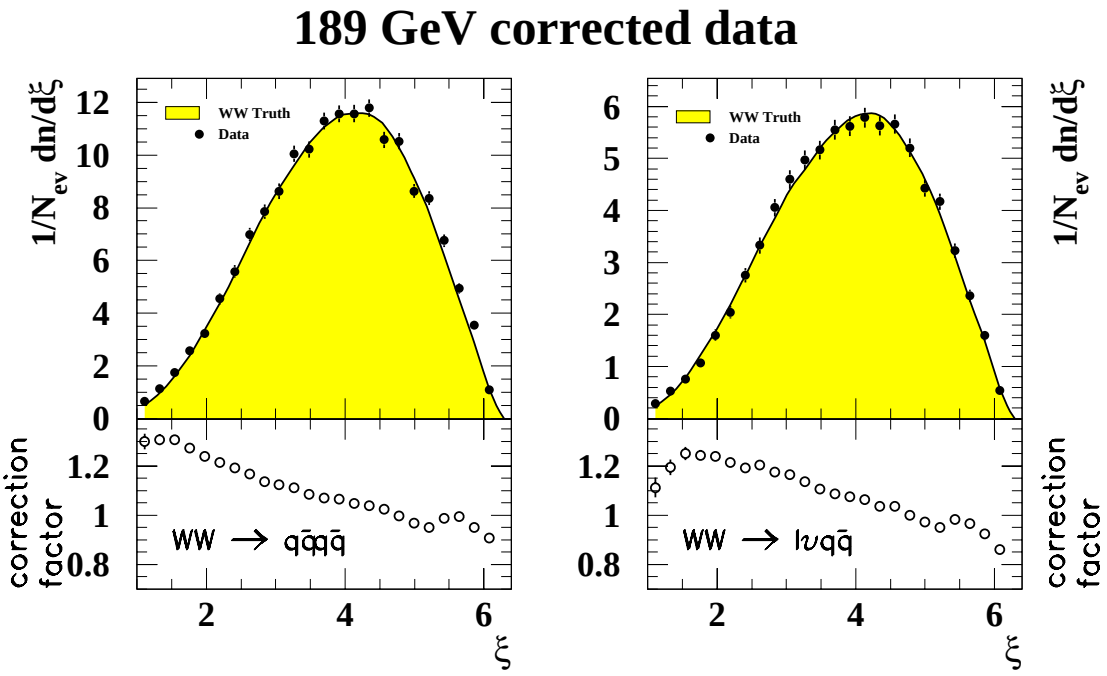

Figure 4.11: *Semi-leptonic and hadronic ξ distributions for 189GeV data, corrected to the limited acceptance defined in the text. The correction factor is the ratio* $\frac{\xi^{true}_{accept}}{\xi^{ww}_{signal}}$. *Error bars are statistical only.*

are calculated from the momentum distributions; they are therefore subject to the same limited acceptance as the distributions which were described earlier.

Now that we have the data multiplicities for both WW channels, $<N^{ch}_{q\bar{q}q\bar{q}}>_{data}$ and $<N^{ch}_{q\bar{q}}>_{data}$, it is possible to construct the difference between the hadronic event multiplicity and twice the multiplicity of the hadronic part of semi-leptonic events, $<N^{ch}_{q\bar{q}q\bar{q}}>_{data} - 2 <N^{ch}_{q\bar{q}}>_{data}$, which is believed to be sensitive to colour reconnection. The reason for this choice of variable is that there is no colour reconnection occurring in the semi-leptonic channel, therefore twice the multiplicity of the hadronic part of these events will be an estimator of the hadronic multiplicity without reconnections. Consequently, a value of zero is naively expected. Yet, most colour reconnection models predict a small negative value, but here there is a problem. There are topological biases in this number due to the experimental acceptance used to calculate them, which could shift the expected value from zero. For this reason, the same variable is calculated using the simulated

multiplicities, $<N^{ch}_{q\bar{q}q\bar{q}}>_{mc}$ and $<N^{ch}_{q\bar{q}}>_{mc}$, to form $<N^{ch}_{q\bar{q}q\bar{q}}>_{mc} -2\ <N^{ch}_{q\bar{q}}>_{mc}$. The Monte Carlo will simulate any topological bias and subtracting the Monte Carlo value from the data will restore the expectation of zero in the absence of colour reconnection. Multiplicity values and related properties for the data samples and Monte Carlos can be found in Tables 4.6 - 4.8, which are displayed in Section 4.7.2.

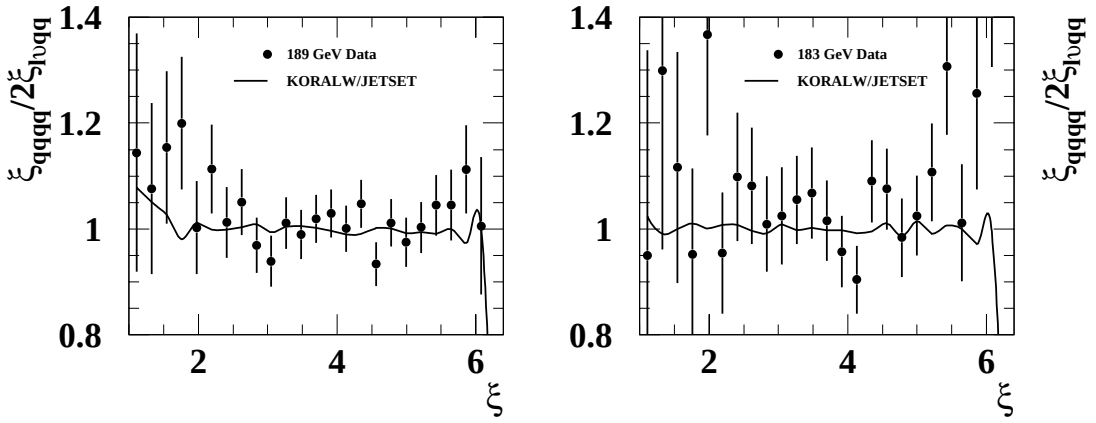

Figure 4.12: *Ratio of hadronic and twice semi-leptonic momentum distributions, for 183GeV and 189GeV data and simulated prediction. Error bars are statistical only.*

The ratio of the momenta spectra for the two WW channels is produced for both the corrected data, $\frac{\xi^{cor}_{q\bar{q}q\bar{q}}}{2\xi^{cor}_{l\nu q\bar{q}}}$, and the WW generated signal Monte Carlo, $\frac{\xi^{true}_{q\bar{q}q\bar{q}}}{2\xi^{true}_{l\nu q\bar{q}}}$. It is this distribution where the effects of colour reconnected models will be most apparent. The reason for this choice in variable is that the predicted change in multiplicity due to colour reconnection in the hadronic channel will manifest itself at low momenta. This will not be present in the semi-leptonic distribution, therefore, a deviation of the ratio from unity at low momenta could be seen as evidence for colour reconnection. Notice that any topological bias introduced may also shift the ratio from unity, however, this is modelled in the simulation which is also plotted as a ratio. Figure 4.12 shows the ratio plot for the data and the simulation at both 183GeV and 189GeV. Further distributions of the data ratio against the various Monte Carlo simulations can be seen in Figures 4.17 -

4.24 on pages 110 - 117.

This procedure is repeated for all of the WW Monte Carlo models, with and without colour reconnection present, though the main analysis and final results quoted use KORALW/JETSET as the standard simulation. All of the models are compared with the data, so that they can either be ruled out or found to be compatible. Section 4.7 discusses all the results of this study thoroughly.

4.4.3 Statistical Error

It is clear the statistical errors will need to be propagated throughout this analysis so that the statistical precision of the corrected data can be obtained. This needs to be done for both the ξ distributions and for the multiplicities.

In the case of the Monte Carlo, the procedure is relatively straight-forward because the statistical errors on the number of tracks per bin of the distributions are negligible. This is due to the large statistics used in the Monte Carlo, thus making the statistical error on the bins too small to be seen. The multiplicity error can be calculated directly from the standard deviation of the multiplicity distribution of the generated tracks used to define the acceptance of the final result.

However, there is not an obvious method of obtaining the errors for the corrected data multiplicities, since we are unable to make a multiplicity distribution for the corrected data and therefore, do not know the standard deviation. The straight-forward solution of scaling the error obtained before correction, by the ratio of the corrected data and the raw data multiplicity values, was used as an estimate of the statistical error. The statistical error on the data before correction is obtained from the standard deviation of its multiplicity distribution.

To test this method's validity, it was used on the 189GeV simulation to calculate the statistical error on the true multiplicity. This is compared to the statistical error from the standard deviation on the true multiplicity distribution;

the results are shown in Table 4.2. N_{raw} is the fully reconstructed simulated multiplicity and σ_{raw} is its statistical error (standard deviation). N_{true} is the true WW multiplicity of limited acceptance which the data is corrected to, and σ_{true} is the statistical error from the standard deviation of the multiplicity distribution, (this value is not known for the real data). The calculated statistical error which is an estimate of σ_{true} is given by, $\sigma_{calc} = \sigma_{raw} \times \frac{N_{true}}{N_{raw}}$. Table 4.2 shows that this estimate is good to 3 decimal places.

Simulation	$N_{raw} \pm \sigma_{raw}$	$N_{true} \pm \sigma_{true}$	σ_{calc}	$\lvert\sigma_{calc} - \sigma_{true}\rvert$
WW $\rightarrow q\overline{q}q\overline{q}$	32.0838 ± 0.0367	34.7712 ± 0.0393	0.0398	0.0005
WW $\rightarrow q\overline{q}l\nu$	16.2439 ± 0.0308	17.4076 ± 0.0318	0.0330	0.0012

Table 4.2: *Table showing the difference between the calculated statistical error, σ_{calc}, and the true statistical error, σ_{true}, for the Monte Carlo simulation showing the accuracy of the method used to calculate the statistical error on the corrected data.*

The statistical error on the bins of the ξ distribution are first calculated for the raw data via the usual method, where $\sqrt{n}$ is the error on the n bin entries. These errors are propagated, or scaled following the usual rules as the distribution is normalised and corrected, until the error is obtained for the final distribution.

4.5 Systematic Uncertainties

Systematic uncertainty will arise from any source that is beyond the control of the analysis, or from assumptions or arbitrary decisions made during the analysis. The systematic uncertainties in this analysis are described below.

4.5.1 Tracking Simulation

Uncertainties arise in the final results due to the simulation of the tracking in the detector not being perfect. Once a track selection cut has been applied to remove

inefficient, and usually, badly modelled regions, the selection efficiency may still not be equivalent in data and Monte Carlo. It is clear that we need to attempt to produce a comparable efficiency in both; however, there are two complications to consider:

1. There are limited statistics for WW events selected in the data, therefore, any change to the track selection cuts in the data will contain a statistical component.

2. How is it possible to define an efficiency in the data, when by definition, this requires knowledge of the total number of tracks before the selections? Notably, this will include the unreliable tracks which we are striving to remove in the first place.

These two problems can be solved by analysing hadronic data recorded at the Z^0 mass[14] during the year[15] in which the WW data in question was taken. The data sample consisted of 66761 *class 16* hadronic Z^0 decays and the hadronic Monte Carlo consisted of 97430 events generated by PYTHIA/JETSET and run through the ALEPH event simulation. This sample has very large statistics, and the physics of the Z^0 is well understood, which will aid our study. In fact, the Z^0 data from 1997 was chosen because no major upgrades to the tracking were made for the 1998 data, hence, any results obtained will still be valid for the 189GeV data-set. To reinforce the decision to use Z^0 data, it should be noted that the Monte Carlos are tuned at the Z^0, and then extrapolated to higher energies. This means that the tracking simulation really is being tested accurately by using the Z^0 data sample.

[14]A hadronic event at the Z^0 is selected by simply requiring it to be a *class 16* event, as defined on page 67.

[15]LEP always run at around 91.2GeV at the beginning of every year of data taking so that the experiments can calibrate their detectors with a well understood, high statistics physics sample.

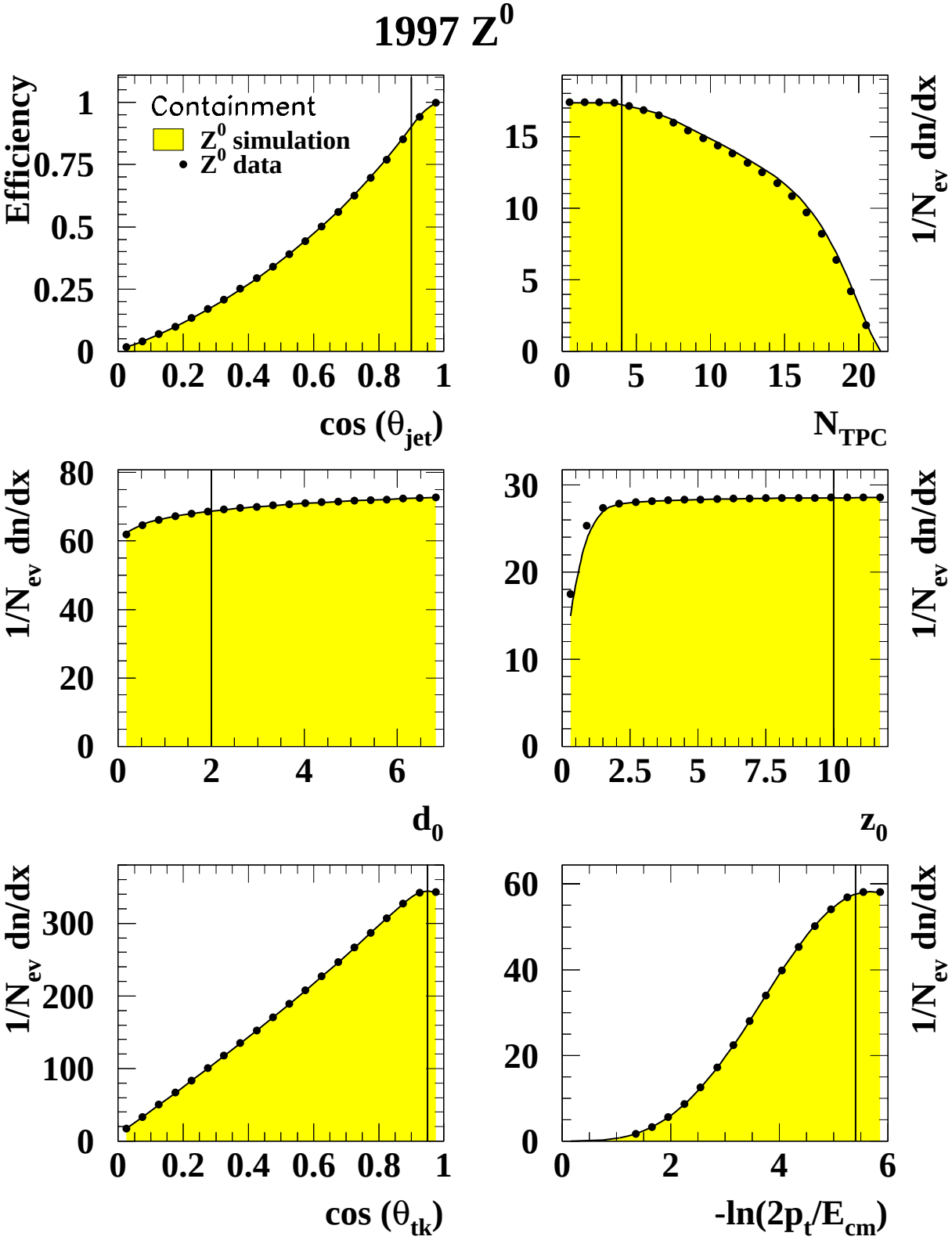

Figure 4.13: *1997 Z^0 data/Monte Carlo comparisons. The top left plot is the event selection efficiency as a function of the containment cut,* $\cos\theta_{jet}$*. The other plots show the integrated number of tracks passing the charged track selection cut as a function of the cut. The line shows the value of the standard cut.*

Selection cut	**Original value**	**New Value in MC**
Containment	0.9	0.8975
TPC hits	4	n/a
$\|d_0\|$	2cm	1.867cm
$\|z_0\|$	10cm	6.64cm
$\|\cos\theta_{tk}\|$	0.95	0.9402
p_t	200MeV	205.5MeV

Table 4.3: *The change in the track (and containment) selection cuts.*

Rather than using the efficiencies of a selection cut, the integrated number of tracks passing the selection cut is used, and assuming that the simulation gives the correct total charged multiplicity, these can be compared in data and Monte Carlo. The position of the cut in the Monte Carlo is then moved until the integrated number of tracks matches those selected in the Z^0 data sample, and the value of the new cut recorded and displayed in table 4.3. The WW analysis is repeated, using each new cut in turn, on the simulation only; any change in the final result is recorded as a systematic. To obtain the total tracking systematic, the systematics for each of the track selection cuts are added together in quadrature ('Trk.' in Table 4.4).

4.5.2 Event Containment

The containment systematic, while being an event property, has much in common with the tracking cuts in terms of its principles, as well as the method used to estimate its effects. It is a pure detector inefficiency effect and is susceptible to statistical fluctuations in the WW data sample. Conveniently, its effects can also be estimated by using the 1997 Z^0 data sample along with its simulation. However, it must be noted that the definition of a jet will have to be changed, though with the intention of retaining some compatibility between high and low

energies.

In the hadronic WW event selection, jets are made by forcing to 4-jets and requiring that $y_{cut}^{ww} < 0.001$, which defines an invariant jet mass, M_{jet}, where, $y_{cut} = \left(\frac{M_{jet}}{E_{cm}}\right)^2$. So, by simply scaling the y_{cut} value using the two centre-of-mass energies while keeping the invariant jet mass constant, a comparable jet definition at the Z^0 is obtained: $y_{cut}^{Z} = 0.004$. The high energy y_{cut} value [63] can be seen to be just beyond the point where the 3-jet rate overtakes the 4-jet rate, while in the low energy case [64], the cut is at the point where the 2-jet rate overtakes the 3-jet rate, which again makes the jet selections appear comparable.

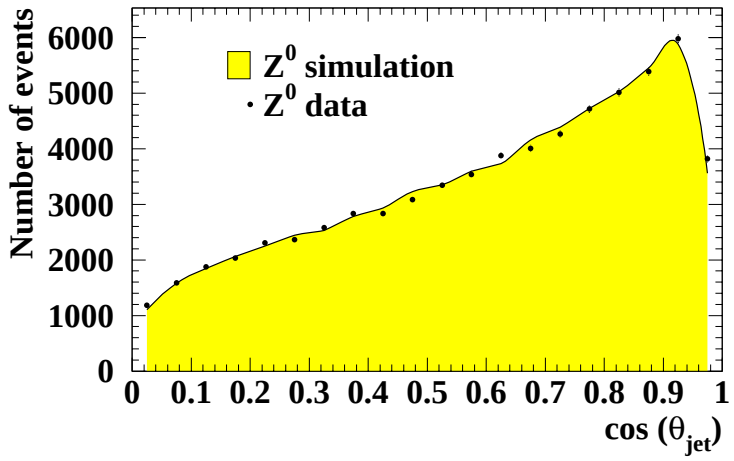

Figure 4.14: *Distribution of cosine of minimum polar angle of jets, mjpol, in 1997 Z^0 hadronic events.*

To obtain an estimate of the uncertainty invoked by forcing all jets to pass a polar angle cut *mjpol*, first, the distribution of *mjpol* is made for data and simulation using 1997 Z^0 events and is shown in Figure 4.14. Assuming the simulation gives the correct $Z^0 \rightarrow hadrons$ branching ratio, then the total integrated number of selected events, shown in Figure 4.13, can be used to define a new cut in the Monte Carlo which reproduces the data selection efficiency. The new cut value is displayed in Table 4.3 and is imposed on the simulation in the high energy analysis; any change in the results is taken as a systematic ('Cont.' in Table 4.4).

4.5.3 Background Simulation

The background contamination in the data sample produces two forms of uncertainty:

1. The mean charged multiplicity of the selected background events need not be similar to that of the signal. Z^0 events are selected by the WW hadronic selection routines, and a difference of 0.54 was found[16] [65] between data and simulation. A value of 0.18 (0.17) is taken as a systematic on the 33% (31%) background in the hadronic WW sample at 183GeV (189GeV).

2. The fraction of background events in the signal can only be estimated by the simulation. Cross-section studies at 183GeV [66] show that the uncertainty in the $q\overline{q}$ cross-section is approximately 3.3%. The QCD background is varied by this fraction, and the change in the final result is taken as a systematic. Since this analysis was conducted, the latest results have been published [67, 68], and the uncertainties are seen to be 2.3% and 1.8%, at 183GeV and 189GeV, respectively. However, it must be noted that the value can be seen as a conservative estimate and is still insignificant when compared to the background multiplicity uncertainty. The total background systematic is displayed as 'Back.' in Table 4.4.

4.5.4 Monte Carlo Model

Uncertainties will arise because of the relatively arbitrary choice of Monte Carlo used to correct the data; also, using a different simulation will produce different results. All the final data results quoted use KORALW as the WW event generator, which has an interface to JETSET to simulate hadronisation effects in order to correct for detector inefficiencies. The analysis is repeated using HERWIG because it is seen as the most significantly different Monte Carlo simulation

[16]This systematic study was not conducted by the author.

from KORALW/JETSET; any change in the results is taken as the uncertainty ('Mod.' in Table 4.4).

4.5.5 Method of Data Correction

Again, the choice to correct the data bin-by-bin in ξ is a relatively arbitrary choice from several other possible methods, using an alternative method will produce different results. A very simple method of correcting the multiplicities is to simply scale the detector level data multiplicity by the ratio of the generated, over the reconstructed level. This is essentially assuming a flat distribution of the correction factors with ξ. The results are shown under 'Meth.' in Table 4.4.

4.5.6 Selection Uncertainties

It is essential to include a systematic for the event selections ('Selec.' in Table 4.4), more so than ever because the acceptance is limited to the events topology favoured by them. The essential method is to identify the main criteria of the selection which will affect the events it chooses, and to then change it by what would appear to be a reasonable amount.

The hadronic neural network has already been changed from its original specifications, as described earlier, therefore changing the cut on the output back to its original value in both data and simulation, is appropriate. The analysis is then repeated so that any change observed in the final results can be taken as a systematic uncertainty.

The electron/muon events are selected by a cut on the probability at 0.4 [56]. However, on inspection, the majority of events are seen to be clustered above probabilities of 0.9, therefore the cut is moved to 0.9 [69, 70] and the analysis is then repeated. Any change in the final corrected results are taken as systematics.

There are large numbers of events selected by both the tau, and the elec-

tron/muon selections. These events are analysed as if they were electrons/muons, rather than as taus, because it is generally felt that this selection is cleaner than the tau selection [71]. This procedure is reversed to obtain a systematic for the tau selection.

The uncertainty in the τ and the e/μ channels are combined to produce one $l\nu q\overline{q}$ selection systematic by adding in quadrature, but allowing for the different number of events selected in each channel,

$$\sigma_{l\nu q\overline{q}} = \sqrt{(f_\tau \sigma_\tau)^2 + (f_{e\mu}\sigma_{e\mu})^2}. \tag{4.11}$$

f_τ and $f_{e\mu}$ are the fractions of selected τ or e/μ events of the full semi-leptonic sample, respectively, and σ_τ and $\sigma_{e\mu}$ are the systematic uncertainties on the two selections, respectively.

4.5.7 Close Track Resolution

It is possible that further uncertainties could arise from the tracking when two tracks are produced very close together. The co-ordinates of the tracks could be confused inside the TPC, leading to the miscounting of tracks, or incorrect momentum measurements. It seems quite plausible that this may be hard to model accurately, and therefore needs to be examined. Early studies on Z^0 data [72, 73, 74] conducted by ALEPH examined this effect and believed it to be of little importance, though there is little evidence to support this. It must also be noted that the track density of WW hadronic events is twice that at 91GeV, and it is therefore unclear that it is still irrelevant, thus an investigation is required.

A suitable method has to be found to measure how close two tracks are to one another. Still, it must be noted that it is not immediately obvious what 'close' means, because clearly, two tracks will tend to diverge. However, it is the TPC hit recognition that is causing the problem. Hence, the distance of closest approach of a fitted track helix to the TPC hit of the track in question is chosen as the variable of interest. The variable is represented schematically in Figure

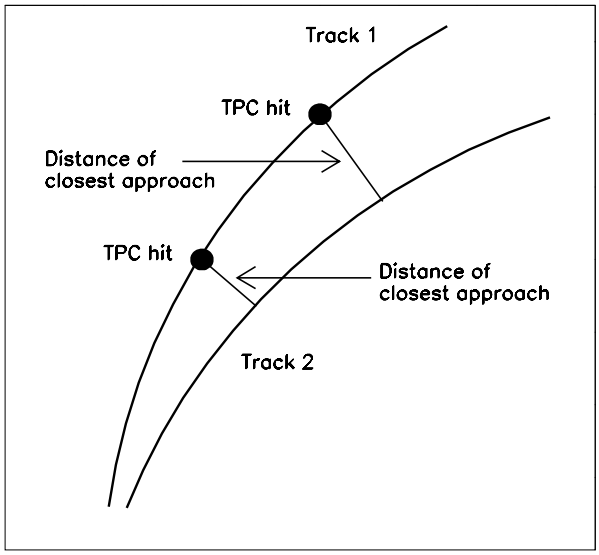

Figure 4.15: *Definition of the distance of closest approach of a fitted track helix to a TPC hit belonging to a separate track.*

4.15. The fitted track helix is chosen because this track may not have a reliable TPC hit on the same pad row as the chosen hit on the neighbouring track, if at all.

Special consideration must be made to 'kinked' tracks, which occur when a hadron decays inside the active tracking volume of the apparatus, thus producing one charged and one neutral particle, which is not seen. The reconstruction algorithm is able to cope with this phenomena and produces two tracks, one before, and one after the kink vertex of similar momentum. However, these fitted helices before and after the vertex can be extrapolated to any point in the detector, which could be a source of confusion when finding the closest fitted helix to a TPC hit on one half of the kinked track. The solution is to ignore the helix from one half of the kink if the TPC hit in question lies on the other half.

The distance of closest approach of a fitted track helix to a TPC hit on another track cannot be calculated directly. It has to be found using an iterative algorithm, which 'swims' along the helix, defined by five parameters, calculating the distance to the Cartesian co-ordinate until it is minimised. The five pa-

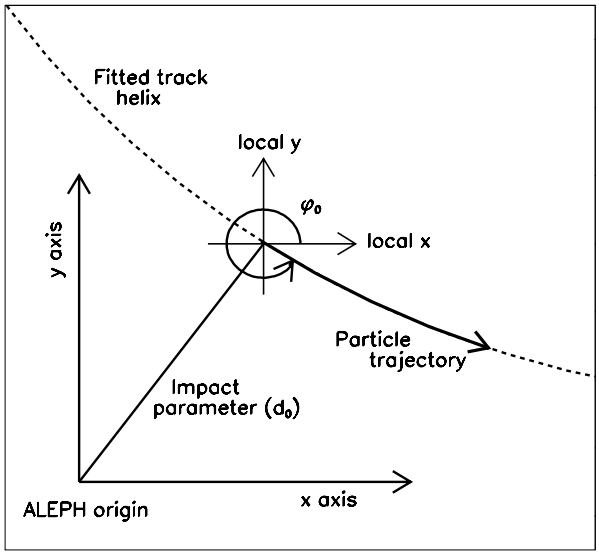

Figure 4.16: *The diagram shows the projection of a helix in the xy plane as viewed from end-cap A, and shows how the particles trajectory can be revealed from knowledge of the impact parameter and ϕ_0. The origin is the local ALEPH event origin, and z runs up out of the page.*

rameters which define a helix are given below, and their meaning is represented schematically in Figure 4.16,

- $\pm\frac{1}{r}$ - The signed inverse radius of curvature, of the circular projection of the helix in the xy plane. The sign infers either a clockwise helix (-ve), or an anti-clockwise helix (+ve), when viewed from end-cap A.

- $\tan\lambda$ - Tangent of the dip angle. λ is the angle the helix makes to the local xy plane.

- ϕ_0 - The ϕ angle that the track makes at the d_0 point, ϕ runs from x to y in the xy plane.

- $\pm d_0$ - Signed impact parameter, which is the r co-ordinate where the circular projection is closest to the z axis. The sign signifies whether the circle encloses the origin (+ve), or not (-ve).

- z_0 - The z co-ordinate where the d_0 point occurs.

The 'swimming' algorithm starts at the d_0 point and moves in 1cm increments around the circle in the xy plane; the new z co-ordinate can then be calculated from the knowledge of $\tan\lambda$. At each position on the helix, the distance to the TPC hit can be found, until it minimises. When this distance is seen to increase, the algorithm moves back two steps and reduces the swim size until the distance of closest approach is found to three significant figures. Verification is made that swimming along the helix does not leave the tracking volume; such tracks will be discarded.

It is now possible to find the track whose helix has the smallest distance of closest approach of all the tracks to a particular TPC hit. A distribution can be made of the closest distance a fitted track approaches a TPC co-ordinate for any of the twenty-one pad rows. The distribution for each of the twenty-one TPC pad rows are displayed in Appendix C, and are examined using the 1997 Z^0 data sample and simulation, as used for the tracking systematic discussed earlier. The distribution is normalised to a differential cross-section and the data/Monte Carlo agreement is not seen to be very good in places. Clearly, a systematic is needed, although the method of applying one is not obvious.

At this stage, it should be noted that the distribution is actually a convolution of two effects: one, the efficiency of a TPC pad row to resolve two tracks as a function of their separation, which is the distribution of interest, and two, a phase-space effect proportional to the area of an annulus centred around the track to which the TPC co-ordinate belongs. Assuming a homogeneous distribution of tracks around the one in question, more tracks will fall in bins at larger separation because the area of the annulus is larger. This effect can be removed by dividing by a factor $2\pi \times rdr$, leaving us with the true two track separation efficiency. However, there are problems with this $2\pi \times rdr$ assumption because tracks are not distributed homogeneously, nor are they parallel, but are confined into jets and spherically distributed within those jets. But, the assumption will only start to break down at large values of the track separation, which are not of interest

here; the aim is to find an area of inefficiency at small separation, where the assumption that the phase-space factor is rising linearly, is true.

Now that the distribution is normalised to $\frac{1}{2\pi N_{evt}} \frac{dn_{tk}}{r(dr)^2}$, it can be seen to fall sharply for separations below 4cm, which is the inefficiency of the TPC to resolve track pairs which are too close together. The fall beyond this region is due to the fewer number of tracks found outside the core of a jet. The distribution for each of the twenty-one TPC pad rows are shown in Appendix C, and all of them are seen to possess a similar shape after the introduction of the $2\pi \times rdr$ factor.

To estimate the systematic, a cut is placed at 2cm, as not only is the distribution showing that we are deep in the region of inefficiency, but also, neither is the simulation a brilliant model of the data. So, any track which has another fitted track within two centimetres of any of its TPC co-ordinates is ignored. The entire WW analysis is repeated following the introduction of this cut, and any deviation is taken as the uncertainty in resolving close track pairs within the TPC ('2-tk' in Table 4.4).

4.5.8 Monte Carlo Tuning

The prediction of the Monte Carlo multiplicity is uncertain due to the precision with which the model was tuned to Z^0 decay multiplicities, and because it is also based on the accuracy to which the multiplicity of uds and c fragmenting Z^0 decays are known. The agreement between mean charged event multiplicities in data and Monte Carlo for Z^0 decays is 0.26 [64]. The measured multiplicities of different flavoured Z^0 decays are as follows: $uds = 20.32 \pm 0.51$ and $c = 21.12 \pm 1.59$, these numbers are -95% correlated [75]. This information produces an uncertainty on the mean multiplicity of a W decay via propagation of the errors in the usual way, and are displayed under 'MC tune' in Table 4.4.

4.5.9 Correlated and Uncorrelated Systematics

Special consideration has to be given to each systematic in turn - whether the semi-leptonic and hadronic uncertainties are correlated or not. This is essential because the uncertainty on the difference of the mean charged multiplicities, $<N_{q\bar{q}q\bar{q}}> -2 <N_{q\bar{q}}>$, is required. Correlated errors arise for reasons independent of the type of event being selected, such as the detector effects of tracking, containment and close track resolution; the Monte Carlo tuning is also correlated. The uncorrelated uncertainties arise from the specific event selection, or from channel related effects such as the simulation model used, or the amount of background in the channel. Correlated errors are subtracted when calculating the error on $<N_{q\bar{q}q\bar{q}}> -2 <N_{q\bar{q}}>$; uncorrelated ones are added in quadrature.

4.5.10 Systematics on Event Multiplicities

The results of all the systematic studies are displayed in table 4.4. The numbers are in units of multiplicity, and in each case for the data, it is the change in the corrected data multiplicity of the channel in question that is entered into the table. The values of the systematics on the difference are calculated as described in Section 4.5.9. The total data error is the sum in quadrature of each column, and it is this value which is assigned to the multiplicity results displayed in Table 4.7 in Section 4.7.2; the Monte Carlo tuning systematic is assigned to the Monte Carlo multiplicities in Table 4.7.

4.5.11 Systematic error bars on ξ distributions

Care is taken to correctly assign the systematic error bar to each bin on the ξ and ratio of ξ distributions. First, the two ξ distributions are considered. For each source of systematic, a new data plot is obtained and any deviation from the original is stored. All the systematics are added in quadrature, along with

Selected	Systematics for 183GeV data							Total	MC
channel	Trk.	Cont.	Back.	Mod.	Meth.	Selec.	2-tk	data	tune
$q\overline{q}q\overline{q}$	0.36	0.20	0.18	0.09	0.01	0.07	0.09	0.47	0.58
$q\overline{q}l\nu$	0.13	0.05	negl.	0.12	0.01	0.11	0.01	0.21	0.29
$4q - 2 \times 2q$	0.10	0.10	0.18	0.15	0.01	0.23	0.07	0.36	negl.
Selected	**Systematics for 189GeV data**							**Total**	**MC**
channel	**Trk.**	**Cont.**	**Back.**	**Mod.**	**Meth.**	**Selec.**	**2-tk**	**data**	**tune**
$q\overline{q}q\overline{q}$	0.41	0.20	0.17	0.05	0.01	0.38	0.01	0.62	0.58
$q\overline{q}l\nu$	0.14	0.05	negl.	negl.	0.01	0.07	0.01	0.16	0.29
$4q - 2 \times 2q$	0.13	0.10	0.17	0.05	0.01	0.40	0.01	0.47	negl.

Table 4.4: *Breakdown of the systematic error for different channels in units of multiplicity.*

the statistical error so as to give the total error, which is plotted along with the statistical error on the plots. Second, the systematics on the ratio of the two ξ distributions are dealt with separately, depending on whether they are categorised as being correlated or uncorrelated. Correlated ones are subtracted, uncorrelated ones are added quadratically; the statistical and total error are both shown on the plot.

4.6 Combination of data samples

An attempt is made to increase the statistical precision of the results by combining the 183GeV, 189GeV, and the four energies recorded in 1999, together. The analysis of the 1999 data was simply conducted[17] by using the same analytical procedure as the 189GeV data, and used an appropriately generated KORALW/JETSET sample for the data corrections. The combination of the six energies was achieved via a statistical error weighted average, given by [13],

$$x_{av} = \frac{\sum_i^n (W_i x_i)}{\sum_i^n W_i} \qquad \text{and} \qquad \sigma_{av} = \sqrt{\frac{1}{\sum_i^n W_i}}, \tag{4.12}$$

[17]The analysis of the four energies recorded in 1999 was conducted as a first year project, by a Lancaster Postgraduate student, Matthew Pearson, who ran the authors code.

where x_{av} and σ_{av} are the weighted average and the statistical error on the average, respectively, of the n values x_i at energy i. The weight of energy i, W_i, is given by, $W_i = \sigma_i^{-1}$, if σ_i is the statistical error on x_i.

The simulations are combined using a luminosity weighted average, x_L which is given by [13],

$$x_L = \frac{\sum_i^n (x_i L_i)}{\sum_i^n L_i}, \tag{4.13}$$

where L_i is the luminosity recorded of the data sample i.

4.7 Results

4.7.1 Momentum Distributions

The 183GeV and 189GeV data/Monte Carlo comparison of the final semi-leptonic and hadronic ξ distributions corrected for detector inefficiencies to the limited acceptance of the event selections and $p_t > 200$MeV, have already been displayed in Figures 4.11 and 4.10, on pages 89 and 88. The ratios of the hadronic ξ over twice the semi-leptonic ξ, at the two energies, have been shown in Figure 4.12 on page 90. These plots used the standard, colour reconnection-free, KORALW/JETSET simulation for the comparisons as well as for the data corrections discussed in Section 4.4.2, and will be displayed again here for completeness, along with the other Monte Carlo simulations available. It should be noted that on the following plots, the data does not change, it is always the result of correcting with KORALW/JETSET.

Figures 4.17 - 4.24 show the 183GeV and 189GeV semi-leptonic (top) and hadronic (middle) corrected ξ distributions, and the ratio of the hadronic over twice the semi-leptonic[18] (bottom). The data (points) includes the total (statistical and systematic) error bar as well as the statistical error (to the horizontal bar). The simulation without colour reconnection is displayed in yellow on the ξ

[18]Remembering that the leptonic part of semi-leptonic events is always ignored.

plots and as a black line on the ratio; the coloured lines show the predictions of colour reconnection models implemented into the Monte Carlo simulation. The models used on the plots are as follows:

- KORALW/JETSET on Figures 4.17 and 4.18;
- EXCALIBUR/JETSET on Figures 4.19 and 4.20, including the three colour reconnection models by Sjöstrand and Khoze;
- ARIADNE on Figures 4.21 and 4.22, including the two colour reconnection models by Lönnblad, and by Gustafson and Häkkinen;
- HERWIG on Figure 4.23 at 189GeV, including the colour reconnection model, there is no HERWIG simulation available at 183GeV.

The 183GeV and 189GeV data are seen to be reproduced by all simulations extremely well in the hadronic and semi-leptonic ξ distributions. The slight excess observed in the data at low momenta ($\xi > 5$), at both 183GeV and 189GeV is also observed in ALEPH data recorded at the Z^0 peak [64]. A lot of work was done in an attempt to tune the Monte Carlo on the Z^0 sample to give a better description of the data in this region, but no solution was found, except at the cost of making the agreement at high momentum far worse [62].

The plots of the ratio are the most interesting because they show the predictions of the colour reconnection models. All of these models suggest that only momenta below approximately 1GeV ($\xi > 4.5$) will be affected, and that the magnitude of the effect will be minimal. In the 183GeV data, there are rather limited statistics and the points are scattered about, though, it still appears likely that a possible excess[19] may be occurring above $\xi = 5$, though this may simply be statistical in nature.

[19]The last point at $\xi = 6.1$ has a ratio value of approximately 1.6 and extends beyond the top of the scale.

The 189GeV ratio plots have much higher statistics than the 183GeV sample, and show a smaller scatter about the standard Monte Carlo prediction of approximately unity. However, there is still insufficient statistical accuracy to establish which model best describes the data as all are seen as being compatible. In addition, note also that the slight excess above $\xi = 5$ is still observed. The HERWIG simulation in the hadronic and semi-leptonic ξ distributions shown in Figure 4.23 can be seen to reproduce the data much better than any other simulation at low momenta, but is worse at higher momenta.

A much larger statistical sample is available by using all four of the 1999 data samples and combining them with the 183GeV and 189GeV samples, as discussed in Section 4.6. The resulting ξ distribution is displayed in Figure 4.24. The datapoints include the systematic error bars produced from the complete study of systematics conducted at 189GeV. The simulation (yellow) is the combination of the KORALW/JETSET samples for each energy, and the coloured lines on the ratio plot (bottom) are the predictions of the most extreme 189GeV[20] colour reconnected models: HERWIG (red), ARIADNE 2 (pink), and EXCALIBUR SK I (green).

The slight excess of the data at low momenta in the ratio plots discussed earlier, is still present after the combination, though the data is still compatible with unity. The errors prevent any clear discrimination between the models, but on this occasion, it is the systematics which are the limiting factor because the statistics have been greatly reduced by the combination. A Pearson χ^2 goodness-of-fit test [76] is conducted on the last ten bins (*i.e.* $\xi > 4$) of the ratio plot for each of the simulations displayed in Figure 4.24, to determine which, if any, can be discarded. The last ten bins are used because this is where all the colour reconnected models are seen to diverge from the standard simulation. It should also be noted that the χ^2 test only takes account of the statistical error and not the total error; because the systematics on the combined data sample are

[20] At the time of writing no colour reconnected samples were available for the 1999 data-sets.

a conservative estimate taken from the study conducted at 189GeV. The χ^2 is given by:

$$\chi^2 = \sum_i^N \frac{(n_i - \nu_i)^2}{\sigma_{n_i}^2}, \tag{4.14}$$

where n_i is the ratio value of the data in bin i of N bins, ν_i is the predicted ratio of the model being tested, and σ_{n_i} is the statistical error on the data in bin i. The normalisation of the theoretical prediction is absolute so that no degrees of freedom for the χ^2 are lost.

Simulation	χ^2**/10 df**	**Probability**
KORALW	1.591	10.2%
EXCALIBUR	1.635	9.0%
SK I	3.952	0.002%
SK II	2.669	0.3%
ARIADNE	0.974	46.4%
ARIADNE 2	1.697	7.5%
HERWIG	1.428	16.1%
HERWIG cr	1.027	41.7%

Table 4.5: χ^2 *and probability for the combined data-set against various simulations in last ten bins of the ratio of hadronic to twice semi-leptonic* ξ *distributions.*

The results of the χ^2 tests are displayed in Table 4.5, and confirm what is clear by examining Figures 4.17 - 4.24; the colour reconnected HERWIG model is the best description of the data at low momentum. Following closely behind is the unconnected version of HERWIG and both ARIADNE models. The reconnected models by Sjöstrand and Khoze do not possess very good agreement, with the observed colour reconnection effect in the opposite direction to that of HERWIG.

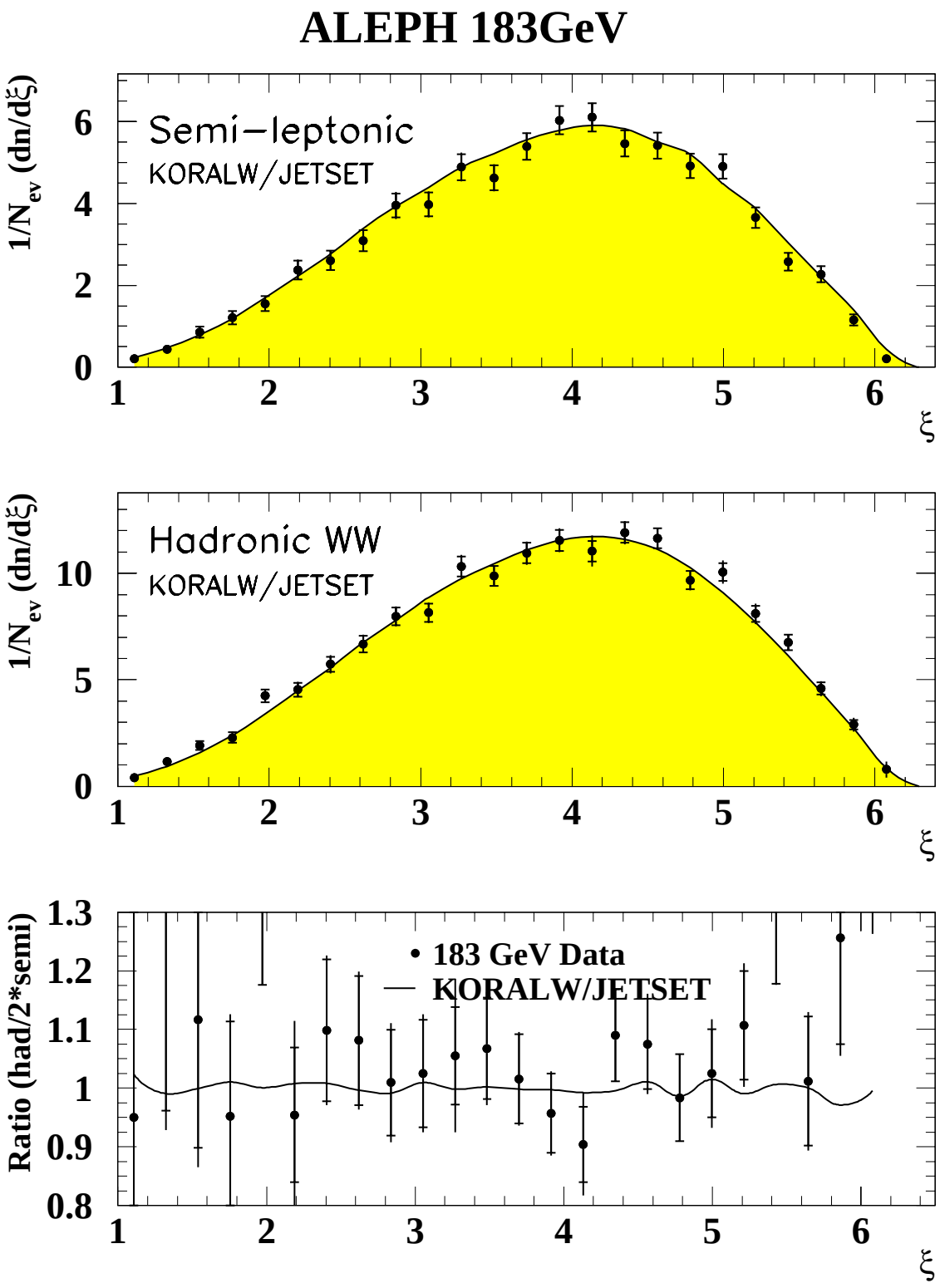

Figure 4.17: *Hadronic and semi-leptonic ξ distributions, and the ratio $\frac{\xi_{q\bar{q}q\bar{q}}}{2\xi_{l\nu q\bar{q}}}$ for 183GeV data with the KORALW/JETSET prediction without colour reconnection.*

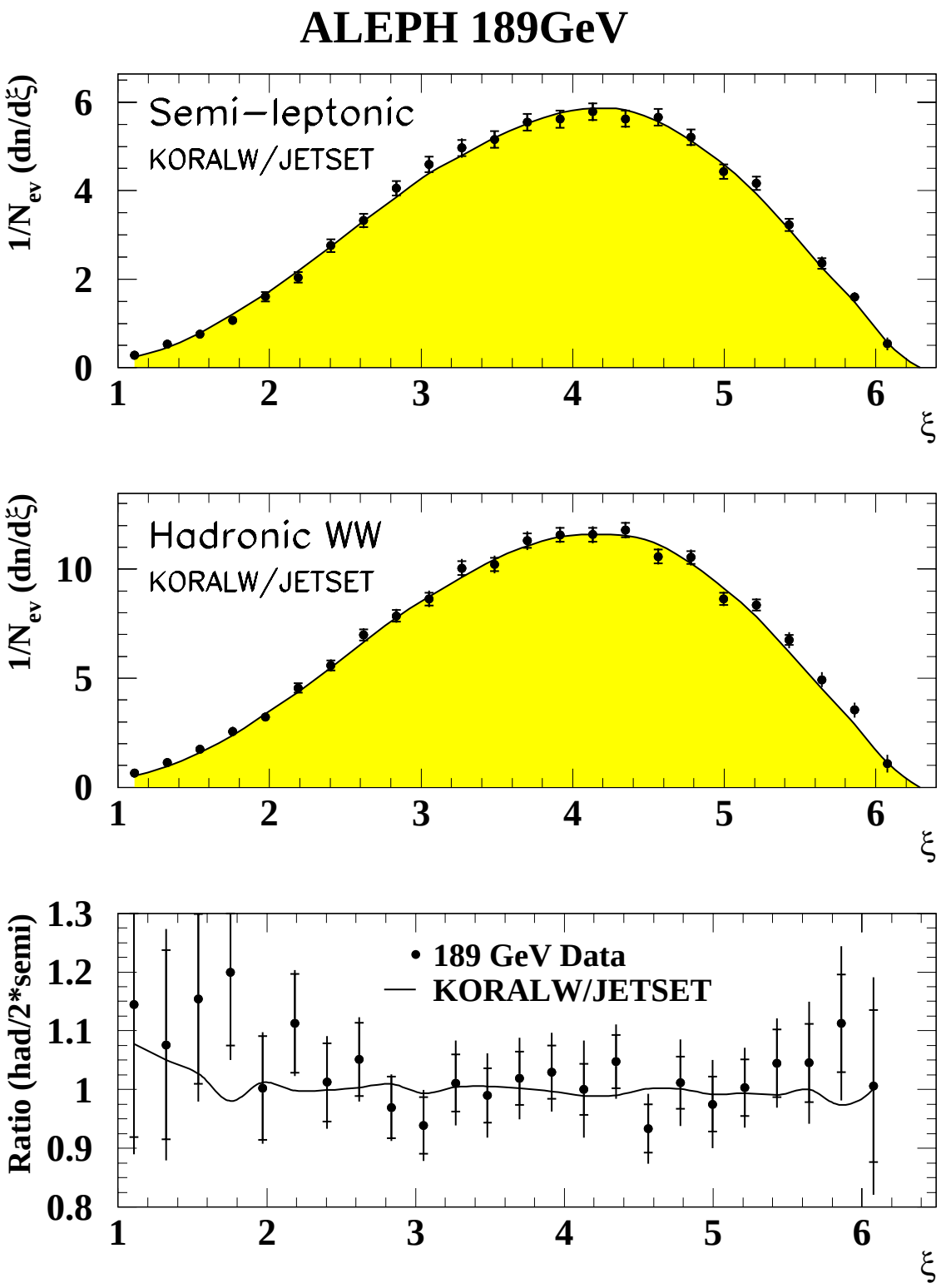

Figure 4.18: *Hadronic and semi-leptonic ξ distributions, and the ratio $\frac{\xi_{q\bar{q}q\bar{q}}}{2\xi_{l\nu q\bar{q}}}$ for 189GeV data with the KORALW/JETSET prediction without colour reconnection.*

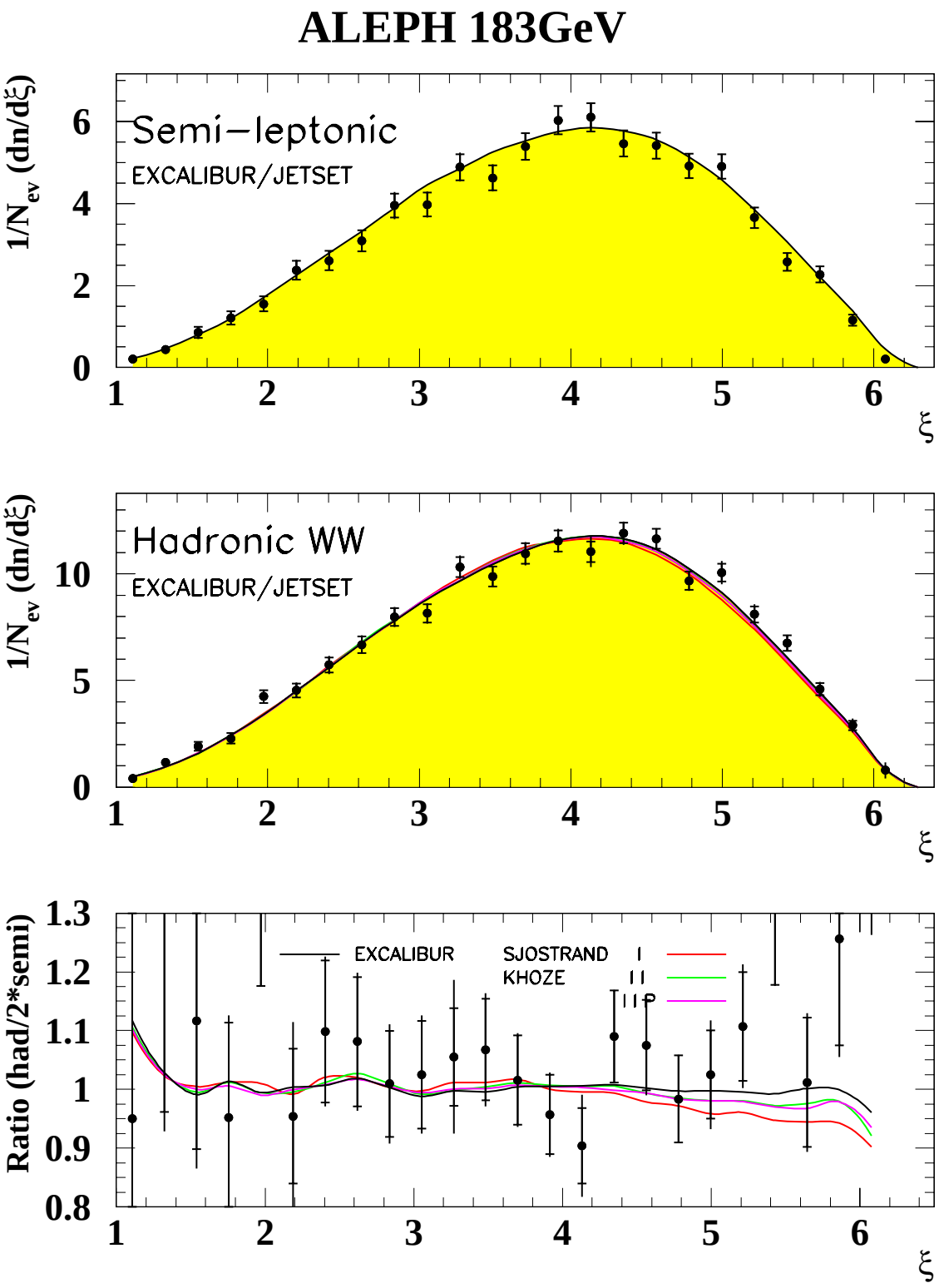

Figure 4.19: *Hadronic and semi-leptonic ξ distributions, and the ratio $\frac{\xi_{q\bar{q}q\bar{q}}}{2\xi_{l\nu q\bar{q}}}$ for 183GeV data with the EXCALIBUR/JETSET prediction with and without the three colour reconnection models by Sjöstrand and Khoze.*

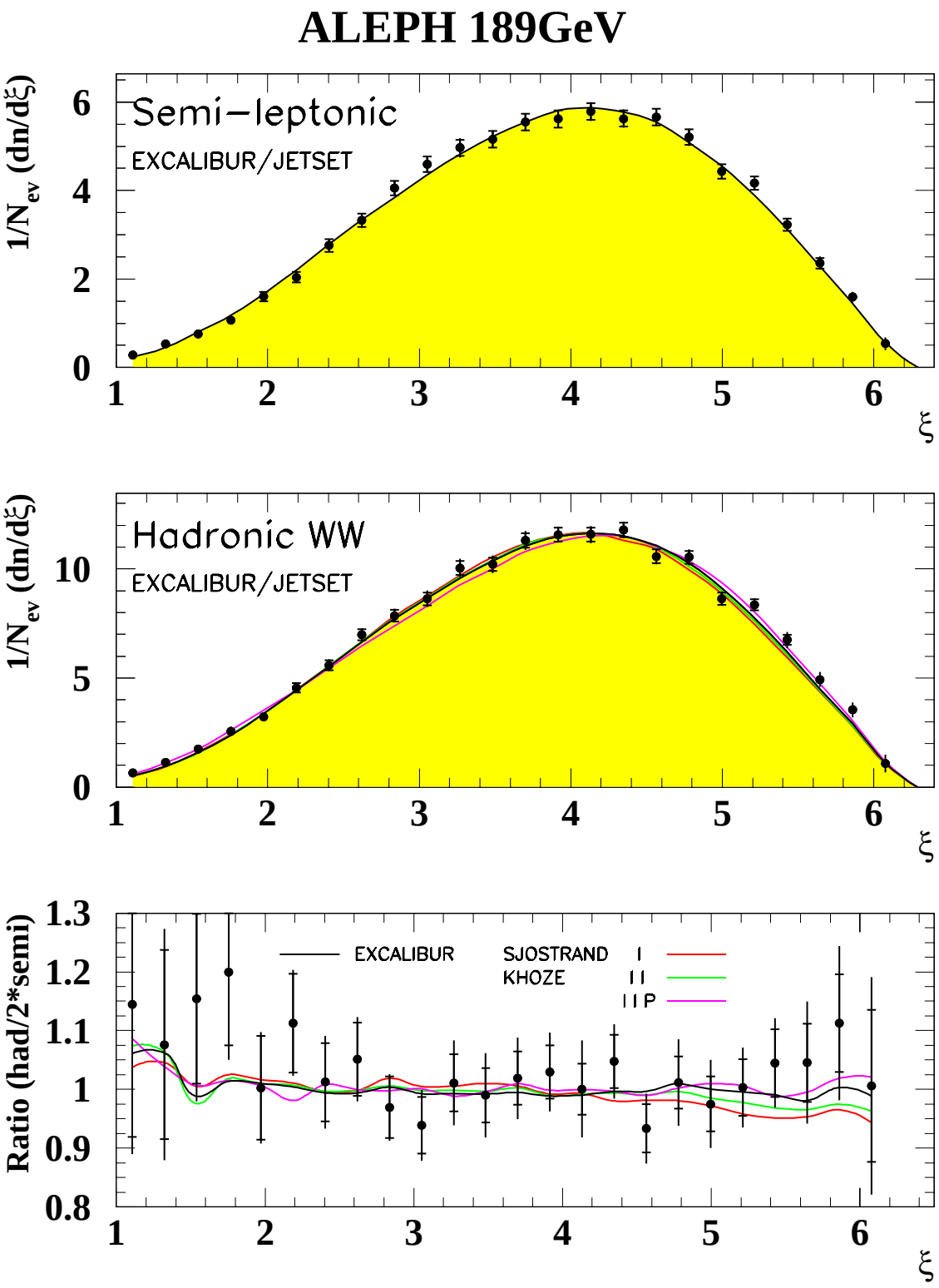

Figure 4.20: *Hadronic and semi-leptonic ξ distributions, and the ratio $\frac{\xi_{q\bar{q}q\bar{q}}}{2\xi_{l\nu q\bar{q}}}$ for 189GeV data with the EXCALIBUR/JETSET prediction with and without the three colour reconnection models by Sjöstrand and Khoze.*

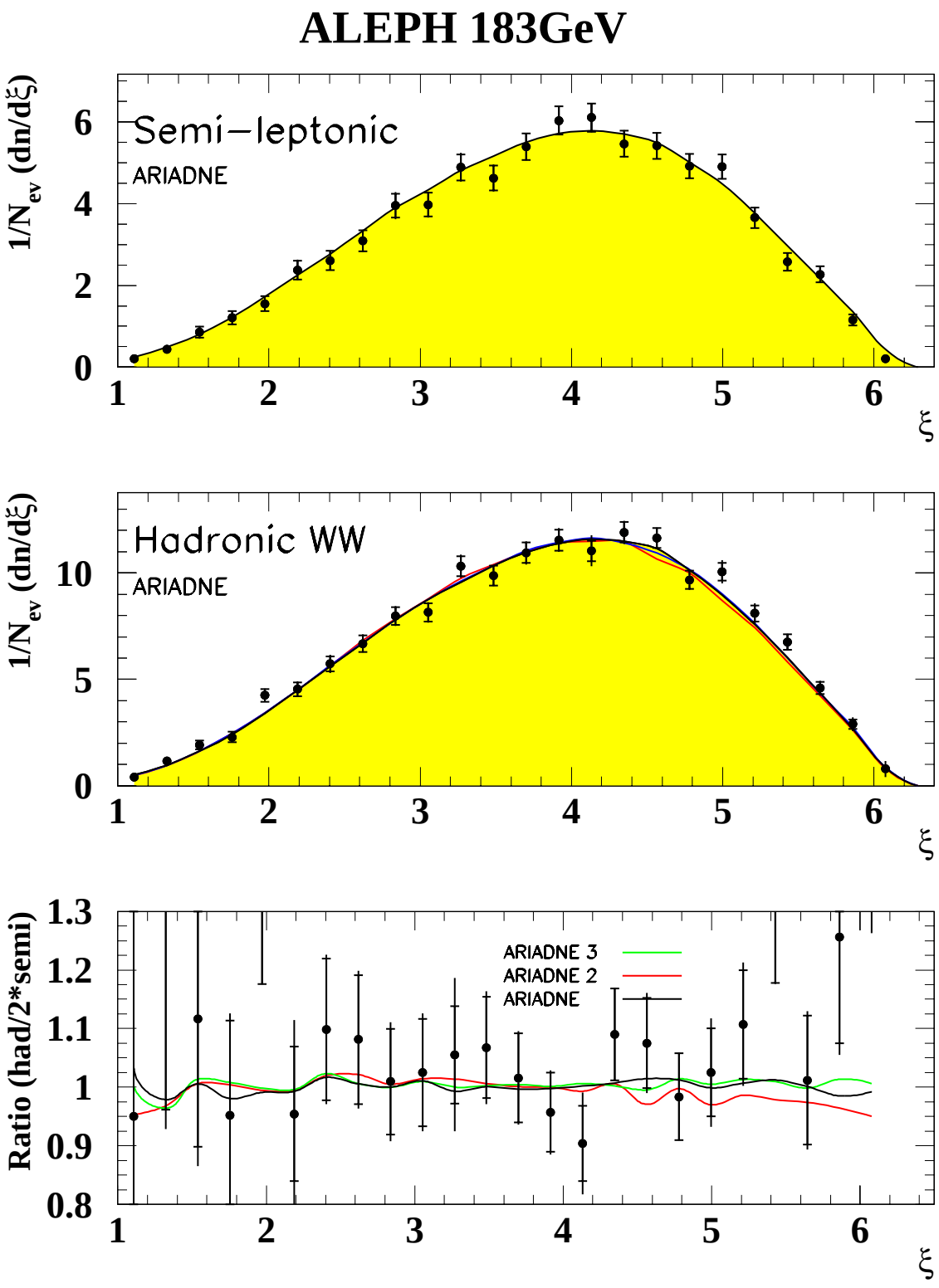

Figure 4.21: *Hadronic and semi-leptonic ξ distributions, and the ratio $\frac{\xi_{q\bar{q}q\bar{q}}}{2\xi_{l\nu q\bar{q}}}$ for 183GeV data with the ARIADNE prediction with and without colour reconnection.*

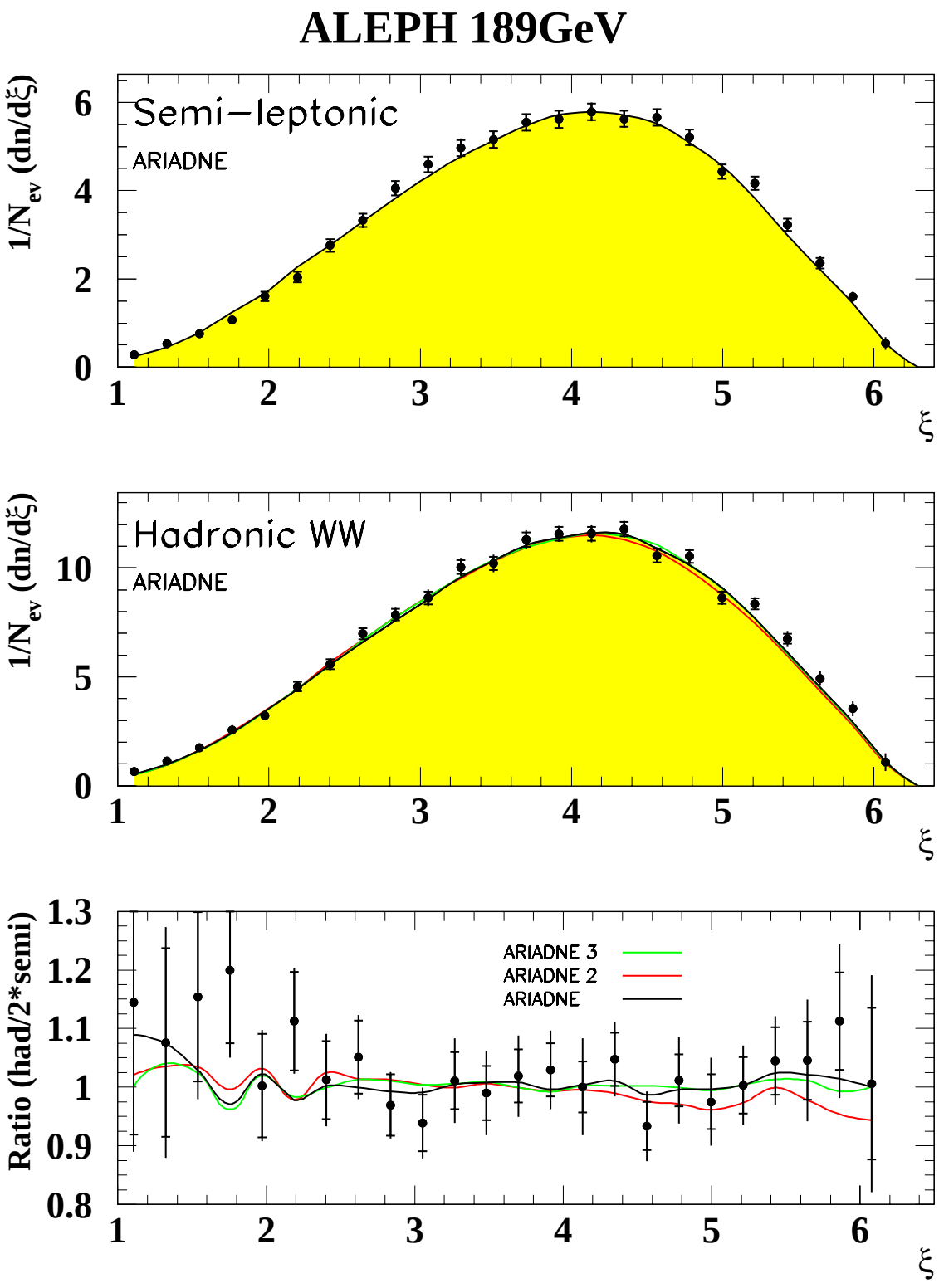

Figure 4.22: *Hadronic and semi-leptonic ξ distributions, and the ratio $\frac{\xi_{q\bar{q}q\bar{q}}}{2\xi_{l\nu q\bar{q}}}$ for 189GeV data with the ARIADNE prediction with and without colour reconnection.*

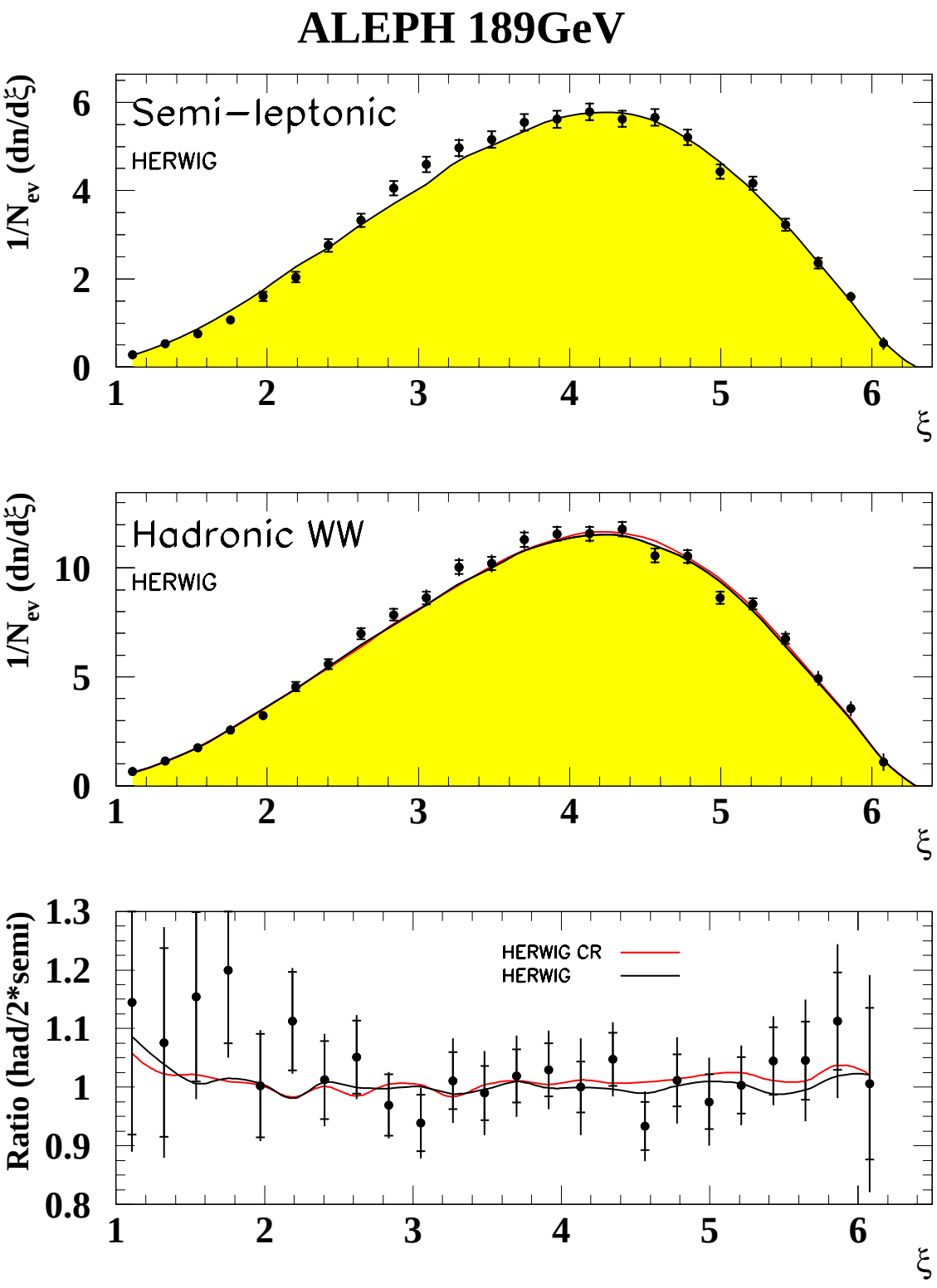

Figure 4.23: *Hadronic and semi-leptonic ξ distributions, and the ratio $\frac{\xi_{q\bar{q}q\bar{q}}}{2\xi_{l\nu q\bar{q}}}$ for 183GeV data with the HERWIG prediction with and without colour reconnection.*

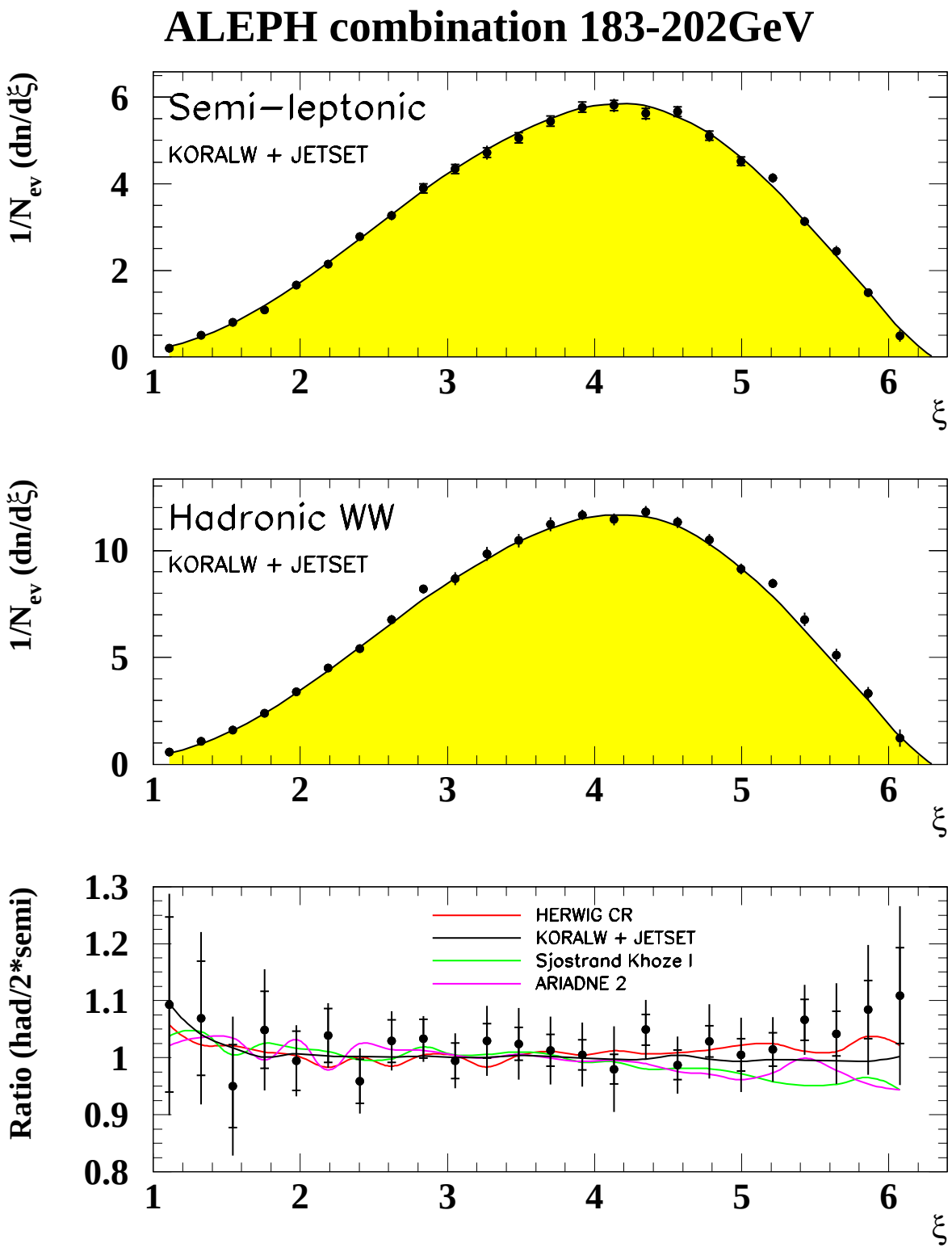

Figure 4.24: *183GeV-202GeV combined data-set with the KORALW/JETSET prediction without colour reconnection, the 189GeV colour reconnected HERWIG, ARIADNE 2 and EXCALIBUR SK I.*

4.7.2 Multiplicities

The method of calculating the mean charged particle event multiplicity is discussed in detail in Section 4.4.2 and is obtained from the integral of the momentum distributions, therefore they are subject to the same corrections to limited acceptance of the event selections and $p_t > 200$MeV, as the momenta spectra. To see if there was an effect that might be missed due to the limited acceptance 'washing out' the signal, Table 4.6 shows how the simulated effect of colour reconnection changes as the analysis is conducted at 189GeV; all numbers are still subject to the $p_t > 200$MeV cut. The generated multiplicities before and after event selections are displayed, along with the reconstructed detector level, which includes backgrounds. The size of the expected effect is represented by Δn_{cr} which is given by,

$$\Delta n_{cr} = (n_{4q} - 2 \times n_{2q})_{cr} - (n_{4q} - 2 \times n_{2q})_{nocr}. \tag{4.15}$$

It should be noted that only the HERWIG has a 'colour reconnected' semi-leptonic sample, while the others use the standard semi-leptonic simulation see Section 2.4.5. The Sjöstrand and Khoze models can be seen to have their effects reduced substantially when the Monte Carlo is run through the detector simulation; HERWIG and ARIADNE are more fortunate.

Table 4.7 shows the final multiplicities for data and the standard colour reconnection-free KORALW/JETSET Monte Carlo simulation for 183GeV and 189GeV; Table 4.8 shows the equivalent results for the combined data-set. The first error shown is statistical, the second is the systematic, and where only one error is present it is the combination of both. The data/Monte Carlo agreement (data minus MC) is shown in the right-hand column. The results are consistent with zero in both channels: being 0.62σ and 1.08σ from zero, for the hadronics and semi-leptonics, respectively at 183GeV; and 0.89σ and 0.26σ from zero, in the hadronic and semi-leptonic channels, respectively at 189GeV. The final combined channel results (Table 4.8), are seen to be 1.14σ and 0.00σ from zero, in

189GeV			
MC Sample	**Mean Charged Event Multiplicity**		
	Gen. before Selection	**Gen. after Selection**	**Detector Level**
KORALW			
$l\nu q\bar{q}$	17.33 ± 0.03	17.41 ± 0.03	16.24 ± 0.04
$q\bar{q}q\bar{q}$	34.45 ± 0.04	34.77 ± 0.04	32.08 ± 0.05
EXCALIBUR			
$l\nu q\bar{q}$	17.34 ± 0.03	17.40 ± 0.03	16.23 ± 0.03
$q\bar{q}q\bar{q}$	34.50 ± 0.03	34.69 ± 0.04	32.06 ± 0.04
$q\bar{q}q\bar{q}$ (SK I)	34.29 ± 0.03	34.49 ± 0.04	31.98 ± 0.04
Δn_{cr}	-0.21	-0.20	-0.08
$q\bar{q}q\bar{q}$ (SK II)	34.39 ± 0.03	34.58 ± 0.04	31.99 ± 0.04
Δn_{cr}	-0.11	-0.11	-0.07
$q\bar{q}q\bar{q}$ (SK II′)	34.34 ± 0.03	34.54 ± 0.04	31.97 ± 0.04
Δn_{cr}	-0.16	-0.15	-0.09
HERWIG			
$l\nu q\bar{q}$	17.25 ± 0.03	17.32 ± 0.03	16.18 ± 0.03
$q\bar{q}q\bar{q}$	34.35 ± 0.04	34.65 ± 0.04	32.01 ± 0.04
$l\nu q\bar{q}$ (CR)	17.26 ± 0.03	17.32 ± 0.03	16.15 ± 0.03
$q\bar{q}q\bar{q}$ (CR)	34.61 ± 0.04	34.90 ± 0.04	32.16 ± 0.05
Δn_{cr}	0.24	0.27	0.21
ARIADNE			
$l\nu q\bar{q}$	17.17 ± 0.04	17.24 ± 0.04	16.11 ± 0.04
$q\bar{q}q\bar{q}$	34.38 ± 0.05	34.57 ± 0.05	31.95 ± 0.05
$q\bar{q}q\bar{q}$ (A2)	34.03 ± 0.05	34.24 ± 0.05	31.74 ± 0.05
Δn_{cr}	-0.35	-0.33	-0.21
$q\bar{q}q\bar{q}$ (A3)	34.38 ± 0.05	34.57 ± 0.05	31.96 ± 0.05
Δn_{cr}	0.00	0.00	0.01

Table 4.6: *189GeV Monte Carlo multiplicities with $p_t > 200MeV$ at generated level before and after event selections, and at detector level.*

the hadronic and semi-leptonics, respectively. The hadronic data multiplicity is always seen to be higher than the Monte Carlo simulation, while the semi-leptonic is seen to agree quite nicely.

183GeV Multiplicities			
Channel	**Data**	**MC**	**data-MC**
WW $\rightarrow q\bar{q}q\bar{q}$	35.30 ± 0.38 ± 0.47	34.78± 0.04 ± 0.58	0.52 ± 0.84
WW $\rightarrow q\bar{q}l\nu$	16.87 ± 0.34 ± 0.21	17.40 ± 0.03 ± 0.29	-0.53 ± 0.49
$q\bar{q}q\bar{q} - 2 \times l\nu q\bar{q}$	1.56 ±0.78 ± 0.36	-0.02 ± 0.07	1.58 ± 0.86
189GeV Multiplicities			
WW $\rightarrow q\bar{q}q\bar{q}$	35.45 ± 0.22 ± 0.62	34.77± 0.04 ± 0.58	0.68 ± 0.88
WW $\rightarrow q\bar{q}l\nu$	17.51 ± 0.19 ± 0.16	17.41 ± 0.03 ± 0.29	0.10 ± 0.38
$q\bar{q}q\bar{q} - 2 \times l\nu q\bar{q}$	0.43 ±0.44 ± 0.47	-0.05 ± 0.07	0.48 ± 0.65

Table 4.7: *The mean charged particle multiplicities for data and Monte Carlo at 183GeV and 189GeV.*

183-202GeV combination			
Channel	**Data**	**MC**	**data-MC**
WW $\rightarrow q\bar{q}q\bar{q}$	35.75 ± 0.13 ± 0.62	34.77± 0.04 ± 0.58	0.98 ± 0.86
WW $\rightarrow q\bar{q}l\nu$	17.41 ± 0.12 ± 0.19	17.41 ± 0.03 ± 0.29	0.00 ± 0.37
$q\bar{q}q\bar{q} - 2 \times l\nu q\bar{q}$	0.93 ±0.27 ± 0.49	-0.05 ± 0.07	0.98 ± 0.56

Table 4.8: *The mean charged particle multiplicities for data and Monte Carlo for the combined data-set from 183GeV-202GeV.*

The difference between the hadronic multiplicity and twice the semi-leptonic multiplicity[21] is displayed on the bottom row of the tables. The Monte Carlo (MC) number estimates the expected bias in the difference due to the limited acceptance of the event selections, and in each case it is seen to be small and compatible with zero. However, the final result, which is the data difference minus the MC difference (bottom-right number) shows an excess occurs in the

[21]Remembering that the leptonic part of semi-leptonic events have been ignored.

hadronics at every energy and in the combination, the numbers are 1.84σ, 0.74σ and 1.75σ away from zero at 183GeV, 189GeV, and in the combination, respectively. This shows that the result of the combination is still compatible with the naive assumption of a zero value in the absence of colour reconnection, though as Table 4.6 suggests, the colour reconnection model implemented into the HERWIG Monte Carlo is favoured because it is the only model considered that predicts a positive shift of the multiplicity difference.

4.8 Summary

Hadronic and semi-leptonic WW events were selected from the ALEPH data-sets recorded from 1997 to 1999. An attempt was made to increase the efficiency of selecting 'colour reconnected' hadronic events. Charged particle momentum distributions were obtained, ignoring leptonically decaying W's, and were corrected bin-by-bin for background contamination and detector based inefficiencies. No corrections were made for the limited acceptance of the event selections or for particles with small transverse momentum. The ratio of the hadronic to twice the semi-leptonic momentum distribution was obtained and checked against various Monte Carlo simulations with and without colour reconnection. The average charged event multiplicity was obtained by integrating the fragmentation function, and twice the semi-leptonic multiplicity was subtracted from the hadronic multiplicity. The difference of the standard Monte Carlo was subtracted from the data value, and this number was found to be consistent with zero. The predicted difference in various Monte Carlo simulations were also produced. A full systematic study was conducted at 183GeV and 189GeV, and attached to the final distributions and multiplicities.

No evidence is seen for colour reconnection at the present level of statistics available, in either charged particle momenta or multiplicities. All the models which have been tested with and without implimentations of colour reconnection

are seen to be reasonably compatible with the data. However, there is a hint that the data is more like the HERWIG simulations and that the models of Sjöstrand and Khoze are bordering on being rejected.

Chapter 5

Lorentz Invariant Colour Reconnection Investigation

5.1 Introduction

5.1.1 Motivation

Long before LEP2 started recording W pair decays, there had been many predictions [15, 16] that colour reconnection would have small effects on observable quantities such as the W mass, multiplicity, and momentum distribution. Some early theoretical studies by Geiger and Ellis [39], and Sjöstrand and Khoze [25] suggested that colour reconnection was dependent on event topology, implying that the effects were enhanced when regions of parton evolution originating from separate W decays, overlapped. If particles lying in the regions of overlap could be identified, then the colour reconnection signal could be greatly enhanced. To achieve this however, it would have to be possible to somehow measure how 'close' a particle is to both W's. At this stage, it should be noted that the Geiger and Ellis approach to defining this region of overlap was in terms of angles between jets calculated in the lab frame, however, this is clearly not Lorentz invariant, and the physics occurring in the true overlap region must be entirely independent of

the reference frame. So, it is not immediately obvious how best to define this 'closeness', and the task of doing so is not going to be a trivial one.

Traditionally [77], there are three main particle distributions used to describe hadronic events (which are generally back-to-back 2-jet events, *i.e.* $e^+e^- \rightarrow Z^0/\gamma \rightarrow q\bar{q}$):

1. The scaled momentum distribution, x_p, more usually plotted as ξ, these are defined by equations 4.2 and 4.3, on page 83;

2. The rapidity, y, which is defined as

$$\text{rapidity} = -\frac{1}{2}\ln\left[\frac{E - P_\parallel}{E + P_\parallel}\right], \tag{5.1}$$

   relative to an event axis such as the thrust axis, explained in Appendix A.1;

3. The momentum of tracks transverse to the thrust axis of the event, p_t.

The rapidity and the transverse momentum are by definition Lorentz invariant for boosts along the line-of-flight of the original $q\bar{q}$ axis of a 2-jet event, while the scaled momentum is the distribution of particles in the lab frame. We are on the right lines with invariant particle distributions to aid us in developing a method to obtain a particle's 'closeness' to one or both W's, and hopefully they will be able to help us define exactly what 'closeness' means. However, for the case of the WW events there is a problem, as neither of the two $q\bar{q}$ pairs are back-to-back[1] due to the boost of the W boson from which they originate. This makes the thrust axis used for the 2-jet QCD events now appear rather meaningless in the case of a 4-jet WW event, as it is not clearly related to the decay axis of either W. Thus, we are forced to raise the question: how is it possible to define a meaningful axis for calculation of the transverse momentum and rapidity for tracks originating from W pairs? Clearly the scaled momentum distribution will

[1] In fact they can be back-to-back, but only for the rare case when the line-of-flight of the $q\bar{q}$ pair is along the W trajectory.

also be influenced by the boost of the W, so it is interesting to obtain the spectra of momenta as if they were produced from a stationary source.

5.1.2 Definition of Variables

Members of Lund University suggested a solution to a member of the ALEPH collaboration [78], which was to consider versions of the three particle distributions, but calculated from Lorentz invariant dot products of 4-vectors. This would remove the effect of the W boost allowing distributions of particles in either W rest frame to be produced. These variables will be referred to as the Lorentz invariant variables (LI) and are defined below.

If p_i is the 4-momentum of a particle, and q_1 and q_2 are the 4-momenta of the primary quarks from a W decay (assumed to be massless), then Lorentz invariant versions of the scaled momentum, x_w, rapidity, y, and transverse momentum, p_t, are:

$$x_w = \frac{1}{2}\frac{(q_1 + q_2)\cdot p_i}{q_1 \cdot q_2} \tag{5.2}$$

$$y = -\frac{1}{2}\ln\left[\frac{p_i \cdot q_1}{q_1 \cdot q_2}\right] \tag{5.3}$$

$$p_t^2 = \frac{2(p_i \cdot q_1)(p_i \cdot q_2)}{q_1 \cdot q_2}. \tag{5.4}$$

Notice now that the scaled momentum is expressed as x_w, instead of the normal x_p, this is to signify that it is the spectra of momenta from a decaying W boson rather than a general momentum distribution.

We now have the tools needed to be able to explain what the statement, 'close to both W decays' means, and can now suggest how it could produce a variable more sensitive to the effects of colour reconnection. Consider a particle in the rest frame of its parent W, where there are two back-to-back jets from the W decay. The particle can be thought of as being close to the W if it is produced with a small transverse momentum relative to the original quark direction. This will be referred to as the particle being in its 'correct' or 'parent' W rest frame.

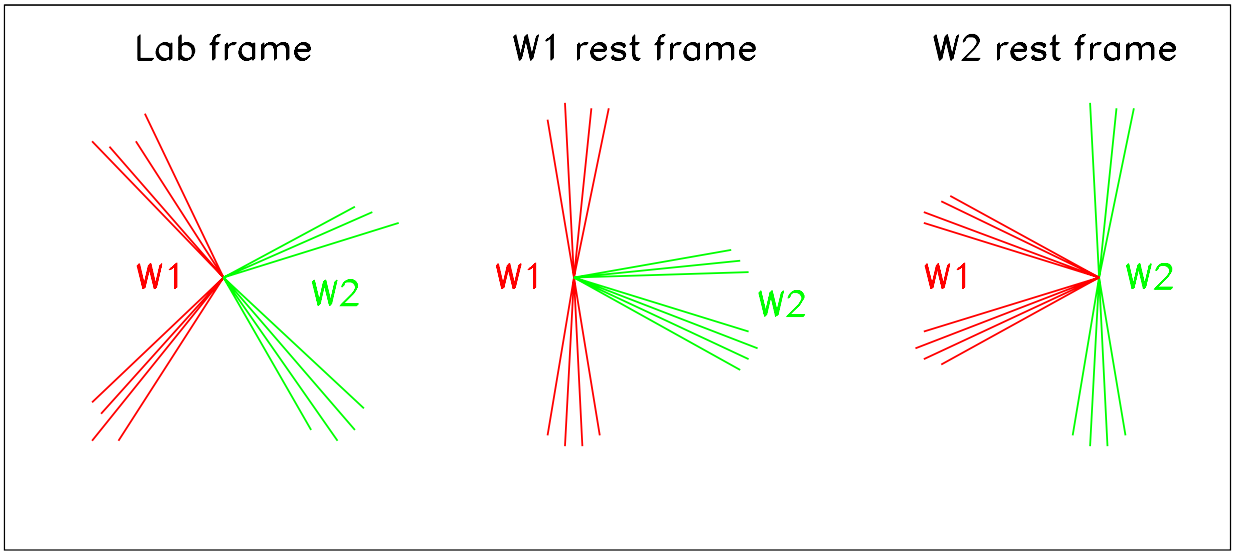

Figure 5.1: *Schematic representations of a hadronic 4-jet event placed into the lab and each W rest frame, showing how the tracks move around with the boost of the W particle. The W1 dijet is red and the W2 dijet is green.*

By 'correct', what is meant is that the algorithm (described in the next section) has placed the particle into a jet, and assigned that jet to have arisen from the decay of a particular W, *i.e.* the particle belongs to a dijet.

Now consider the same particle but in the rest frame of the other W from which it did not originate, this will be referred to as the 'incorrect' or 'non-parent' rest frame, though by the same argument as above, this is by no means actually true. It is possible to find the transverse momentum of the particle relative to the quark axis of this 'incorrect' W decay. If the p_t is small in this rest frame as well, then the particle is close to both W's, and will, it is believed, be more likely to be affected by colour reconnection. A similar procedure for the scaled momentum, x_w, considering how soft the particle is to each W, will produce the same conclusion about 'closeness'. However, the case for rapidity, y, is not quite as clear. The Monte Carlo models could be used to help suggest which regions of rapidity are affected, which is also true for x_w and p_t too.

Figure 5.1 illustrates that a distribution of particles in their 'correct' rest frame

will be made from the red particles in the 'W1' rest frame and the green ones in the 'W2' rest frame, therefore including all the particles of an event. Similarly, the 'incorrect' rest frame distributions will contain the green particles in the 'W1' rest frame and the red ones in the 'W2' rest frame.

A further suggestion [78] is to obtain a combination variable, manufactured from the values of a particle in the two rest frames, and to consider the particles which are felt to be in a region of closeness in both rest frames. Plots could then be made for the other LI variables, thus hopefully obtaining a distribution of particles more susceptible to the effects of colour reconnection and also then being able to predict a visible signal using the models available.

5.2 Experimental Procedure

Now the definition of the variables are understood, and the aims in using them are clear, consideration must be made about how to calculate the distributions from the experimental data. In the definition of the variables, knowledge of the directions of the massless primary quarks is necessary, therefore a method will have to be found to reconstruct these 4-vectors. It will also be important to be able to identify the particles which originate from each W boson so that we can place them in either the parent rest frame or the non-parent rest frame, though it may be that with a combination variable, this may not actually be a problem. Both of these factors are incorporated into the algorithm which is used to calculate the variables, and starts by selecting hadronic events using the neural network described in Section 4.2.1.

Part of the neural network selection forces the events into a 4-jet configuration and the tracks used to manufacture each jet are then recorded. Now, clearly two jets belong to one W, and two to the other; by pairing them up correctly, we will know which particles belong to which parent W. This is an issue that was first investigated by the hadronic W mass group, and it is their algorithm [79] which

will be utilised and discussed in Section 5.2.2.

The knowledge of the primary quark directions comes from a calculation of the thrust axis[2] from the two back-to-back jets in the rest frame of the W from which they arose, while ignoring the other half of the event. The massless quark axis is taken to be the thrust direction. Before this is possible, we have to boost the particles in the jets into the rest frame of the W, by reconstructing the W 4-vector from the lab jet-vectors it decayed into. However, by first subjecting the four jet-vectors to a kinematic fit [57, 80, 81], this will provide a better estimate of the real directions, and therefore the W trajectory, because of the constraints to energy and momentum conservation in the entire event. Kinematic fitting is a subject extensively studied by the W mass group and will be subsequently discussed quite briefly.

5.2.1 Kinematic Fitting

In any recorded event, the total energy and momentum of all the visible objects inside the detector will be smaller than the centre-of-mass energy of the e^+e^- collision that produced them. Naturally, the centre-of-mass energy would be expected to be reproduced by momentum and energy conservation if the detector was perfect. But, the detector is not perfect, it cannot record particles which occur in particular regions, nor does it always reconstruct the momentum of tracks correctly for example, (see Chapter 3). There will also be undetectable particles, such as neutrinos from particle decays within the detector which will remove energy.

This missing energy and momentum will have an effect on the direction of the jet-vectors produced by the jet-finding algorithm. The W mass analysis group was interested in the resolution on the W mass, so they developed a kinematic fitting package [80] to correct the jet-vectors. This was done by constraining

[2]See Appendix A.1 for a definition of the thrust axis.

the event to energy and momentum conservation and adjusting the jet-vectors accordingly. For a full review of the kinematic fitting techniques used by the ALEPH hadronic W mass group, see References [57] and [81].

If $\vec{P}_i$ is the measured jet-vector of jet i and $\vec{P}_i^{cor}$, the corrected one after the kinematic fit, then a_i, b_i, and c_i are the coefficients which transform them via,

$$\vec{P}_i^{cor} = a_i \vec{P}_i + b_i \vec{u}_i^{\theta} + c_i \vec{u}_i^{\phi}, \tag{5.5}$$

where, $\vec{u}_i^{\theta}$ is perpendicular to $\vec{P}_i$ and lies in the plane between $\vec{P}_i$ and the z axis, $\vec{u}_i^{\phi}$ is perpendicular to both $\vec{P}_i$ and $\vec{u}_i^{\theta}$. Thus, this relates b_i and c_i to angular corrections, and a_i to an energy correction. These three coefficients are predetermined using Monte Carlo and allow the fit to vary the measured parameters around their mean, but within their Gaussian width.

5.2.2 Jet-Pairing

In the W mass analysis the kinematically fitted jets are paired up to produce two dijets, so that the invariant mass of the W bosons can be obtained. In this study however, we are interested in the direction and magnitude of the W boost. Hence, the jets are paired according to the usual W mass scheme [57, 79], which is to find the pairing with the smallest mass difference between the two dijets. An additional constraint is included, which is the chosen pairing must not be the one with the smallest opening angle of either of the dijets [82] because this is unlikely to occur[3]. If this is found to be the case then the second smallest mass difference is used. The pairing routine has been estimated to obtain the correct pairing over 75% of the time [57].

[3]For example see Figure 4.3 in Section 4.2.2.

5.3 Individual Lorentz Invariant Distributions

5.3.1 Scaled Momentum, x_w

The LI scaled momentum, x_w (equation 5.2) is plotted as ξ_w where,

$$\xi_w = -\ln(x_w), \tag{5.6}$$

and the distributions for both W rest frames are displayed in Figure 5.2. The plots are for 189GeV data, and for fully reconstructed detector level Monte Carlo plus background simulation. The WW signal is produced by the EXCALIBUR/JETSET Monte Carlo without colour reconnection, and the backgrounds are generated by PYTHIA/JETSET. The events are selected using the hadronic neural network selection as described in Section 4.2.1, with the same criteria of $outnn > -0.9$, and jet containment of $\cos\theta_{jet} < 0.9$. The distributions have been normalised to a differential cross-section, as explained on page 87, and the error bars show only statistical uncertainties.

The top plot, marked a), shows the distribution of all tracks in selected WW events when they are in the rest frame of their parent W particle[4]. This can be interpreted as the spectra of momenta produced from W boson decays, if it were possible to produce the particle individually. The lower plot, marked b), shows the momentum distribution for exactly the same tracks as the former but they are always in the rest frame of the 'incorrect' W parent (or dijet). It is seen to be shifted to the left and can therefore be thought of as a harder distribution, which would be expected because the particles now include momentum from the boost of the W whose rest frame they are now in.

It is now interesting to discover how a particle's momentum varies from the 'correct' to the 'incorrect' W rest frame, which can be found by examining the two-dimensional scatter plot shown in Figure 5.3. Events are again selected by

[4]Remember that this description means that the particle is in the rest frame of the dijet to which it belongs.

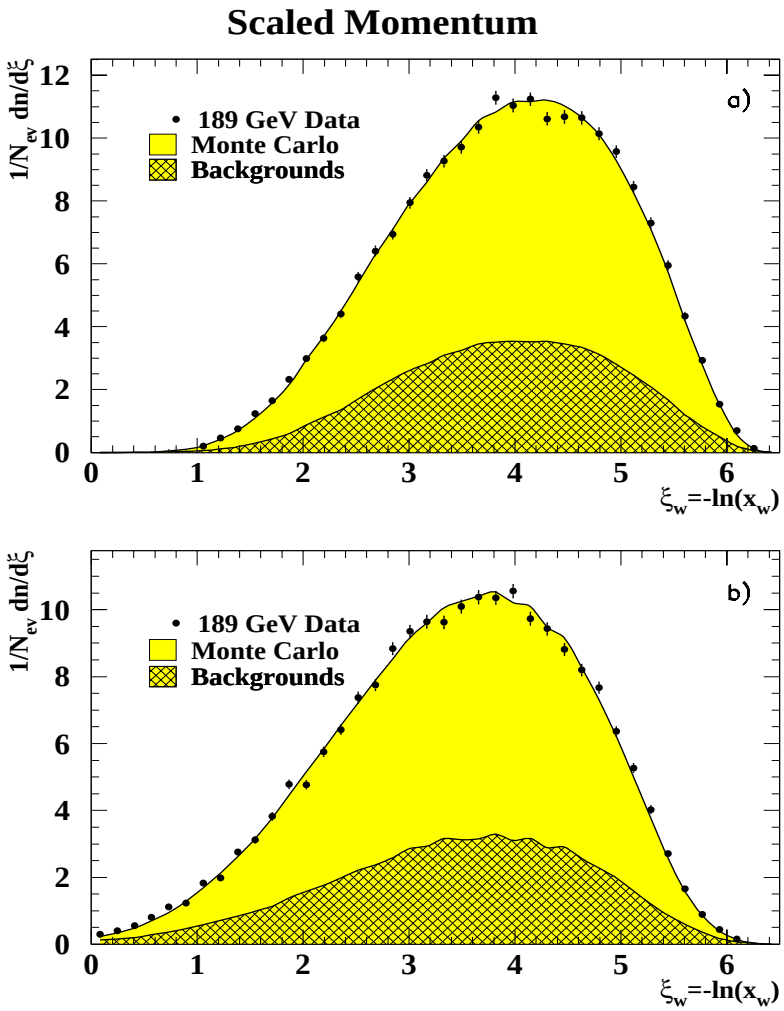

Figure 5.2: *LI scaled momentum distributions for fully reconstructed MC and 189GeV data. a) all tracks are in the rest frame of their parent W. b) all tracks are in the rest frame of the other (non-parent) W particle in the event.*

the hadronic neural network and jet containment. The abscissa is the ξ_w produced when the reconstructed track is in the rest frame of its parent W against the ξ_w of the track in the rest frame of the other W on the ordinate. The left plot is produced from the EXCALIBUR/JETSET WW signal Monte Carlo, while the right plot shows the prediction of the PYTHIA/JETSET QCD background. The particles can clearly be seen as being reasonably correlated between the two rest frames, but a track is generally softer when it is in the 'correct' W rest frame. The background distribution shows similar effects but obviously due to the selected events looking like W pairs, with the algorithm finding a 'correct', and 'incorrect'

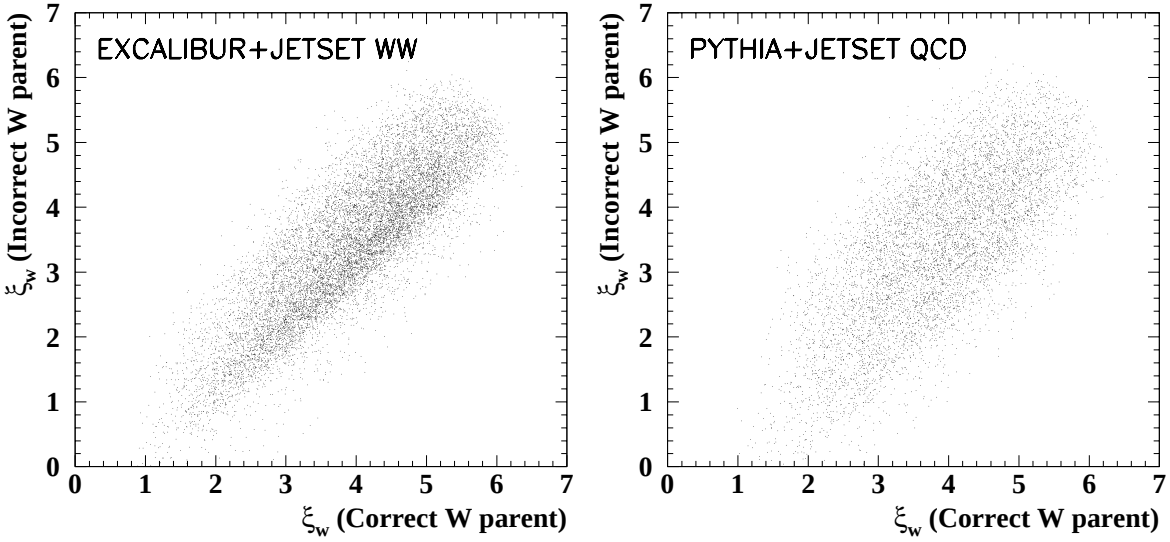

Figure 5.3: *LI scaled momentum scatter distributions, using reconstructed particles from selected signal (left), and background events (right).*

W parent, while there is clearly no such thing in the event. The background distribution without the event selection would show a much weaker correlation. These correlation plots will be required later on when an attempt is made to define a track which is close to both W decay axes.

5.3.2 Transverse Momentum, p_t^2

The LI transverse momentum squared, p_t^2 (equation 5.4) is plotted logarithmically as $-\ln\left(\frac{2p_t^2}{E_{cm}}\right)$, so that the distribution at low transverse momenta is stretched out. This enables the region of interest to be seen, which is namely the fall on the right of the plot which would be clumped together without the logarithmic scale. The distributions for both W rest frames are displayed in Figure 5.4.

The plots shown are for 189GeV data and for fully reconstructed detector level Monte Carlo plus background simulation. The WW signal is produced by the EXCALIBUR/JETSET Monte Carlo without colour reconnection, and the backgrounds are generated by PYTHIA/JETSET. The events are selected using the hadronic neural network selection, as described in Section 4.2.1, using the same criteria of $outnn > -0.9$ and jet containment of $\cos\theta_{jet} < 0.9$. The

distributions have been normalised to a differential cross-section, as explained on page 87 and the error bars show only statistical uncertainties.

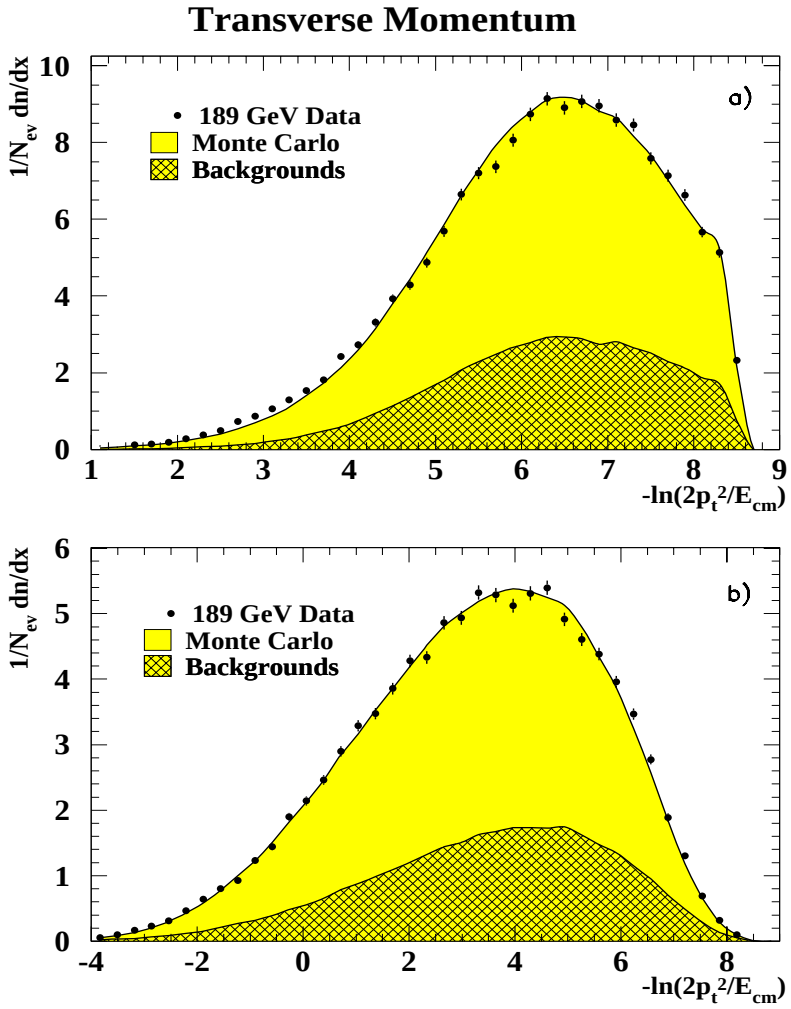

Figure 5.4: *LI transverse momentum distributions for fully reconstructed MC and 189GeV data. a) all tracks are in the rest frame of their parent W. b) all tracks are in the rest frame of the other (non-parent) W particle in the event.*

The top plot, marked a), shows the transverse momentum distribution for all tracks in selected WW events when they are in the rest frame of their parent W particle. The majority of particles lie as expected, in the soft region[5] to the right of the plot because the tracks are produced in two back-to-back jets, collinear to the primary quark axis. The sudden cut-off of the distribution at about 8.5 is due to the particles having zero (or nearly zero) calculated transverse momentum

[5]The peak of distribution a) occurs at a value of ≈ 6, which is equivalent to a transverse momentum of only 600MeV.

in this rest frame, thus leaving only the mass of the particle to contribute to the p_t^2 [83]. All charged tracks reproduced by the ALEPH reconstruction software are assumed to be charged pions with a mass of 139.57MeV [13], which produces $-\ln\left(\frac{2p_t^2}{E_{cm}}\right) = 8.48$. At this point it must be realised that perhaps the name 'transverse momentum', is a little misleading because the variable is actually some form of transverse 4-momentum and not 3-momentum, hence the entering of the particle mass[6]. A more correct description would be the 'transverse mass', though the notation and naming convention introduced earlier in this chapter will be retained, and this point will be marked as an interesting feature.

The lower plot, marked b), shows the transverse momentum distribution for exactly the same tracks as the top one but they are always in the rest frame of the 'incorrect' W parent. The particles will no longer be produced collinear to the primary quark axis of this W decay, and will tend to be emitted with a definite angle to it. It is therefore expected to see a harder distribution, which is exactly what is observed[7].

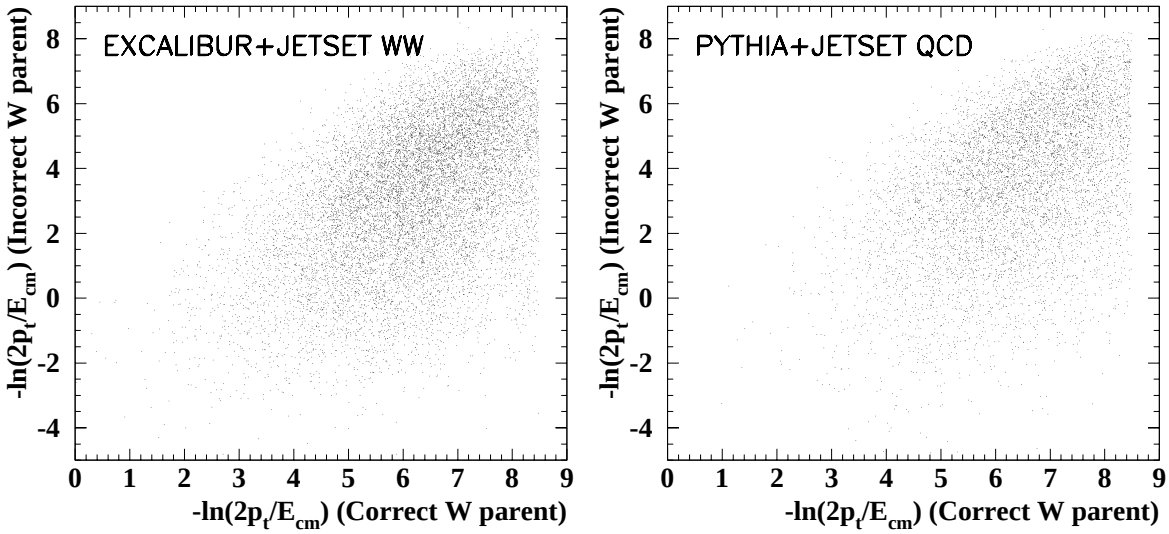

Figure 5.5: *LI transverse momentum scatter distributions, using reconstructed particles from selected signal (left) and background events (right).*

[6]Our p_t^2 is actually $p_t^2 = E^2 - |p|^2\cos\theta$, which in the limit of $m \to 0$, becomes $p_t^2 = |p|^2\sin\theta$.

[7]The peak of distribution b) occurs at a value of ≈ 4, which is equivalent to a transverse momentum of 1.3GeV.

The two-dimensional scatter plots displayed in Figure 5.5 show how the distributions of the transverse momentum varies from one rest frame to the other. Events are selected by the hadronic neural network and jet containment. The plot shows $-\ln\left(\frac{2p_t^2}{E_{cm}}\right)$ produced by the reconstructed track in the parent W rest frame on the abscissa against $-\ln\left(\frac{2p_t^2}{E_{cm}}\right)$ produced in the 'incorrect' W rest frame on the ordinate. The left plot is produced from the EXCALIBUR/JETSET WW signal Monte Carlo and the right shows the prediction of the PYTHIA/JETSET QCD background. There is no strong correlation between the two distributions as seen earlier with the scaled momentum, thus suggesting that it may be more difficult to obtain particles that are close (possess low transverse momentum) to both W's. It should be noted there are very few tracks which are softer in the 'incorrect' rest frame than in the 'correct' one, and this can quickly be observed because the majority of tracks lie below the line $y = x$. This further emphasises the point raised earlier about the tracks being collinear to the quark axis in the 'correct' W rest frame, but not in the 'incorrect' one. The background distribution is seen to be very similar to the signal.

5.3.3 Rapidity, y

The distributions of the LI rapidity, y (equation 5.3) are plotted for both W rest frames and are displayed in Figure 5.6. The plots are for 189GeV data and for fully reconstructed detector level Monte Carlo plus background simulation. The WW signal is produced by the EXCALIBUR/JETSET Monte Carlo without colour reconnection, and the backgrounds are generated by PYTHIA/JETSET. The events are selected using the hadronic neural network selection as described in Section 4.2.1, using the same criteria of $outnn > -0.9$ and jet containment of $\cos\theta_{jet} < 0.9$. The distributions have been normalised to a differential cross-section, as explained on page 87 and the error bars show statistical uncertainties only.

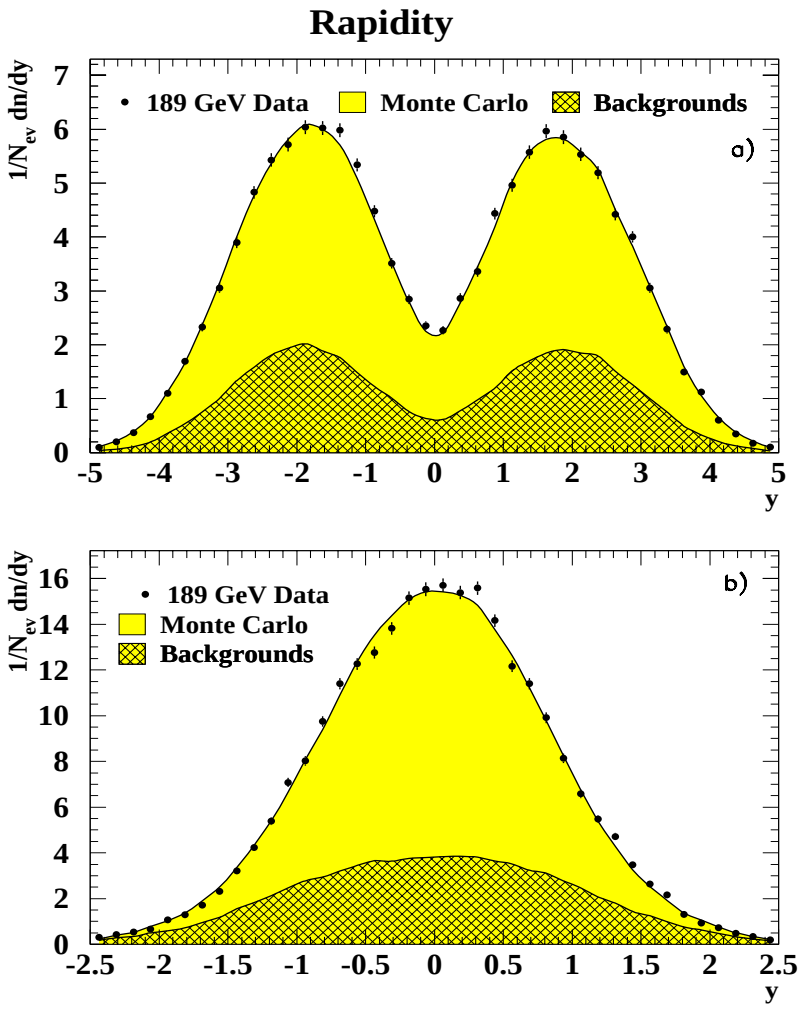

Figure 5.6: *LI rapidity distributions for fully reconstructed MC and 189GeV data. a) all tracks are in the rest frame of their parent W. b) all tracks are in the rest frame of the other (non-parent) W particle in the event.*

The distribution at the top of Figure 5.6, marked a) shows the rapidity of all tracks in selected WW events in the rest frame of their parent W particle. Its distinctive double peak is typical for a rapidity distribution from a back-to-back 2-jet structure. The positive peak is formed from the tracks lying in the core of the jet parallel to the thrust axis, while the negative peak is formed from the jet anti-parallel to it. The trough at zero rapidity arises because there are only a few particles which are emitted perpendicularly to the rapidity axis, or with low momentum in this frame. The lower plot marked b) in Figure 5.6, shows the rapidity distribution for exactly the same tracks as plot a), but in the rest frame

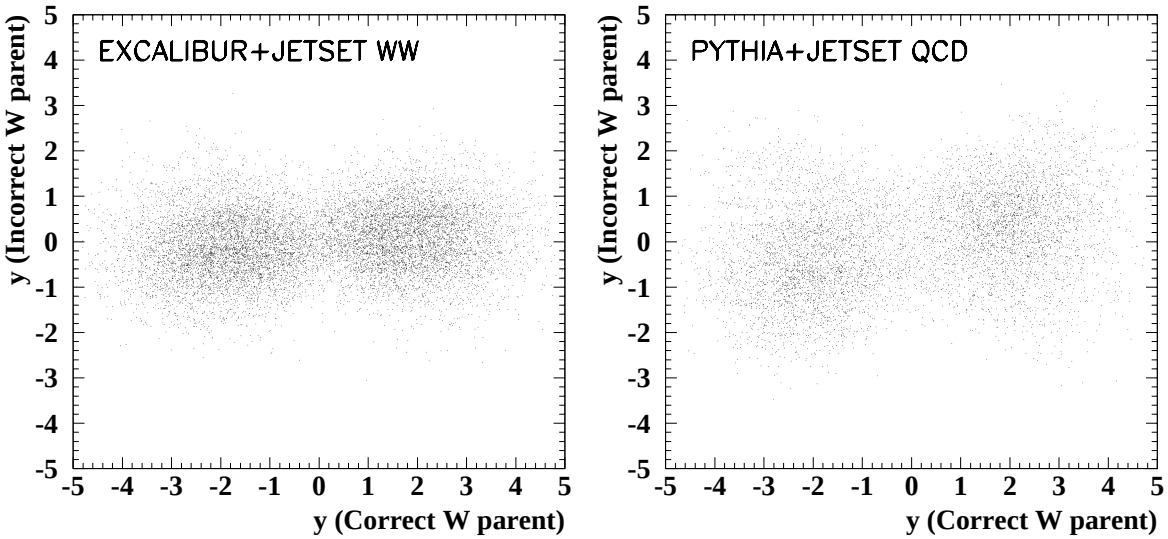

Figure 5.7: *LI rapidity scatter distributions, using reconstructed particles from selected signal (left) and background events (right).*

of the 'incorrect' W parent. It is clearly a very different distribution and suggests that the majority of tracks are now produced non-parallel to the primary quark axis of the non-parent W.

The two-dimensional scatter plots of the rapidity in the two rest frames are shown in Figure 5.7 for reconstructed tracks selected by the hadronic neural network and jet containment. The abscissa is the rapidity produced when the reconstructed track is in the rest frame of its parent W, against the rapidity of the track in the rest frame of the other W on the ordinate. The left plot is produced from the EXCALIBUR/JETSET WW signal Monte Carlo, and the right plot shows the prediction of the PYTHIA/JETSET QCD background.

The particles can clearly be seen as being relatively uncorrelated, from one rest frame to the other. This suggests it could be difficult to distinguish particles which are close to both W particles in rapidity space. The background distribution is a little more diffuse than the signal, because it possesses a flatter shape in the 'incorrect' W rest frame than the signal does, see plot b) in Figure 5.6.

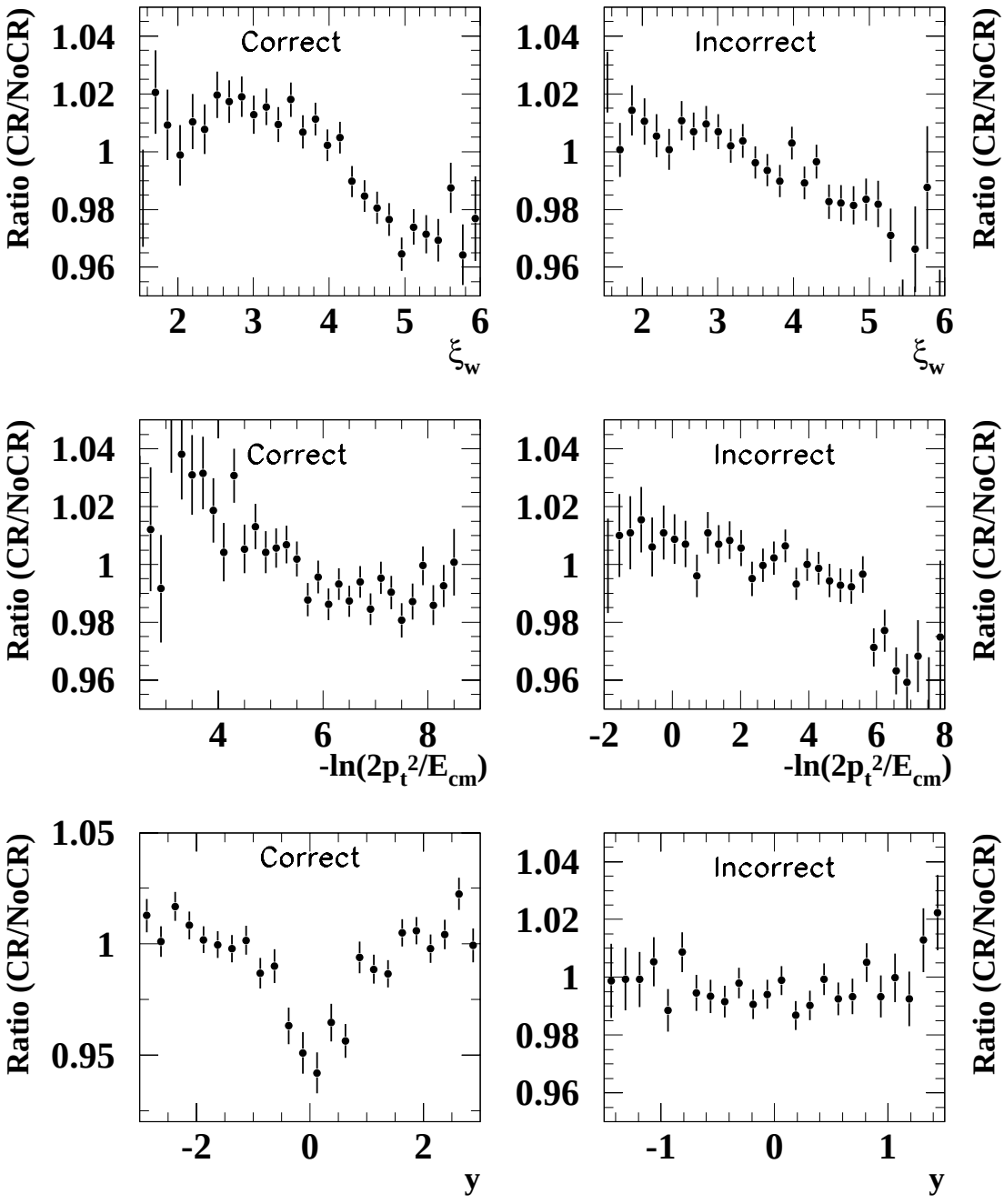

Figure 5.8: *Regions of the six LI variable distributions affected by colour reconnection. The plots are the ratio of the variable as predicted by EXCALIBUR/JETSET without colour reconnection, to the variable as predicted by the colour reconnected version of EXCALIBUR/JETSET, SK I, at the detector level for every generated hadronic event. The error bars are statistical.*

5.3.4 Effect of Colour Reconnection

At this point it is interesting to investigate the effect of colour reconnection on the single LI variables because it will hopefully suggest which regions of the distributions are affected as an aid in developing combination variables. However, it must be noticed that each distribution has the same event multiplicity (area under the plot) as the ξ distributions displayed in Chapter 4, therefore the size of the effect in any one plot will be no larger than it was earlier, *i.e.* small.

The effects of colour reconnection on the single LI variable distributions are in fact so small, that including a reconnected model on the plots already displayed in this section will not produce a striking result. Therefore, the chosen method is to display the ratio of the EXCALIBUR/JETSET detector level prediction without colour reconnection, to the Sjöstrand Khoze Model I prediction, which is implemented into EXCALIBUR/JETSET. The plots are made using every generated hadronic event in the samples. The results are displayed in Figure 5.8 and show that for both ξ_w and $-\ln\left(\frac{2p_t^2}{E_{cm}}\right)$, the deficit of particles occurs in the soft region (right of distributions) with a slight excess in the harder region (left). The rapidity shows a deficit in the dip region of the 'correct' rest frame distribution, while in the 'incorrect' rest frame, no affected region is identifiable.

5.4 Combination Variables

The introduction to this chapter has already explained the interest of combining the LI variables from the previous section to form new, and hopefully sensitive variables. The aim is to be able to identify particles which are close, in relation to both W decays. This means that a particle lies in the region most likely to be affected by colour reconnection (the deficit in Figure 5.8) in both the 'correct' and the 'incorrect' W rest frames. Therefore, in the case of ξ_w and $-\ln(2p_t^2/E_{cm})$, a

variable is sought[8] that will be large when the value is large in both rest frames, and small when the value is small in both rest frames. The possibilities are to either add or multiply the value of the variable in both rest frames together. Notice also that this can be done first inside, or outside of the logarithm, therefore the four possible combination variables for ξ_w ($XWCOM$) are:

$$XWCOM1 = -\ln[x_{ws}] \times -\ln[x_{wo}], \tag{5.7}$$

$$XWCOM2 = -\ln[x_{ws} + x_{wo}], \tag{5.8}$$

$$XWCOM3 = -\ln[x_{ws}] - \ln[x_{wo}], \tag{5.9}$$

$$XWCOM4 = -\ln[x_{ws} \times x_{wo}], \tag{5.10}$$

where x_{ws} and x_{wo} are the LI scaled momentum values (equation 5.2) in the 'correct' (same) W rest frame, s, and the 'incorrect' (other) W rest frame, o, respectively. Notice that variables 5.9 and 5.10 are clearly identical. The distributions of the first three of these are displayed in Figure 5.9.

The four possible combination variables for p_t^2 ($PT2COM$) are:

$$PT2COM1 = -\ln[p_{ts}^2] \times -\ln[p_{to}^2], \tag{5.11}$$

$$PT2COM2 = -\ln[p_{ts}^2 + p_{to}^2], \tag{5.12}$$

$$PT2COM3 = -\ln[p_{ts}^2] - \ln[p_{to}^2], \tag{5.13}$$

$$PT2COM4 = -\ln[p_{ts}^2 \times p_{to}^2], \tag{5.14}$$

where p_{ts}^2 and p_{to}^2 are the LI transverse momentum squared (equation 5.4) values in the 'correct' (same) W rest frame, s, and the 'incorrect' (other) W rest frame, o, respectively. Notice also that variables 5.13 and 5.14 are clearly identical. The distributions of the first three of these are displayed in Figure 5.10.

The scaled momentum combination variable chosen is the first one, given by equation 5.7, this is because it is observed to fall slower at large values than the

[8]No combination variable will be attempted for the rapidity due to the lack of a signal region in the 'incorrect' W rest frame.

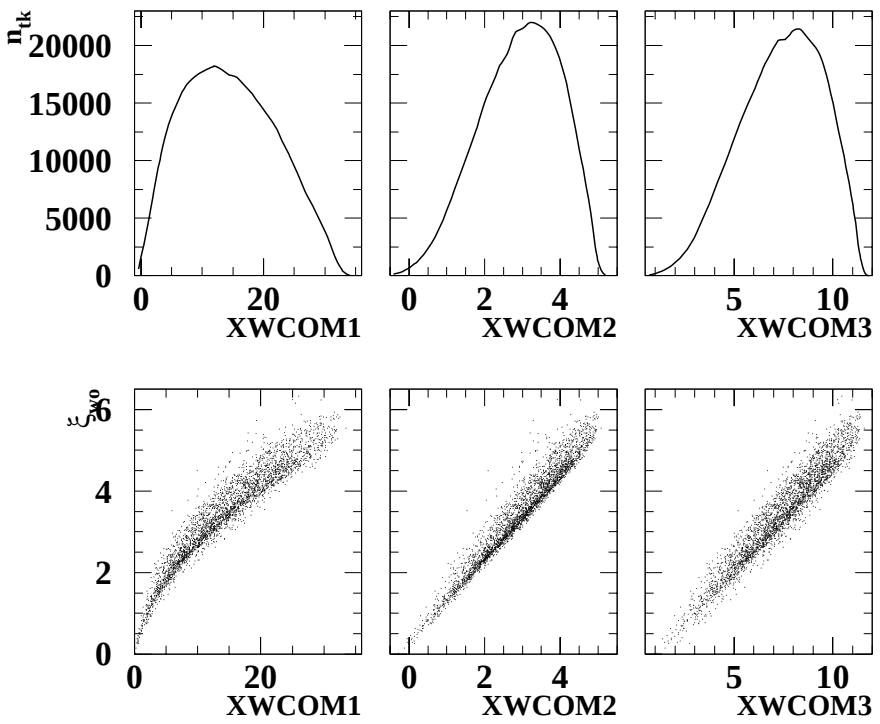

Figure 5.9: *Plots of the three possible ξ_w combination variables, XWCOM (top), and the 2D scatter (bottom) of the combination against ξ_{wo} (ξ_{ws} similar). The plots are made using all hadronic events in the EXCALIBUR/JETSET sample without CR.*

other two possible choices, thus, spreading out the interesting region of the colour reconnection deficit more, as required. The greater spread can also be easily seen in the lower scatter plots, with the region of interest lying in $\xi_{wo} > 4$, which covers a larger range in the first *XWCOM*. There is little to distinguish between $XWCOM2$ and *XWCOM3*.

To choose the best *PT2COM* distribution, two are rejected almost instantly, while the remaining one is selected. *PT2COM1* (equation 5.11) is rejected as it is seen to cluster around zero, this results in no selection power. This occurs because both of the component distributions (Figure 5.4) cross zero and the multiplication of the two often results in near zero values. *PT2COM2* (equation 5.12) is rejected because the lower plot shows it is highly correlated with the LI transverse momentum distribution in the 'incorrect' W rest frame, and therefore

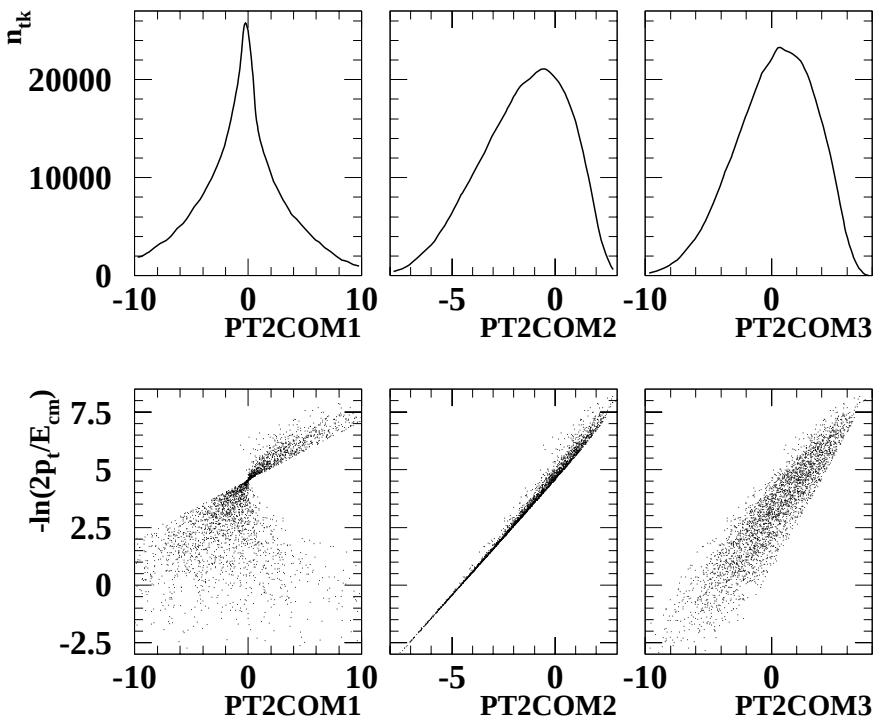

Figure 5.10: *Plots of the three possible p_t^2 combination variables, PT2COM (top), and the 2D scatter of the combination against $-\ln\left(\frac{2p_t^2}{E_{cm}}\right)_o$ (bottom). The plots are made using all hadronic events in the EXCALIBUR/JETSET sample without CR.*

is not really a combination at all. The third combination variable is chosen, though it should be noted it would be preferential if the distribution fell slower at large values. The two selected combination variables are as follows:

$$XWCOM = -\ln[x_{ws}] \times -\ln[x_{wo}], \tag{5.15}$$

and

$$PT2COM = -\ln[p_{ts}^2] - \ln[p_{to}^2]. \tag{5.16}$$

5.5 Colour Reconnection Effects

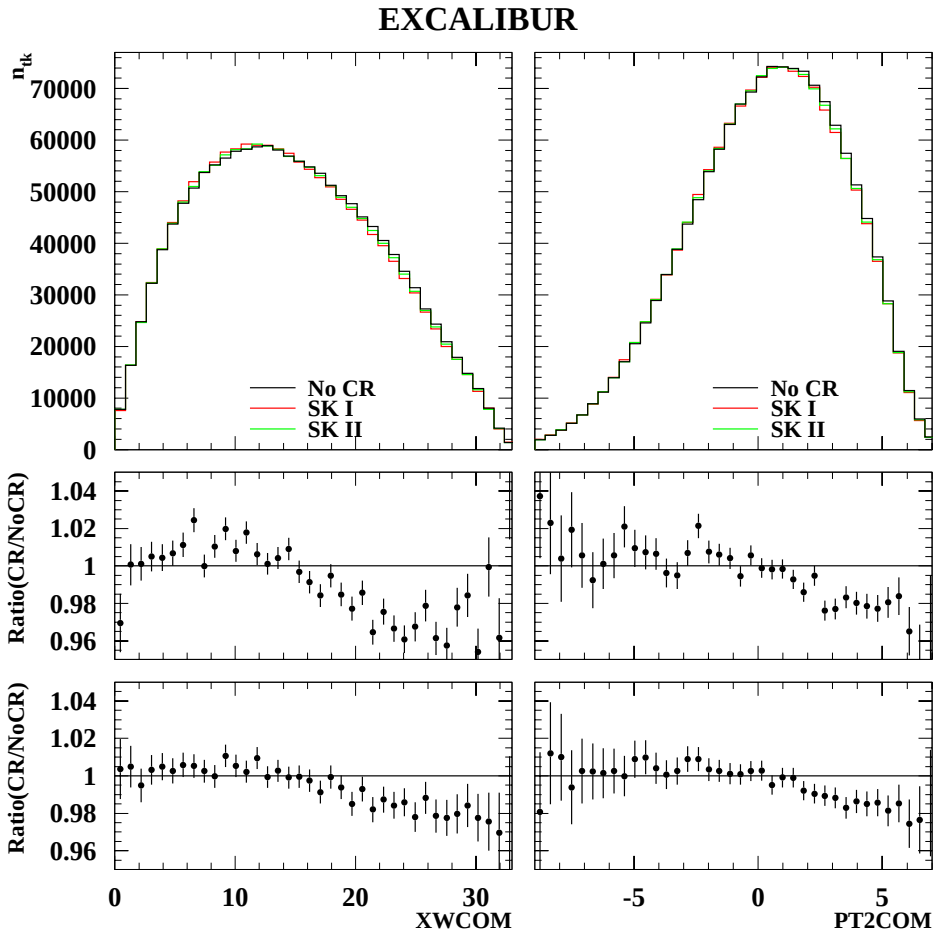

Figure 5.11: *Reconstructed combination variables with the EXCALIBUR/JETSET simulation.*

We are now in a position to test the combination distributions for the effects of colour reconnection. Figure 5.11 shows the sensitivity of the combination variables, *XWCOM* (left) and *PT2COM* (right), to colour reconnection. The distributions at the top show the EXCALIBUR/JETSET prediction without colour reconnection for reconstructed tracks from all generated hadronic events; the red and green lines are the Sjöstrand and Khoze models I and II, respectively. The ratio of the colour reconnected model over the standard simulation is taken and displayed in the middle (SK I/NoCR) and lower (SK II/NoCR) plots. The error bars are the Monte Carlo statistical error. Figure 5.12 shows the regions of the

combination variables affected by the colour reconnection implemented into the HERWIG Monte Carlo.

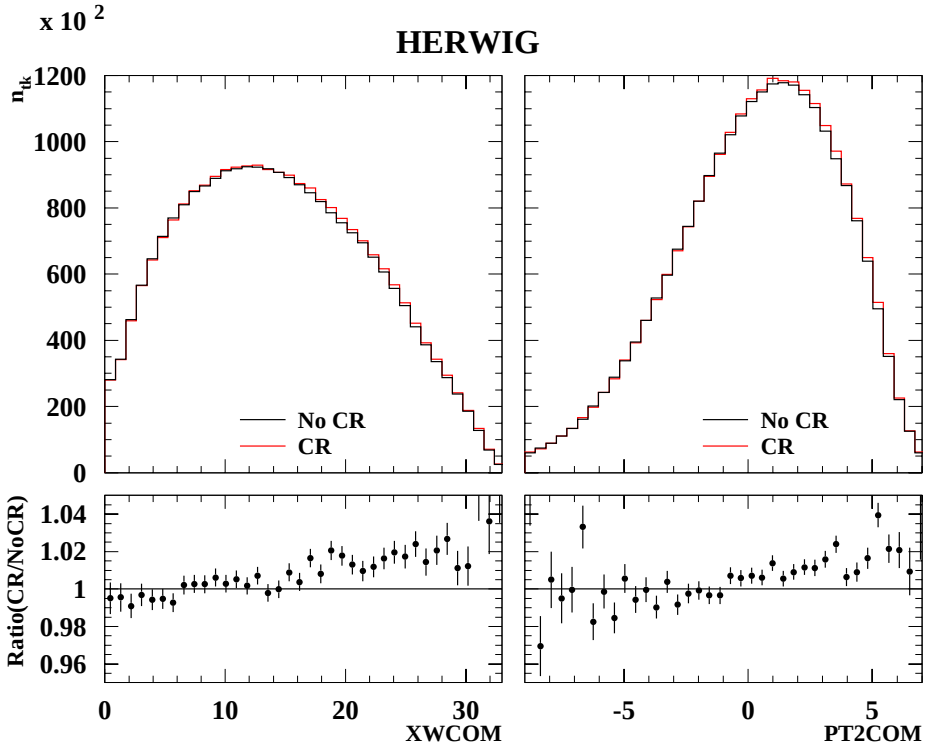

Figure 5.12: *Reconstructed combination variables with the HERWIG simulation.*

Colour reconnection, as clearly shown in Figure 5.11, manifests itself as a deficit at high values for both combinations, while there is also an excess at low values. It is clear that when the distribution is considered as a whole, for example to calculate the multiplicity, then the effects will cancel each other out to some extent. The HERWIG prediction in Figure 5.12, shows entirely the opposite trend, with the excess appearing at high values of the combination. However, it should be noted that the deviation from unity occurs in approximately the same region of the distributions.

There are now three variables which exhibit colour reconnection effects which change across their distribution: *XWCOM*, *PT2COM*, and the rapidity in the 'correct' W rest frame (plot 'a' in Figure 5.6). Now that the regions of the three distributions with expected sensitivity have been identified, it is essential to test how significant an effect (produced by introducing a reconnection model into the

simulation) would be when a data sample of limited size is considered. This is achieved by taking the difference between simulations with and without colour reconnection and dividing it by the statistical error expected in the data sample in that bin of the distribution, thus the significance, S, is given by:

$$S = \frac{n_i^{CR} - n_i^{noCR}}{\sigma_i^{data}}, \tag{5.17}$$

where, n_i^{CR} is the number of normalised fully reconstructed entries in bin i for the reconnected model, n_i^{noCR} is the normalised number of entries for the original simulation and σ_i^{data} is the statistical error on the data in bin i.

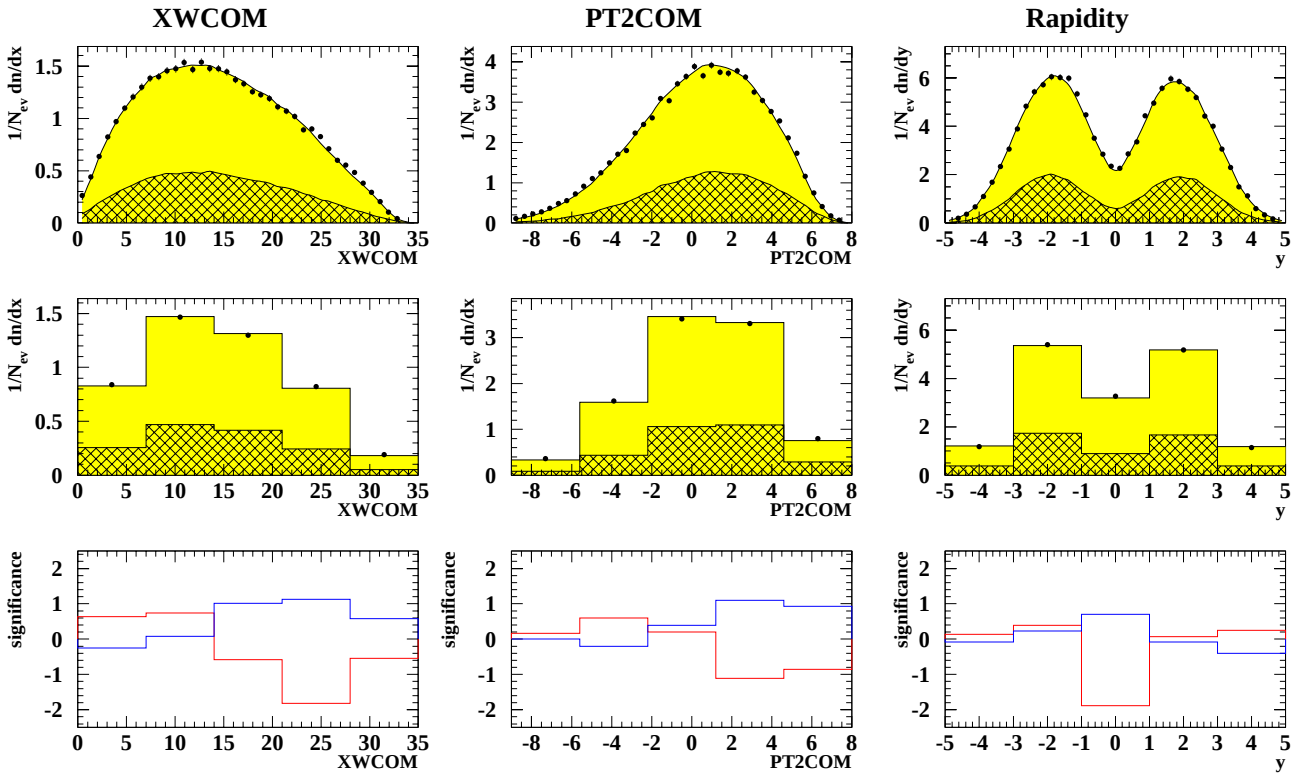

Figure 5.13: *Reconstructed MC/data comparison and significance of CR effect on XWCOM, PT2COM, and Rapidity, with the SK I model implemented into EXCALIBUR (red) and HERWIG (blue).*

Firstly however, the distributions for the fully reconstructed Monte Carlo including backgrounds must be produced and compared with the raw data. To decrease the statistical error on the data, the distributions are re-binned into five

bins, which groups together regions of sensitivity previously stretched over several bins, thus removing scattering and increasing the significance. The value of the significance can be interpreted as being the number of sigma the data would be away from the standard simulation if it agreed perfectly with the modified model including colour reconnection. Figure 5.13 shows the fully reconstructed distributions for selected[9] 189GeV data with forty bins (top), five bins (middle), and the significance of the signal in the five bins (bottom), for the rapidity, *XWCOM*, and *PT2COM* variables. The significance plot shows SK I in red, and the HERWIG model in blue. The fully reconstructed distributions are normalised to a differential cross-section and also display the relative fraction of background.

Figure 5.13 shows that the SK I model predicts up to a 2 sigma effect in some bins, while the HERWIG model predicts up to a 1 sigma effect, which is always in the opposite direction. It should be realised that ideally, we wish to test the data to see how it compares but it is not possible with this distribution because we do not have a colour reconnected, and unconnected data sample, as we do with the simulation. Possibly the only option available to quantify the data's compatibility with the models at this stage, is via a Pearson's χ^2 test (first introduced on page 109) on the three sensitive distributions, given by:

$$\chi^2 = \sum_{i}^{N} \frac{(n_i - \nu_i)^2}{\sigma_{n_i}^2}, \tag{5.18}$$

where n_i is the value of the data in bin i of N bins, ν_i is the predicted value of the model being tested, and σ_{n_i} is the statistical error on the data in bin i. The χ^2 test is conducted on all bins of the distributions, unlike in Chapter 4 where only the last bins were used. This is because here the colour reconnection manifests itself throughout the entire distribution, whereas this was not the case in the previous chapter, and so it is unclear if a limited bin χ^2 is the correct method. However, a χ^2 test is also done on the most significant group of bins in the five bin histogram, *i.e.* the last three bins of *XWCOM*, the last two bins of

[9]Hadronic events are selected as normal, with *outnn*>-0.9 and $\cos\theta_{jet} < 0.9$.

PT2COM, and the central bin of rapidity. Notice that because the normalisation of the theoretical prediction is absolute, there are no degrees of freedom lost for the χ^2 results. The results of the χ^2 tests are given in Table 5.1, Table 5.2 shows the corresponding χ^2 probabilities [13] for each entries in Table 5.1.

Simulation	***XWCOM***		***PT2COM***		**Rapidity**	
	$\chi^2/40$	$\chi^2/3$	$\chi^2/40$	$\chi^2/2$	$\chi^2/40$	$\chi^2/1$
EXCALIBUR	1.108	3.168	2.328	6.419	1.041	4.589
SK I	1.419	6.830	2.472	9.334	1.384	16.215
HERWIG	0.954	0.427	2.097	5.140	1.455	2.986
HERWIG cr	1.027	1.212	2.145	6.425	1.213	1.046

Table 5.1: *χ^2/ndf for the 189GeV data against various simulations for the three colour reconnection sensitive variables, XWCOM, PT2COM and rapidity. χ^2/ndf are displayed for either the full distribution (40 bins) or for the colour reconnection sensitive bins of the 5 bin distribution.*

Simulation	***XWCOM***		***PT2COM***		**Rapidity**	
	χ^2 **Probability (Degrees of Freedom)**					
	Pr(40)	**Pr(3)**	**Pr(40)**	**Pr(2)**	**Pr(40)**	**Pr(1)**
EXCALIBUR	29.4%	2.3%	0.00%	0.16%	39.9%	3.2%
SK I	4.1%	0.01%	0.00%	0.00%	5.4%	0.00%
HERWIG	55.4%	73.3%	0.00%	0.59%	3.1%	8.4%
HERWIG cr	42.3%	30.4%	0.00%	0.16%	16.7%	30.6%

Table 5.2: *χ^2 probabilities for the χ^2/ndf displayed in Figure 5.1.*

The first most notable feature of Tables 5.1 and 5.2 is that none of the simulations produce a good χ^2 for the PT2COM distribution. It is therefore of little value as a colour reconnection sensitive variable at present. A further investigation would need to be launched to identify the problems the simulations have with modeling the distribution before it could be successfully used.

The χ^2 probabilities clearly show that the HERWIG models are the most

accurate descriptions of the data across the XWCOM and rapidity distributions with the colour reconnected model being better still, especially in the sensitive regions. The Sjöstrand and Khoze model I is not seen to reproduce the data very well in either the sensitive regions or the full distributions. In fact, it is bordering on being rejected entirely given its poor performance. However, the aim of this chapter was to instigate a preliminary investigation into the sensitivity of these variables and it should be noted that even with a smaller data sample (189GeV only) than the previous chapter, and a less rigorous investigation, a similar level of discrimination has been achieved. Clearly then, this promising method requires further study, using greater statistics, as well as a full estimate of the systematics before the rejection of the SKI model could be confirmed. It would also be interesting to study the LI distributions in semi-leptonic events with the same aim as Chapter 4; to remove detector modelling inconsistencies by comparing the hadronic data with a 'colour reconnection free' data sample.

5.6 Summary

This chapter has covered a preliminary investigation into new variables which were expected to be more sensitive to colour reconnection than multiplicity and momentum. The three pairs of Lorentz invariant distributions were introduced and the algorithm used to calculate them has been described. Each variable was considered in turn and its sensitivity to colour reconnection was tested. An attempt was made to combine variables together in order to increase the colour reconnection signal and two new distributions were produced. The significance of the observed effect was produced for the limited 189GeV data sample, and up to a two sigma effect was observed in some regions. The data/Monte Carlo agreement was then tested using a χ^2 across the entire distribution and on limited 'signal' regions.

All Monte Carlo models tested with and without colour reconnection are found

to be compatible with the data, with the exception of Sjöstrand and Khoze model I, which is bordering on being rejected. There is a clear indication that the data is more HERWIG-like than JETSET-like. It is concluded that the method 'shows promise' but requires further study with a larger data-set in order to reach greater statistical precision. It was also observed that one of the distributions was not very well modelled; further investigation is needed.

Chapter 6

Summary and Conclusions

6.1 General Overview of Colour Reconnection

The phenomenon of colour reconnection was introduced in Chapter 1 and it was suggested to exist between hadronically decaying W pairs in the e^+e^- collisions at LEP2 above centre-of-mass energies of 161GeV. Naively, when both W bosons decay into quarks they subsequently evolve into multi-particle final states independently. But, theoretically it is perfectly acceptable to assume that there is cross-talk occurring between the two systems, in either the perturbative or non-perturbative stages of the evolution.

Chapter 2 gave discussion to Monte Carlo models of the phenomenon, as well as the naive equivalents without the effect present. The models implemented into the JETSET Monte Carlo reconnect in the non-perturbative phase when strings between the partons cross; several variants on the string structure were considered. The Dipole Model of parton evolution, which constitutes the ARIADNE Monte Carlo reconnects in the perturbative region and two variants of the model were discussed. The method of reconnection implemented into the HERWIG Monte Carlo involves the introduction of an additional step between the perturbative and non-perturbative phases of the usual Cluster Model evolution.

A further model by Geiger and Ellis was briefly discussed, but was not used at any stage of the analysis.

Theoretically, colour reconnection studies predicted only small effects on variables such as the average charged track multiplicity and particle momentum distributions. These variables were investigated in Chapter 4. However, the advantage of the Monte Carlo technique is that any variable can be constructed and tested, and so an additional investigation was launched into new variables which could have an increased sensitivity to the phenomenon; this was the topic of Chapter 5.

6.2 Summary of the Multiplicity Analysis

Hadronic and semi-leptonic events were selected from the ALEPH data-sets from 183GeV to 202GeV, using event selections developed for W mass studies. The neural network selection for hadronic events was modified in an attempt to enhance the efficiency of selecting 'colour reconnected' events. A cut was imposed to reject events if any jets were not well contained. Charged particle momentum distributions were produced and corrected bin-by-bin for both background contamination, and detector-based inefficiencies, but not for transverse momenta. No correction was made for the limited acceptance of the event selections.

The charged hadronic multiplicity of the two event types was calculated by integrating the relevant corrected fragmentation function. The multiplicity and momentum distribution from hadronic events were compared with those produced by the hadronic part of semi-leptonic events for the effects of colour reconnection in the hadronic sample. Comparisons were also made to various simulations with and without colour reconnection present. The simulated data was also used to remove any bias introduced into the final multiplicities due to the limited acceptance of the event selections. Various systematic uncertainties were considered and studied in detail at 183GeV and 189GeV, which were then attached to the fi-

nal distributions and multiplicities obtained. The six data samples were combined to form a larger sample with greater statistical precision, which was subsequently tested in the same way.

No evidence is seen for colour reconnection at the present level of statistics available in either charged particle momenta or multiplicities. All models with and without implementations of colour reconnection that have been tested are seen to be compatible with the data, although some are marginal. There is a clear hint that the data is more like the HERWIG simulations.

6.3 Summary of the Lorentz Invariant Analysis

Chapter 5 presented a preliminary study of a potentially new method of examining colour reconnection effects, based on particle distributions such as rapidity, scaled momentum and transverse momentum, but redefined in terms of Lorentz invariant products of 4-vectors. The algorithm used to obtain the variables was described and the method was found to be able to reproduce the three particle distributions in the rest frames of either of the W bosons in the event, giving a total of six distributions. The information about a particle's 'position' in respect to both of the W particles was used to construct two new variables, which are believed will concentrate the colour reconnection effects seen in the individual distributions.

These combination variables suggested they were sensitive to colour reconnection across their entire range, with a deficit in one region and an excess in another. The significance of the expected Monte Carlo 'signal' was determined using the 189GeV data sample. The significance was seen to be as large as 2 sigma in several bins, it is therefore concluded that the method 'shows promise'. Most simulations, both with, and without colour reconnection implementations were found to be compatible with the 189GeV data sample after a χ^2 test was conducted across both, the full spectrum, and for a limited region of the distri-

butions. However, there is again a clear indication that the data appears to be more HERWIG-like, than JETSET-like.

6.4 Into the Future

6.4.1 Multiplicity and Momentum Study

This study is effectively complete in many respects, except that the data collected in the Year 2000 will need to be analysed to further increase the statistical precision. It must be noted though, that the event selections were originally developed by the W mass group for use on the 183GeV data, and ideally need to be updated for the higher energy data recorded in 1999 and 2000. It is also clear that several of the systematics need updating, or alternatively the cause of any uncertainty should be identified and eliminated, because with the increase in statistics, the results are already becoming systematics limited. There is also an additional interest in producing a LEP-wide colour reconnection result, which combines the findings of the four LEP experiments. This would involve producing a correction procedure common to all four experiments, thus making the results compatible and a combination possible.

6.4.2 Lorentz Invariant Study

This study is far from being complete, and it is the author's view that it has the potential to make a good project for a postgraduate student, possibly along the following lines:

- An examination of the variables first developed by the L3 collaboration [84, 85], which look at the particle-flow as a function of angle between the jets of hadronic 4-jet WW events. This is also of interest for a LEP-wide examination of these variables.

- A new event selection could be developed, in the attempt to select events most likely to contain more colour reconnection, rather than just simply as many hadronic WW events as possible.
- The Lorentz invariant and 'L3' distributions should be tested against semi-leptonic events, for all the available data samples; this would involve using an updated kinematic fit.
- A full systematic study would also need to be conducted.

6.5 Closing Comments

Colour reconnection is found to be a stimulating and important feature of the decaying W bosons produced at LEP2. The rigorous search for the effect will continue with enthusiasm and effort until the end of the LEP experiments. It would make an interesting exercise for the Next Linear Collider, wherever it may be built, to continue the search with vastly increased luminosity producing the superior statistical power required to settle the colour reconnection mystery once and for all.

Appendix A

Global Variables and Jet-Finding

Global event variables are used to condense the complex distribution of particles within the event into one simple measure in order to produce a global picture of the event structure. This appendix describes the global event variables used in the WW event selections described in Section 4.2 and in the calculation of the Lorentz Invariant variables of Chapter 5.

Jet-finding is an essential part of any analysis involving a multi-particle final state. In this thesis, knowledge of jet orientations is used not only as an aid to distinguish signal and background (see Section 4.2), but also to identify which parent W particle, tracks were produced by.

A.1 Global Event Shape Variables

Thrust

The thrust axis $\vec{n}_T$ is along the direction $\vec{n}$ which maximises the following quantity:

$$T = \frac{\sum_i |\vec{p}_i \cdot \vec{n}|}{\sum_i |p_i|}, \tag{A.1}$$

where p_i is the momentum of particle i. The magnitude of the thrust vector lies between $0.5 < T < 1$, where $T \approx 1$ implies a dijet event, and $T \approx 0.5$ implies an

isotropic event.

Sphericity

The momentum tensor is defined as [86]:

$$S_{\alpha\beta} = \frac{\sum_i p_i^\alpha p_i^\beta}{\sum_i p_1^2}, \tag{A.2}$$

where $\alpha, \beta = 1, 2, 3$ are the spatial co-ordinate labels. The sphericity, S, of an event is calculated from two of the eigenvalues of the momentum tensor, Q_1 and Q_2, so that,

$$S = \frac{3}{2}(Q_1 + Q_2). \tag{A.3}$$

S lies between $0 < S < 1$, where $S \approx 0$ corresponds to a dijet event and $S \approx 1$ an isotropic one.

Fox-Wolfram Moments

Rather than using an event axis, these event shapes are based on rotationally invariant observables. If $Y_m^l(\Omega)$ are the usual spherical harmonics, then,

$$H_l = \left(\frac{4\pi}{2l+1}\right) \sum_{m=-l}^{+l} \left| \sum_i Y_m^l(\Omega_i) \frac{|\vec{p_i}|}{\sqrt{s}} \right|^2. \tag{A.4}$$

In practice, the first two moments, H_0 and H_1, are constrained by energy-momentum conservation to be 0 and 1, respectively. Higher moments express independent information about the event. Further details can be found in [87, 88].

Acolinearity and Acoplanarity

The event is split into hemispheres defined by the plane perpendicular to the thrust axis (defined above). In each hemisphere a 4-vector is produced from the sum of all the particles in that hemisphere. Acolinearity [71] is defined as the angle between these two 4-vectors. Acoplanarity [71] is the difference between the ϕ component of the two 4-vectors.

A.2 Jet-Finding Algorithms

In general, a jet-finding algorithm runs as described below. First, a 'distance' or y parameter is calculated between pairs of reconstructed objects. y is defined as,

$$y_{ij} = \left(\frac{M_{ij}}{E_{vis}}\right)^2, \tag{A.5}$$

where M_{ij} is some mass variable for the pair of objects ij, and E_{vis} is the total visible energy in the event. The pair of reconstructed objects which minimise y are combined, or clustered together into a pseudo-particle, and the process is repeated without discriminating against the pseudo-particles. Eventually the clustering algorithm stops when no further pairs exist below a predefined value, y_{cut}. There will now remain only a small number of pseudo-particles and they are referred to as jet-vectors. Alternatively, the event may be forced to a particular number of jets by stopping the algorithm when the appropriate number of jets is found. In this case, the y value where the event changes configuration is recorded and can be used to identify how difficult it is to force an event into that topology. For example, y_{34} is the value needed to combine two existing jets of a 4-jet event to form a 3-jet event.

There are several algorithms available to reconstruct jets, the JADE algorithm being the first. Produced by the JADE collaboration, it defined the invariant mass or a pair of objects to be,

$$M_{ij} = 2E_iE_j(1 - \cos\theta_{ij}). \tag{A.6}$$

However, this allowed soft objects to be clustered together even though they were at large angles, leading to spurious results. The DURHAM algorithm was introduced to tackle this problem and had an alternative definition for the invariant mass of a pair of objects to be clustered:

$$M_{ij} = 2\min[E_i^2, E_j^2](1 - \cos\theta_{ij}). \tag{A.7}$$

It also had a selection of schemes to define the 4-momenta of the objects to be clustered: P, E and PE. The P scheme forms massless jets by basing the clustering

solely on the directions, while the E scheme simply sums the 4-momenta of the objects. The PE scheme clusters using the P scheme but also calculates the mass of the jet via the E scheme. It is the DURHAM PE scheme that is used within this thesis; for a more detailed review of jet-finders used by the ALEPH collaboration for extraction of the W mass, refer to [81].

Appendix B

Hadronic Neural Network Inputs

Presented here, are the 19 variables inputted to the hadronic neural network selection described in Section 4.2.1. Each variable is calculated for all events which have passed the hadronic pre-selection; therefore all events will have a corresponding output value between -1 and 1. All plots show the 189GeV raw data (points) with statistical error bars, the fully reconstructed MC prediction (yellow), and the backgrounds (hashed). The Monte Carlo distributions have been normalised to the luminosity of the data.

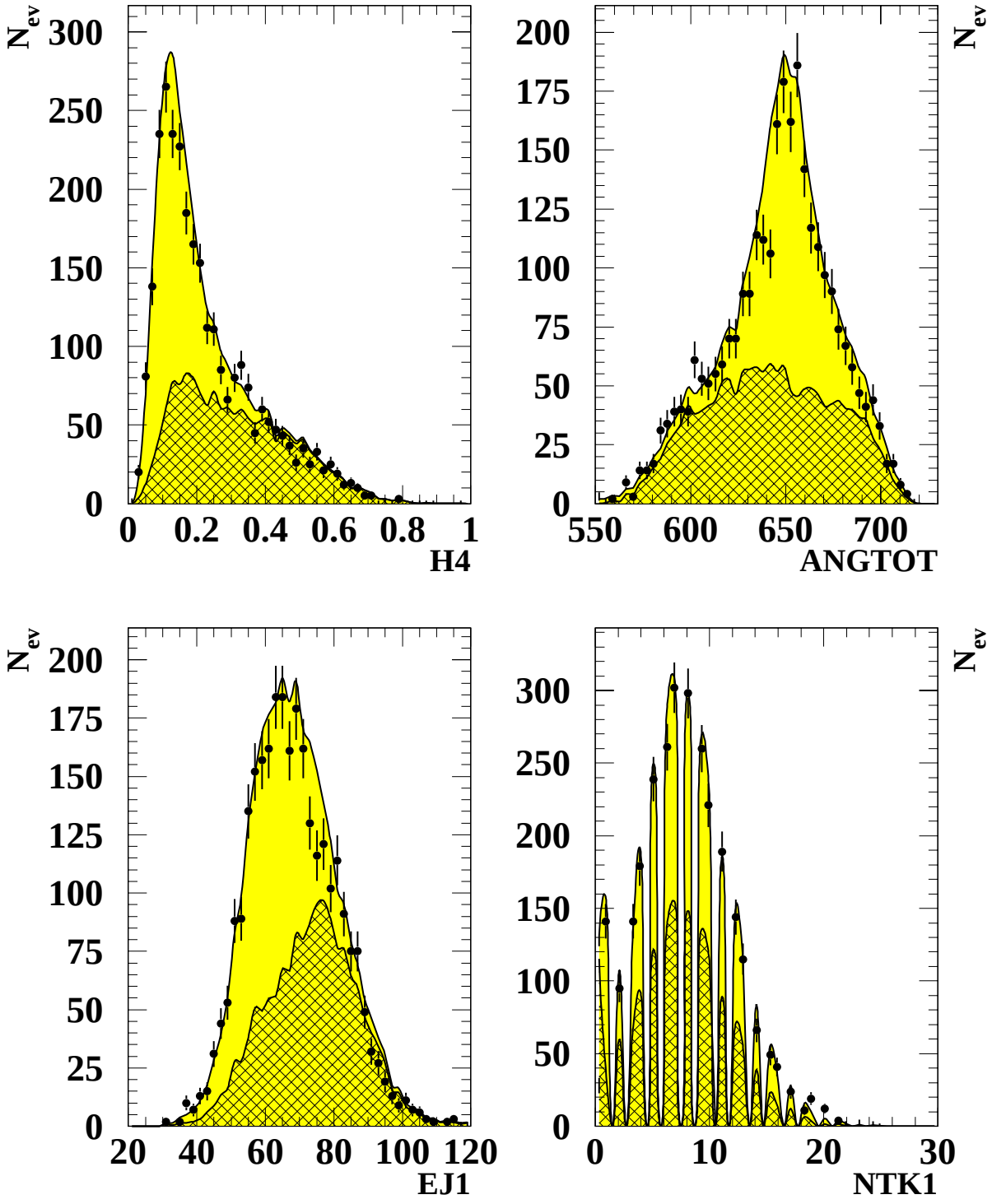

Figure B.1: *1) Fox-Wolfram moment (H4), 2) Sum of the cosines of the six angles between the jets (ANGTOT), 3) Total energy of the most energetic jet (EJ1), 4) Number of tracks in first jet (NTK1).*

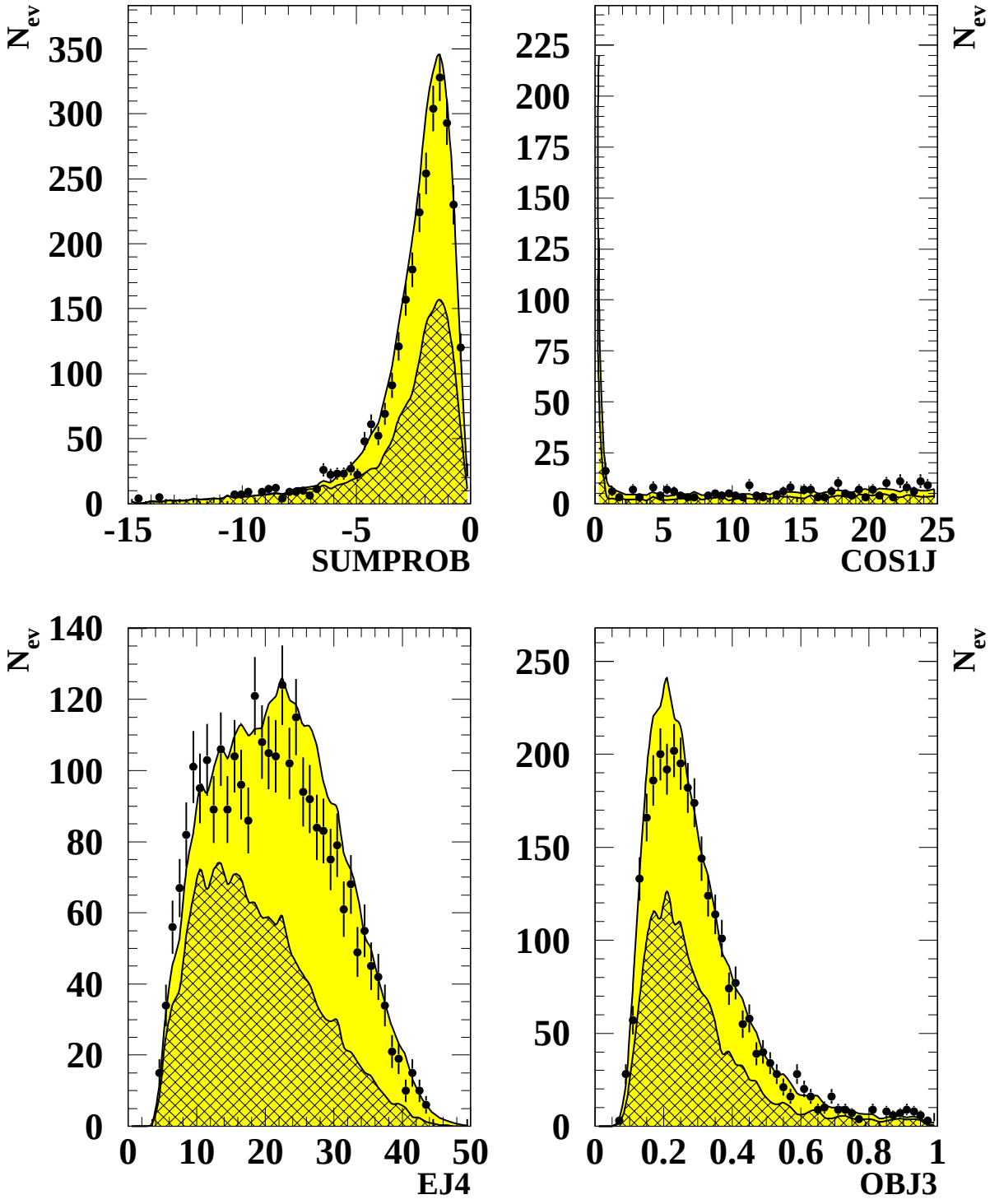

Figure B.2: *5) Sum of the b-tag probabilities of the four jets (SUMPROB), 6) Sum of angles between highest energy track and all other tracks in first jet (COS1J), 7) Momentum of jet 4 (EJ4), 8) Highest energy of any object in third jet (OBJ3).*

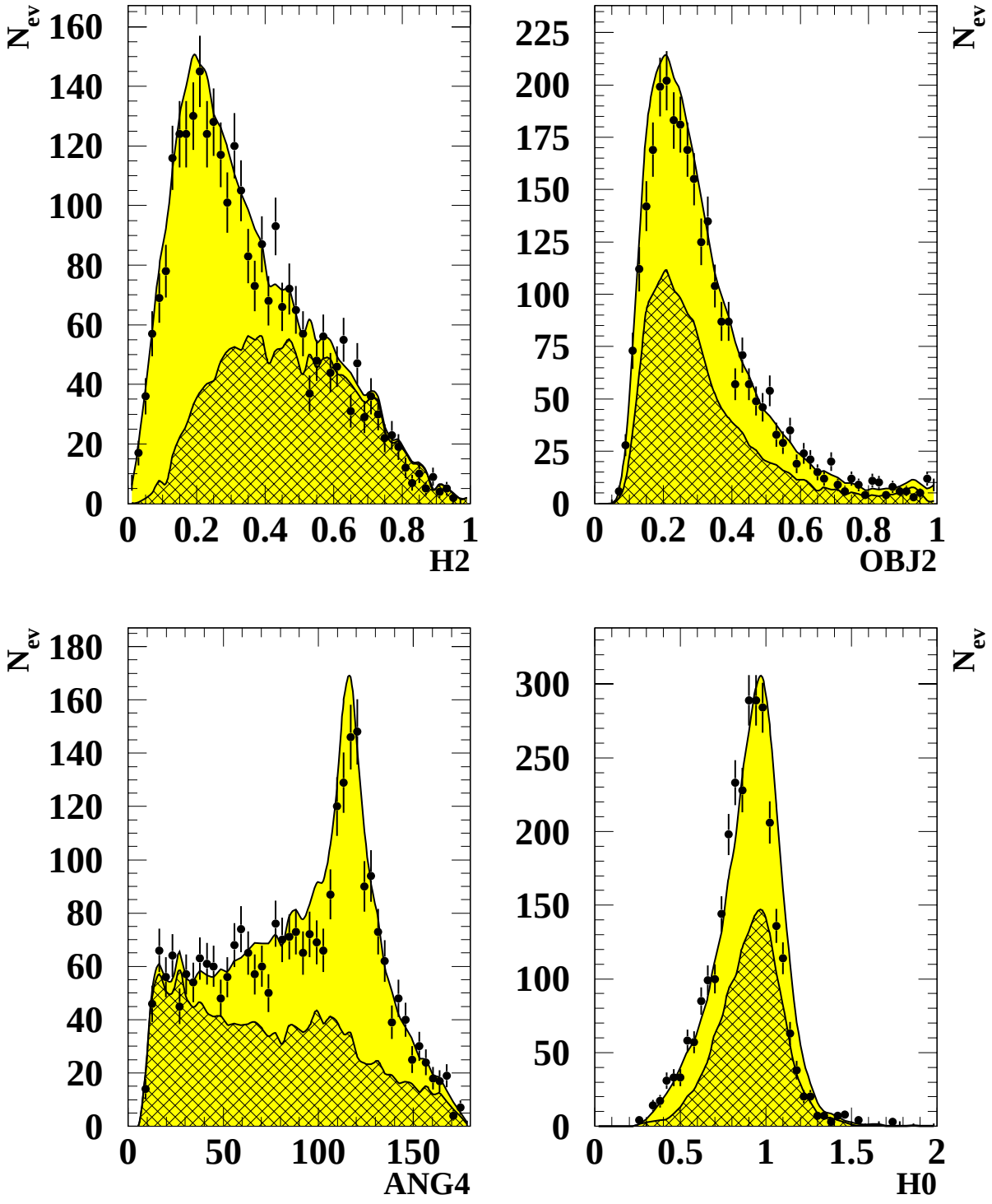

Figure B.3: *9) Fox-Wolfram moment (H2), 10) Highest energy of any object in second jet (OBJ2), 11) Cosine of the angle between the second and third jets (ANG4), 12) Fox-Wolfram moment (H0).*

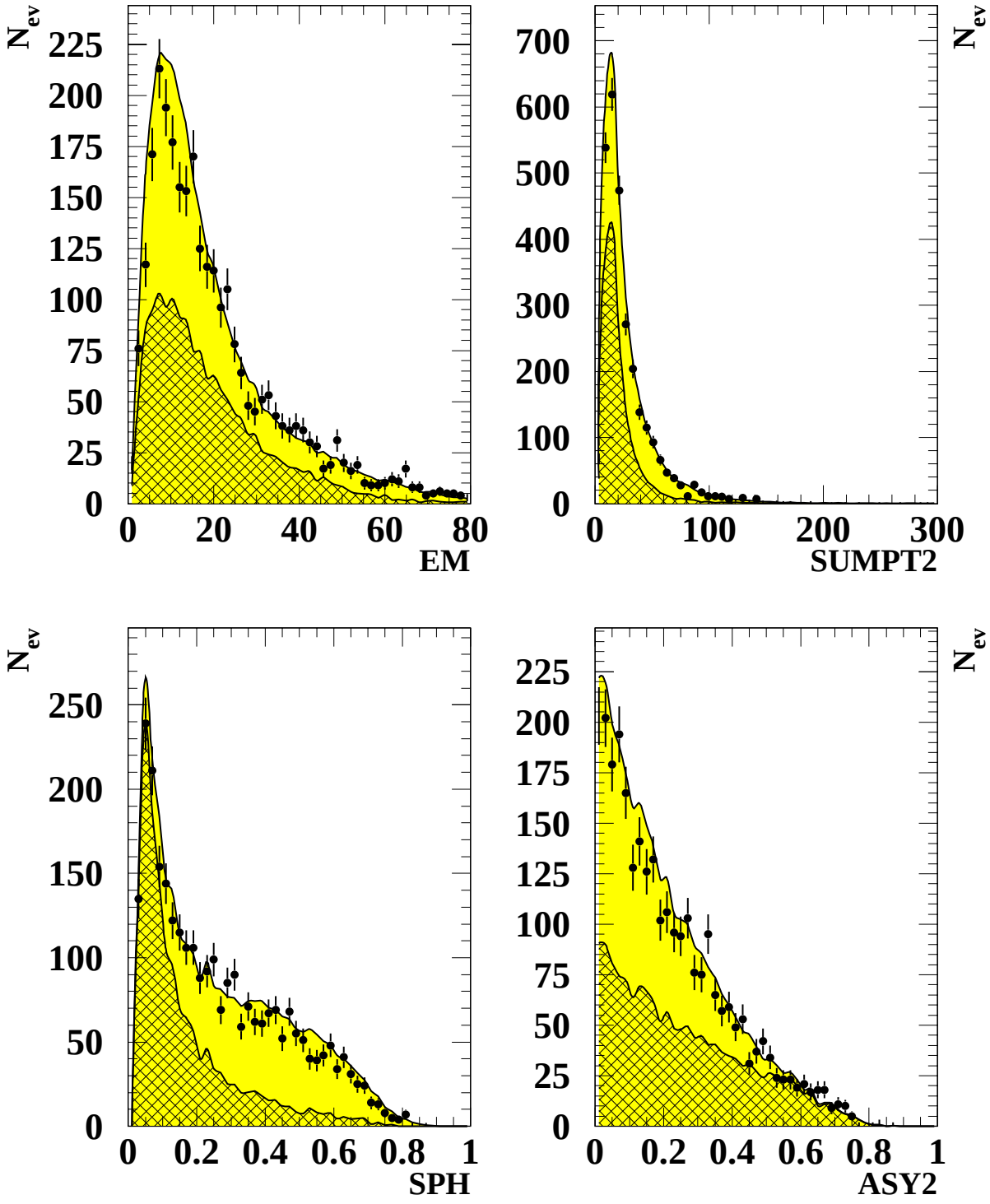

Figure B.4: *13) Missing energy in the event (EM), 14) Sum of the squared transverse momenta of tracks in the second jet (SUMPT2), 15) Sphericity (SPH), 16) Asymmetry between the second and third jets (ASY2).*

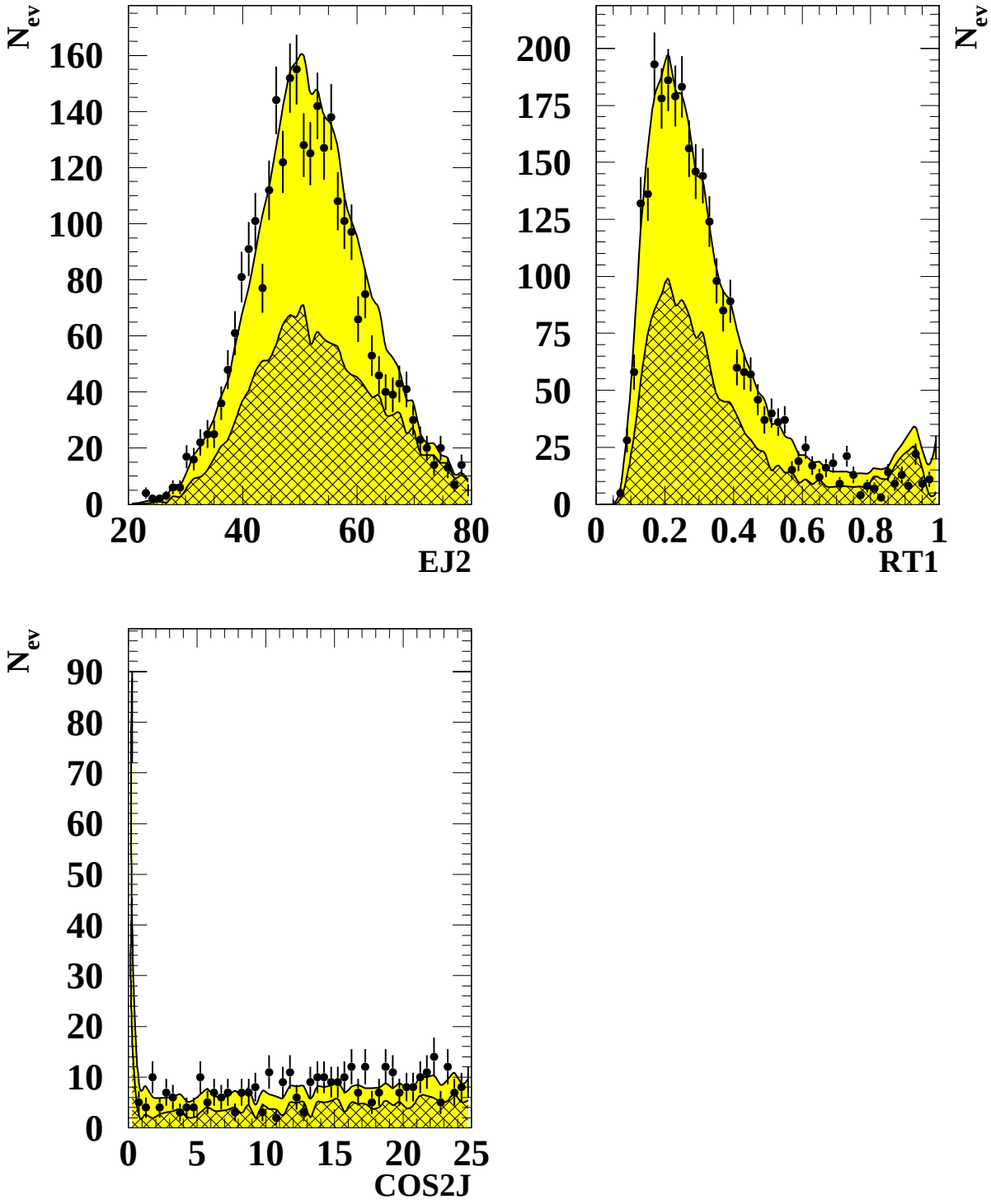

Figure B.5: *17) Energy of the second jet (EJ2), 18) Highest energy of any object in first jet (OBJ1), 19) Sum of angles between highest energy track and all other tracks in second jet (COS2J).*

Appendix C

Close Track Resolution Distributions

Presented here, are the distributions resulting from the systematic study described in Section 4.5.7. All plots show the Z^0 data sample recorded at the beginning of 1997 (points), with statistical errors, and the appropriate Monte Carlo sample generated using PYTHIA/JETSET (yellow). The first set of plots, (there being one for each of the twenty-one TPC pad rows) show the basic minimum distance of closest approach of any of the tracks in an event to a TPC hit on the track in question. The distributions are normalised to a differential cross-section. The second set of plots shown are for the same distribution but have been normalised to $\frac{1}{2\pi N_{evt}} \frac{dn_{tk}}{r(dr)^2}$. The extra criterion of $2\pi \times rdr$ is included so as to remove the unwanted phase space factor in the previous plots, (as explained in Section 4.5.7). This releases the knowledge that the region of inefficiency produced by the TPC's resolution of two close tracks occurs when the tracks are separated by less than 4cm; this is true for all twenty-one TPC pad rows.

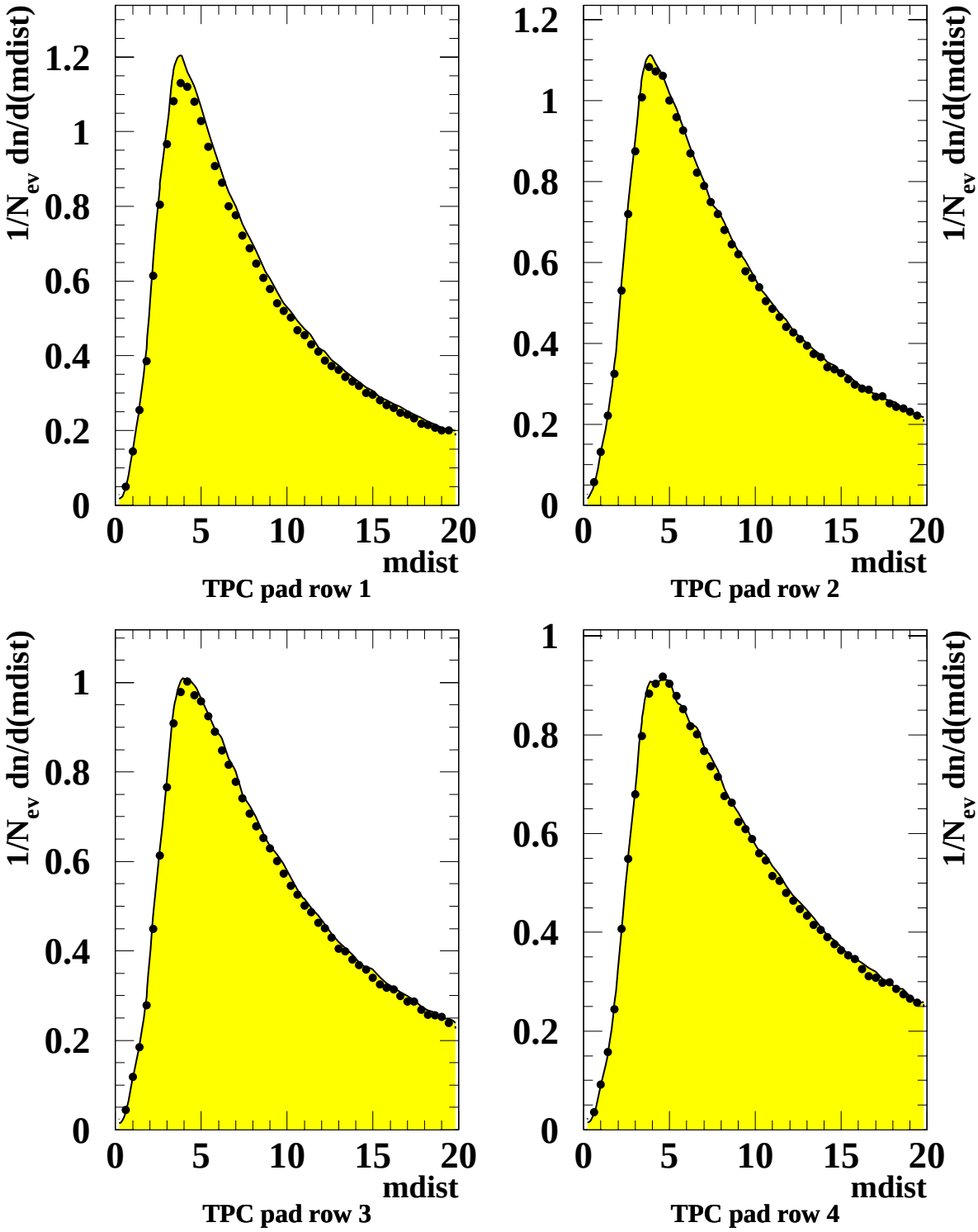

Figure C.1: *Minimum distance of closest approach, TPC pad rows 1-4.*

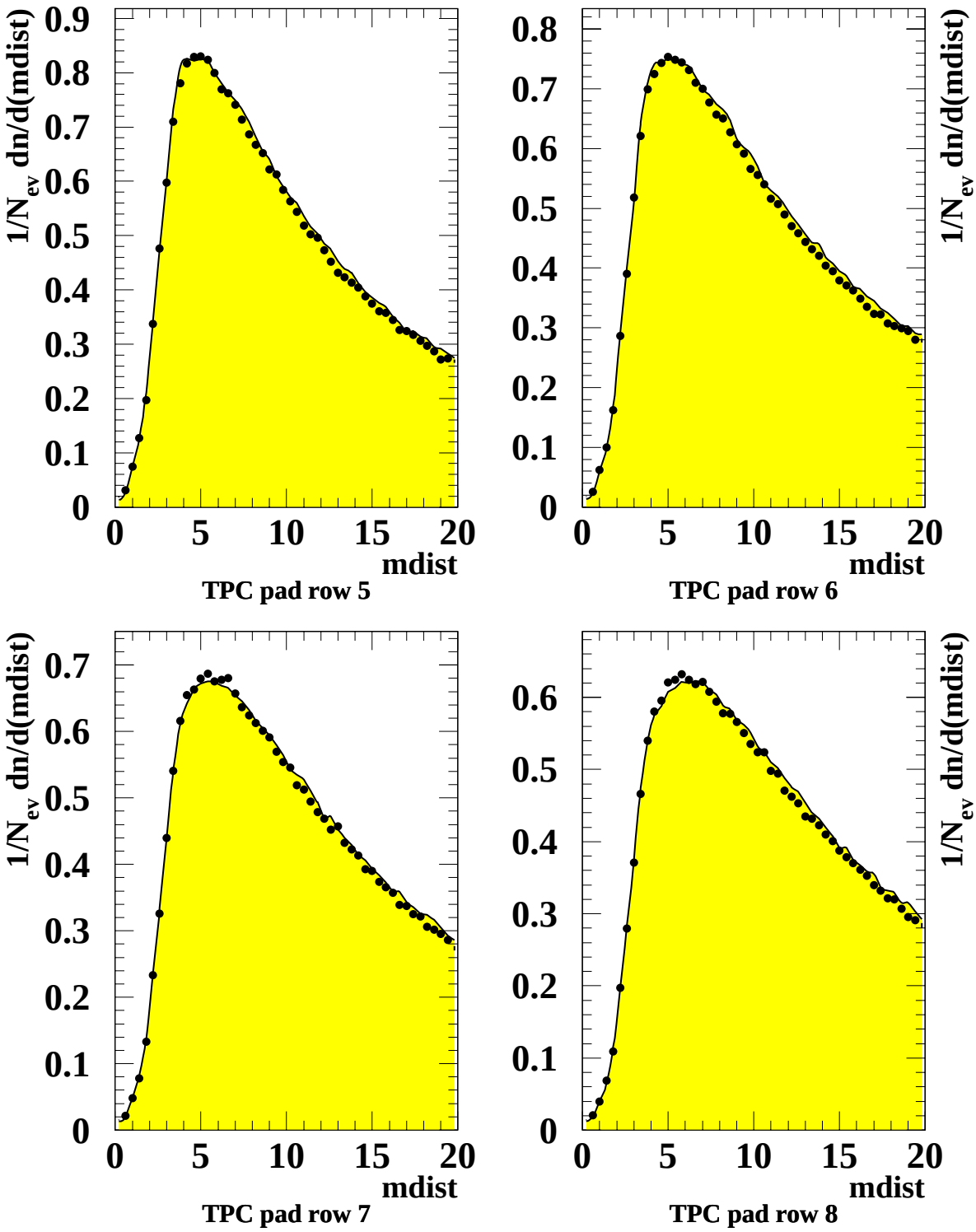

Figure C.2: *Minimum distance of closest approach, TPC pad rows 5-8.*

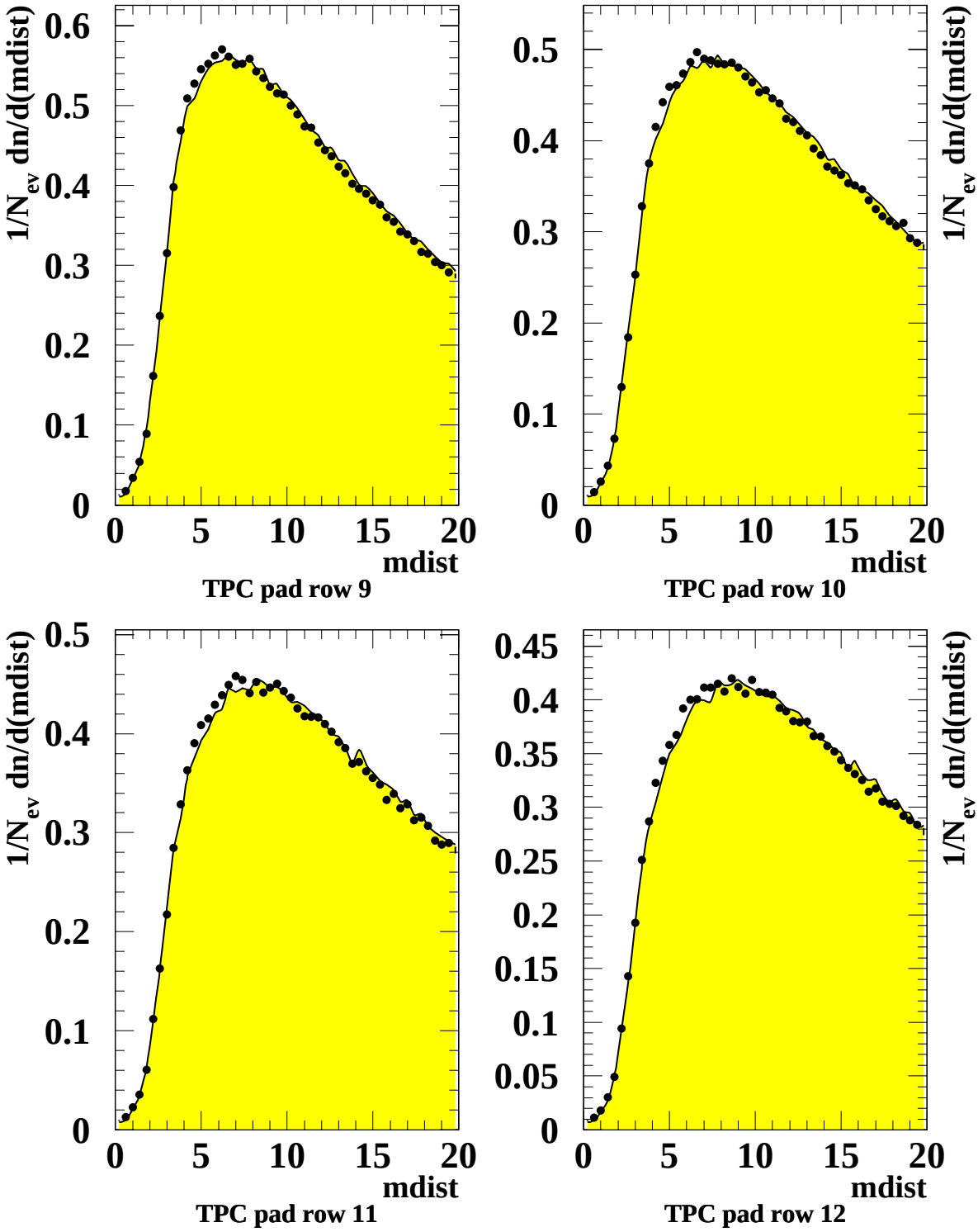

Figure C.3: *Minimum distance of closest approach, TPC pad rows 9-12.*

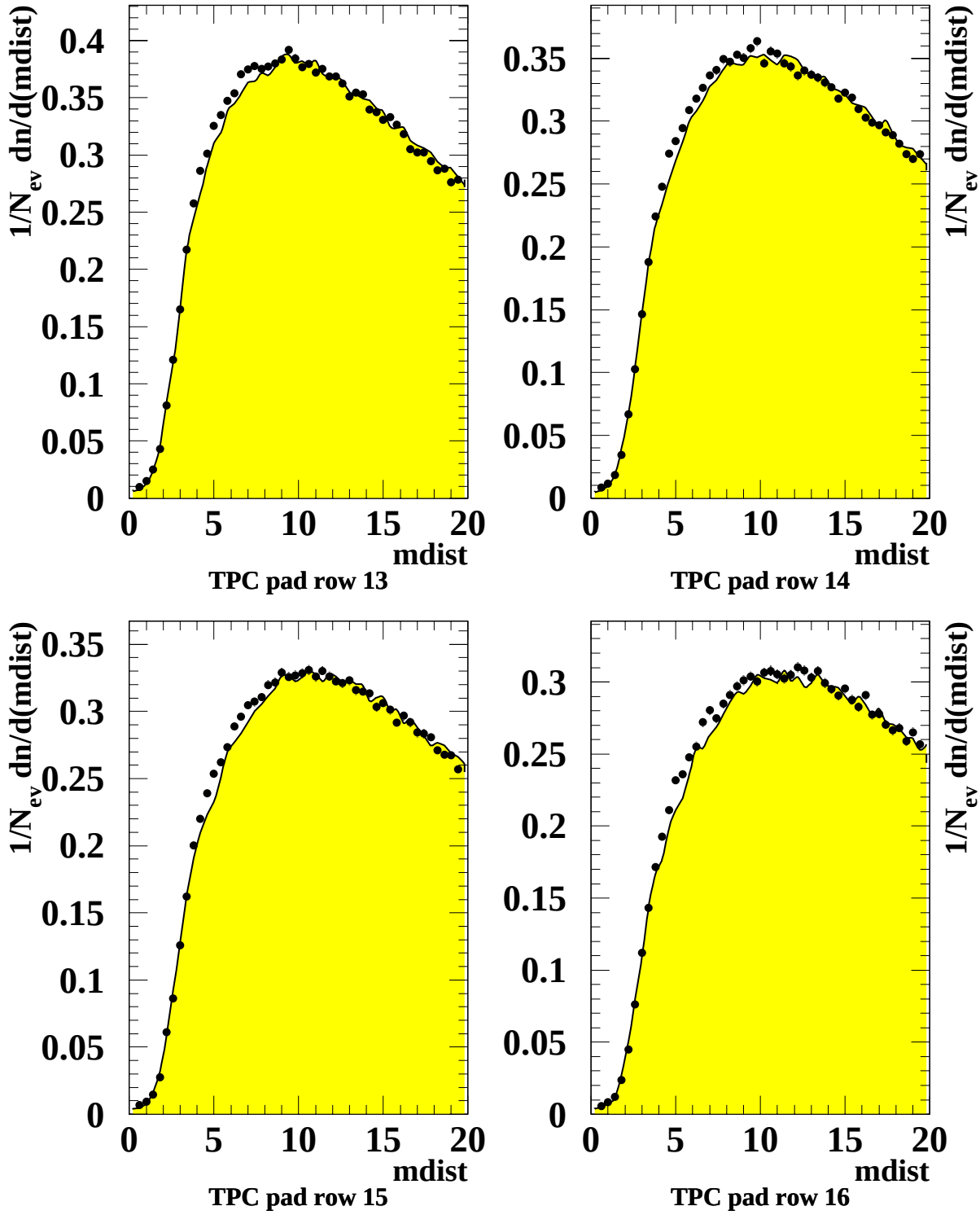

Figure C.4: *Minimum distance of closest approach, TPC pad rows 13-16.*

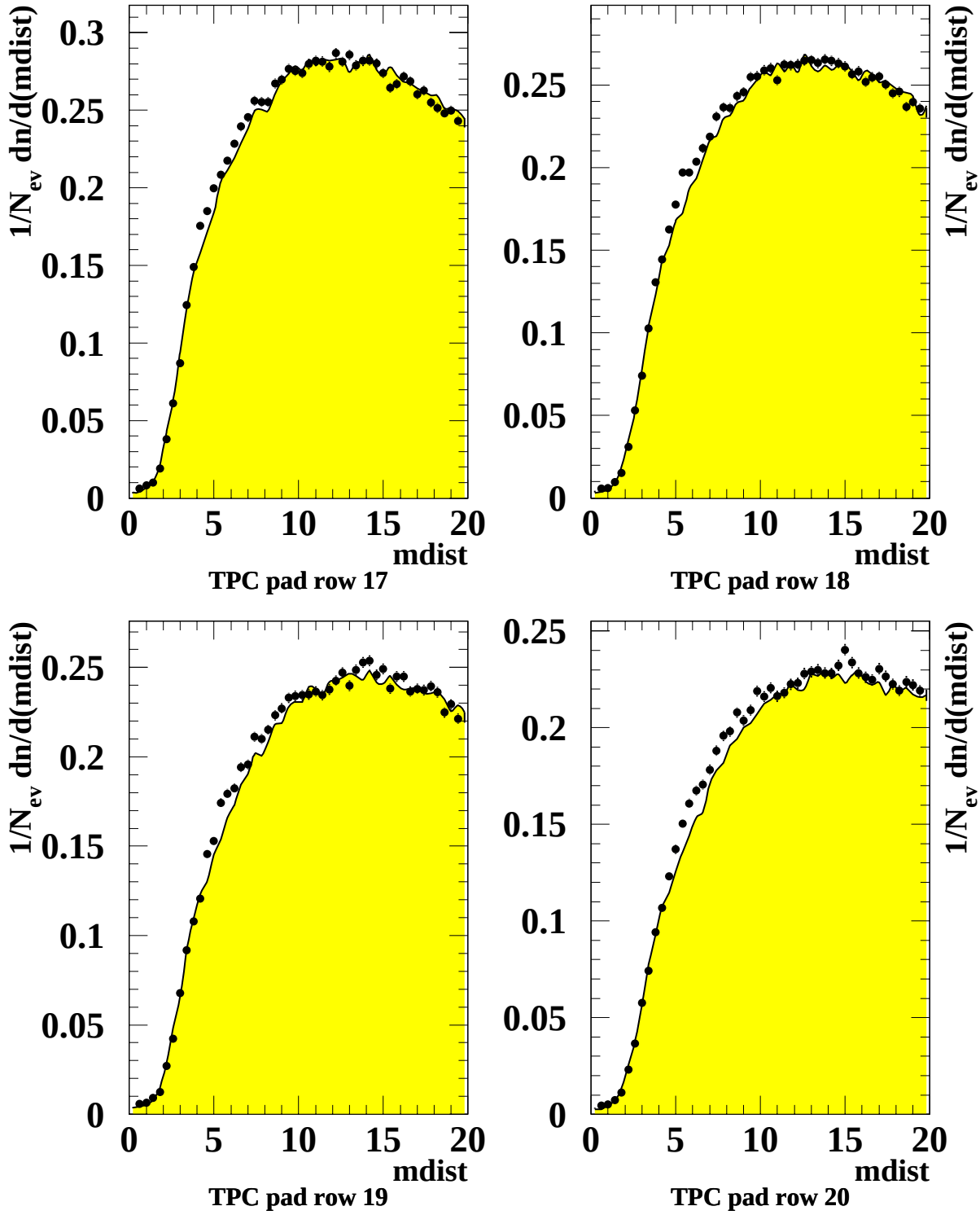

Figure C.5: *Minimum distance of closest approach, TPC pad rows 17-20.*

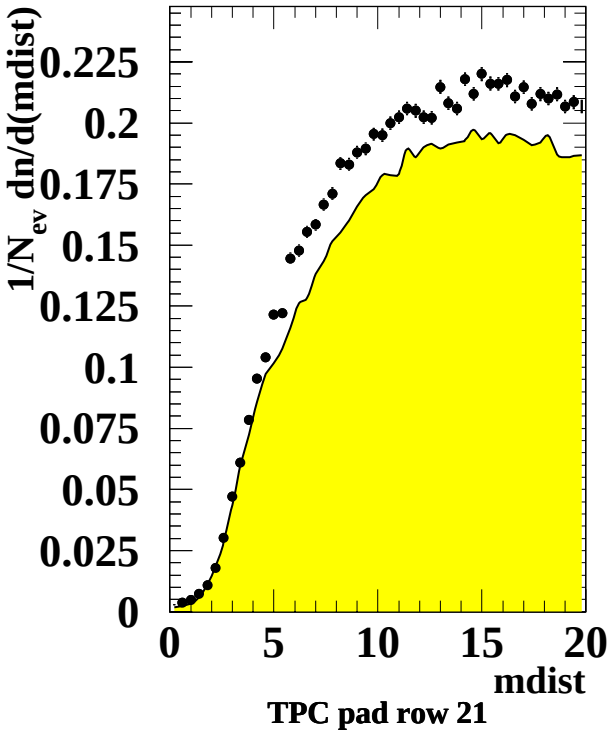

Figure C.6: *Minimum distance of closest approach, TPC pad row 21.*

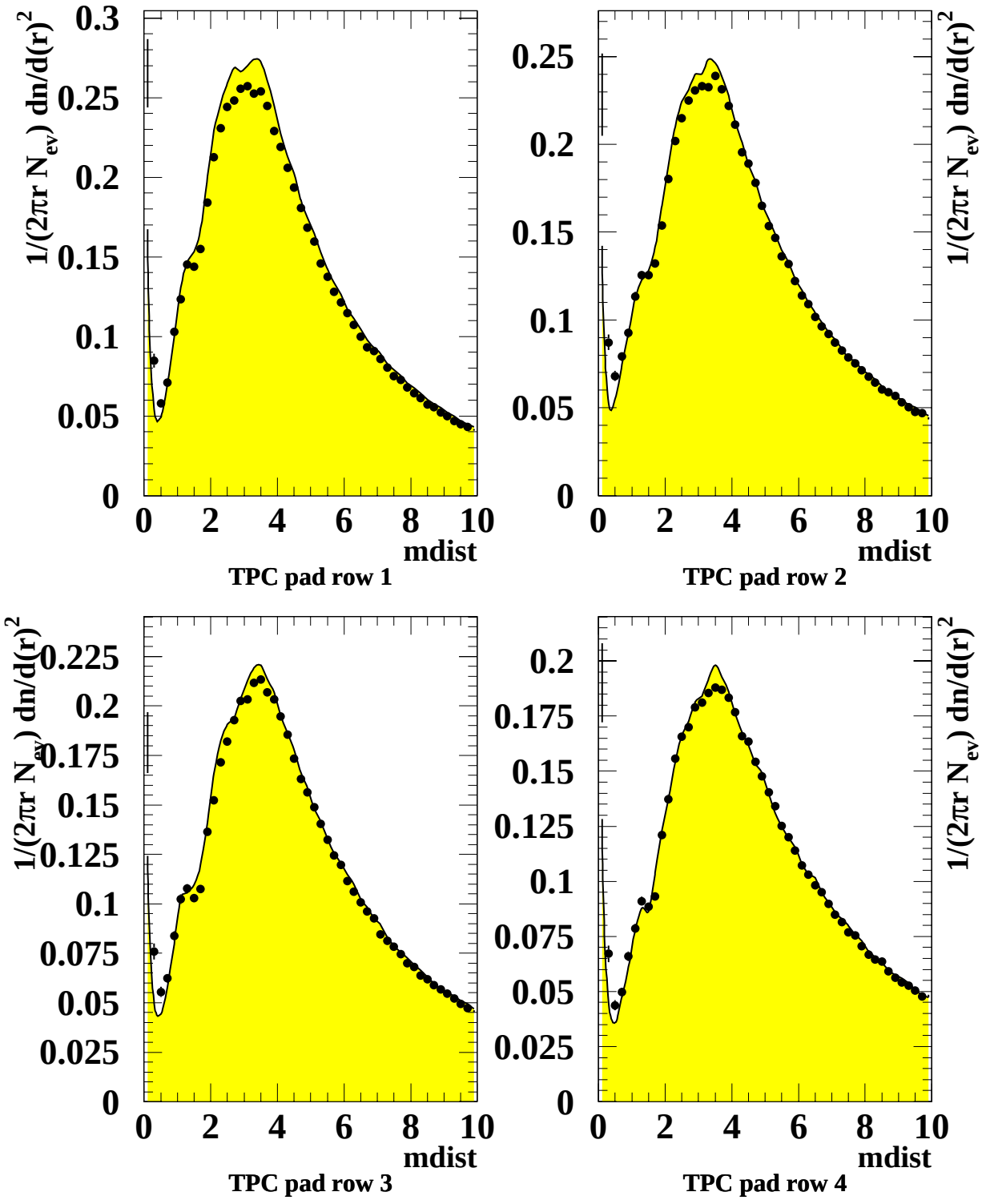

Figure C.7: *Minimum distance of closest approach without* $2\pi r dr$*, TPC pad rows 1-4.*

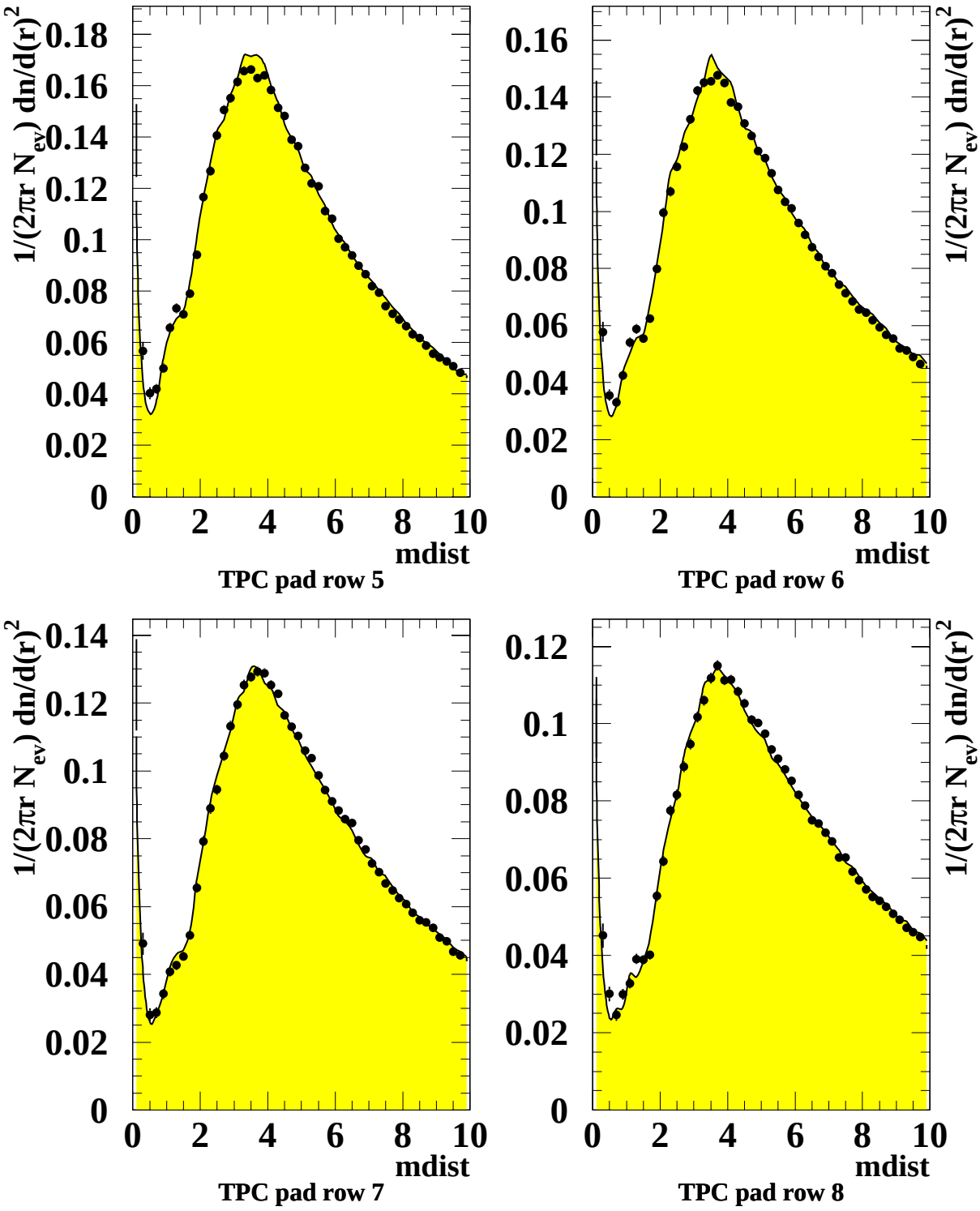

Figure C.8: *Minimum distance of closest approach without* $2\pi r dr$*, TPC pad rows 5-8.*

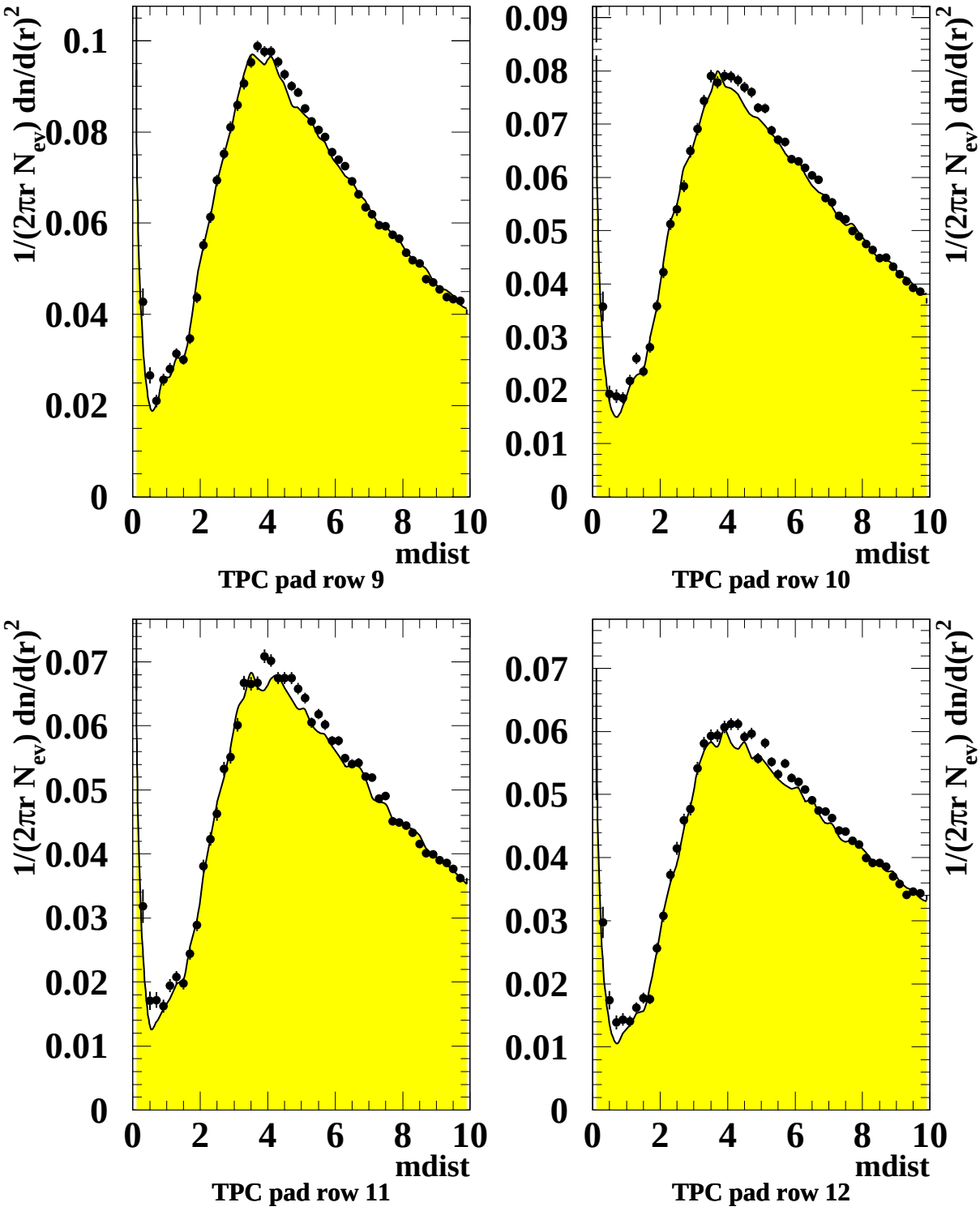

Figure C.9: *Minimum distance of closest approach without* $2\pi r dr$*, TPC pad rows 9-12.*

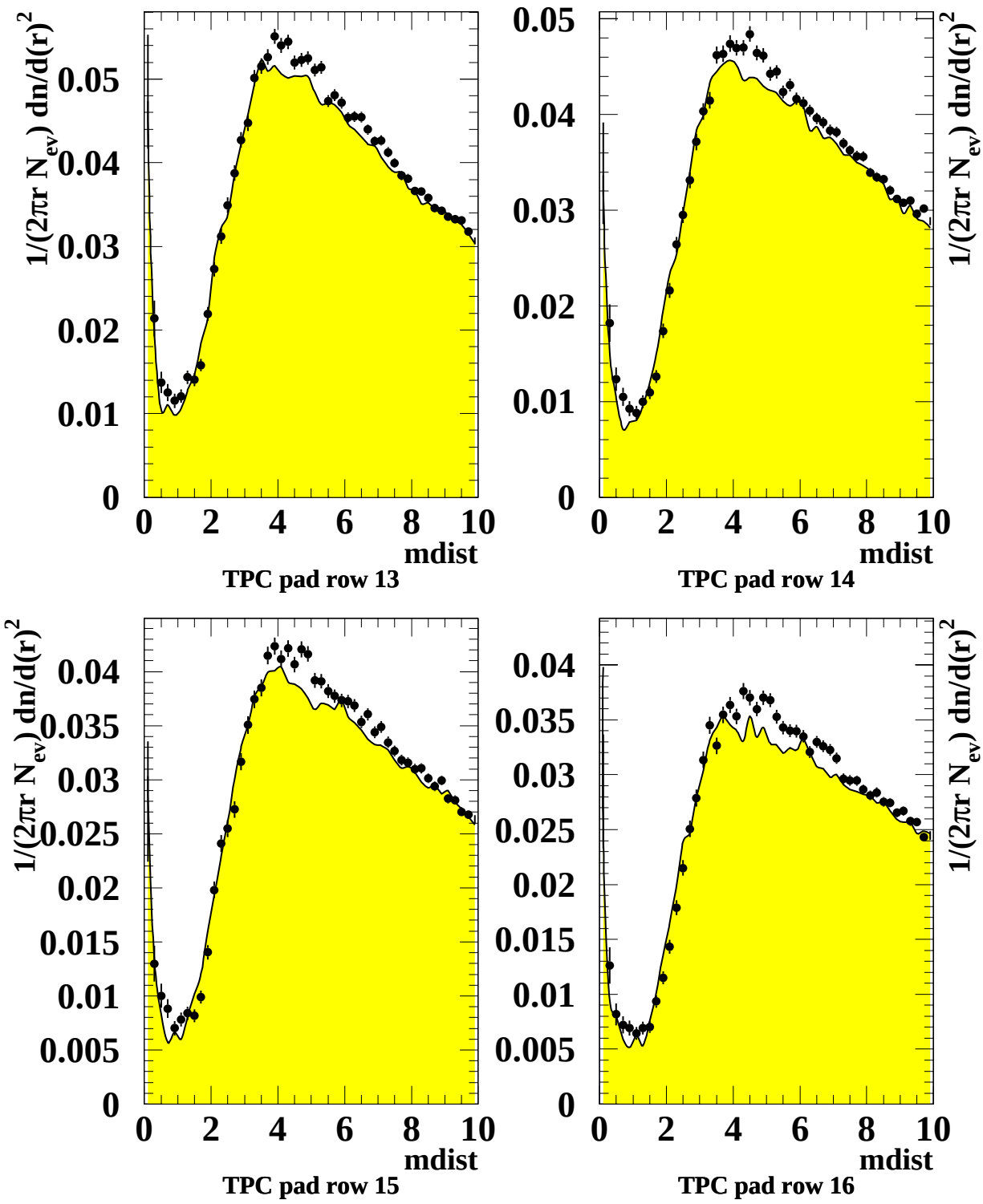

Figure C.10: *Minimum distance of closest approach without* $2\pi r dr$*, TPC pad rows 13-16.*

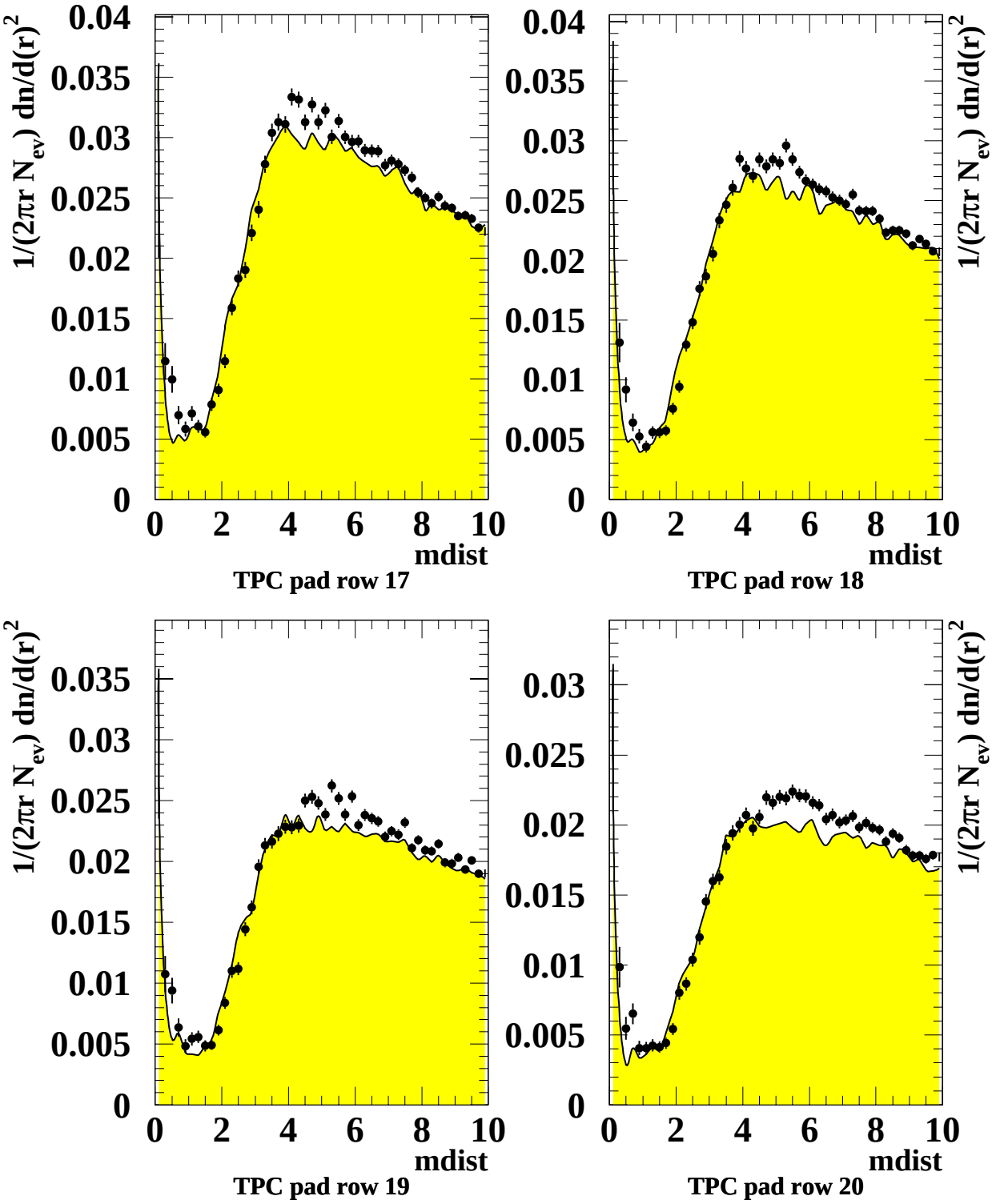

Figure C.11: *Minimum distance of closest approach without* $2\pi r dr$*, TPC pad rows 17-20.*

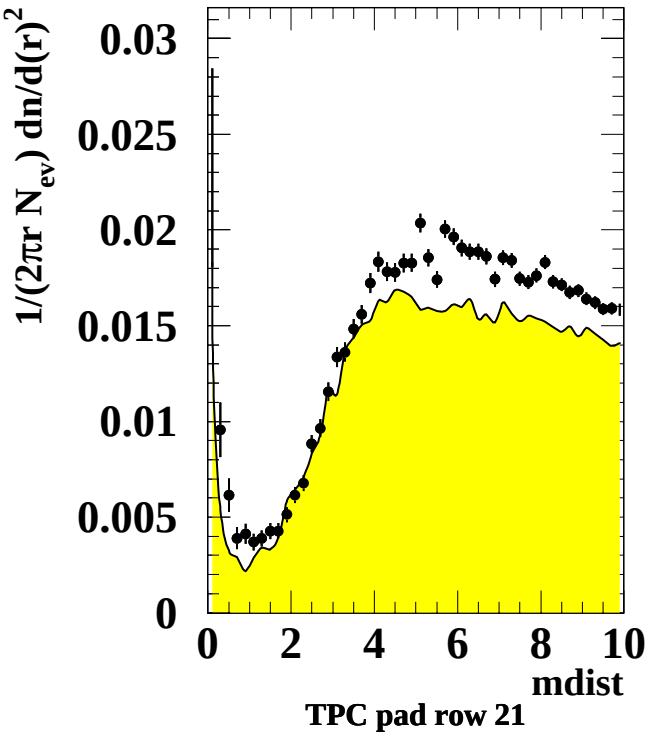

Figure C.12: *Minimum distance of closest approach without* $2\pi r dr$*, TPC pad row 21.*

Bibliography

[1] Francis Halzen and Alan Martin, 'Quarks and Leptons: An Introductory Course in Modern Particle Physics', (1984) John Wiley & Sons, New York.

[2] B.R. Martin and G. Shaw, 'Particle Physics', (1992) John Wiley & Sons, New York.

[3] 'Techniques and Concepts of High Energy Physics X', Proceedings of the 10^{th} NATO ASI Summer School, St Croix, US Virgin Isles, edited by Tom Ferbel, (1998) Kulwer Academic Publishers, Boston.

[4] H.D. Young, 'University Physics - Tenth Edition', (2000) Addison Wesley Longman, San Francisco.

[5] I.S. Grant and W.R. Phillips, 'Electromagnetism', (1992) John Wiley & Sons, New York.

[6] R. Adler, M. Bazin and M. Schiffer, 'Introduction to General Relativity - 2^{nd} Edition', (1975) McGraw-Hill, London.

[7] F. Mandl and G. Shaw, 'Quantum Field Theory', (1993) John Wiley & Sons, New York.

[8] N. Cabibbo, 'Unitary Symmetry and Leptonic Decays', Phys.Rev.Lett.10(1963)531.

[9] UA1 Collaboration, 'Experimental Observation of Lepton Pairs of Invariant Mass around 95GeV at the CERN SPS Collider', Phys.Lett.B(1983)126:398-410.

[10] UA1 Collaboration, 'Experimental Observation of Isolated Large Transverse Energy Electrons with Associated Missing Energy at $\sqrt{s} = 540\text{GeV}$', Phys.Lett.B(1983)122:103-116.

[11] UA2 Collaboration, 'Evidence for $\text{Z}^0 \rightarrow e^+e^-$ at the CERN Anti-P P Collider', Phys.Lett.B(1983)129:130-140.

[12] UA2 Collaboration, 'Observation of Single Isolated Electrons of High Transverse Momentum in Events with Missing Transverse Energy at the CERN Anti-P P Collider', Phys.Lett.B(1983)122:476-485.

[13] Particle Data Group, 'Review of particle physics', Eur.Phys.J.C3(1998)1-794.

[14] CERN Yellow Report. 'Physics at LEP2 volume 1', CERN 96-01.

[15] CERN Yellow Report. 'Physics at LEP2 volume 2', CERN 96-01.

[16] B.R. Webber, 'Colour Reconnection and Bose-Einstein effects', J.Phys.G: Nucl.Part.Phys.24(1998)287-296.

[17] ALEPH Collaboration, 'Measurement of the W mass and width in e^+e^- collisions at 189GeV', Euro.Phys.J.C17(2000)241-261.

[18] ALEPH Collaboration, 'GALEPH Manual', maintained by Florence Ranjard, on-line location: http://alephwww.cern.ch/LIGHT/galeph.html

[19] CERN Library, 'GEANT Manual', on-line location: http://wwwinfo.cern.ch/asdoc/geant_html3/geantall.html

[20] ALEPH Collaboration, 'JULIA Manual', on-line location: http://alephwww.cern.ch/ALEPHGENERAL/jul/doc/html/julia.html

[21] ALEPH Collaboration, 'ALPHA - ALEPH Physics Analysis Package Users Guide', ALEPH 99-087 (1999) SOFTWR 99-001.

[22] T. Sjöstrand, 'High-Energy Physics event generation with PYTHIA 5.7 and JETSET 7.4', Comp.Phys.Commun.82(1994)74.

[23] B. Andersson, G. Gustafson, G. Ingelman and T. Sjöstrand, 'Parton fragmentation and string dynamics', Phys.Rep.97(1983)31.

[24] Torbjörn Sjöstrand and Valery Khoze, 'Does the W mass reconstruction survive QCD effects?', Phys.Rev.Lett.72(1994)28-31.

[25] Valery Khoze and Torbjörn Sjöstrand, 'Soft-particle spectra as a probe of interconnection effects in hadronic W^+W^- events', Euro.Phys.J.C6(1999)271-284.

[26] M. Skrzypek *et al*, 'Monte Carlo program KORALW 1.02 for W pair production at LEP2/NLC energies with Yennie-Frautschi-Suura exponentiation', Comput.Phys.Commun.94(1996)216-248.

[27] F.A. Berends, R. Pittau and R. Kleiss, 'EXCALIBUR - a Monte Carlo program to evaluate all 4-fermion processes at LEP 200 and beyond', Comput.Phys.Commun.85(1995)437.

[28] F.A. Berends, R. Pittau and R. Kleiss, 'All electroweak four fermion processes in electron-positron collisions', Nucl.Phys.B424(1994)308-342.

[29] G. Marchesini, B.R. Webber, G. Abbiendi, I.G. Knowles, M.H. Seymour and L. Stanco, 'HERWIG, a Monte Carlo event generator for simulating hadron emission reactions with interfering gluons, Version 5.1', Comput.Phys.Commun.67(1992)465.

[30] Leif Lönnblad, 'ARIADNE version 4, a program for simulation of QCD-cascades implementing the Colour Dipole Model', Comput.Phys.Commun.71(1992)15.

[31] G. Gustafson, 'Dual description of a confined colour field', Phys.Lett.B175(1986)453.

[32] G. Gustafson and U. Pettersson, 'Dipole formulation of QCD cascades', Nucl.Phys.B306(1988)746.

[33] G. Gustafson and J. Häkkinen, 'Colour interference and confinement effects in W pair production', Z.Phys.C.64(1994)659.

[34] Leif Lönnblad, 'Reconnecting coloured dipoles', Z.Phys.C.70(1996)107.

[35] V.S. Fadin, V. Khoze and A.D. Martin, 'How suppressed are the radiative interference effects in heavy unstable particle production?', Phys.Lett.B320(1994)141.

[36] G. Gustafson, U. Pettersson and P. Zerwas, 'Jet final states in W pair production and colour screening in the QCD vacuum', Phys.Lett.B209(1988)90.

[37] Jorgen Beck Hansen, Private communications.

[38] John Ellis and Klaus Geiger, 'Space, time and colour in hadron production via $e^+e^- \to \mathrm{Z}^0$ and $e^+e^- \to \mathrm{W}^+\mathrm{W}^-$',Phys.Rev.D54(1996)1967.

[39] John Ellis and Klaus Geiger, 'Signatures of parton exogamy in $e^+e^- \to \mathrm{W}^+\mathrm{W}^- \to \mathit{hadrons}$', Phys.Lett.B404(1997)230.

[40] Alois Putzer, talks on 'The VNI Monte Carlo', to the ALEPH Colour Reconnection Group.

[41] N.K. Watson '$\mathrm{W}^+\mathrm{W}^-$ Hadronic decay properties', talk to ICHEP98 Vancouver, 23-29 July 1998.

[42] ALEPH Collaboration, 'Charged particle multiplicity in W pair decays', submitted to ICHEP98, Vancouver, 23-29 July 1998, ALEPH 98-066 CONF 98-036.

[43] OPAL Collaboration, 'W$^+$W$^-$ event Properties at $\sqrt{s} = 183$GeV', submitted to ICHEP98, Vancouver, 23-29 July 1998, OPAL note PN365.

[44] OPAL Collaboration, 'Colour Reconnection Studies in $e^+e^- \rightarrow$W$^+$W$^-$ at $\sqrt{s} = 183$GeV', Phys.Lett.B453(1999)153-168.

[45] L3 Collaboration, 'Study of charged particle production in hadronic and semi-leptonic WW events at $\sqrt{s} = 183$GeV', submitted to ICHEP98, Vancouver, 23-29 July 1998, L3 note 2278.

[46] DELPHI Collaboration, 'Charged particles from the hadronic decay of W bosons and in $e^+e^- \rightarrow q\bar{q}$ at 183GeV, submitted to ICHEP98, Vancouver, 23-29 July 1998, DELPHI note 98-16 CONF 117.

[47] Klaus Geiger, 'VNI 3.1: MC simulation program to study high-energy particle collisions in QCD by space-time evolution of parton cascades and parton-hadron conversion', Comput.Phys.Commun.104(1997)70.

[48] B. Andersson, P. Dahlkvist and G. Gustafson, 'An infrared stable multiplicity measure on QCD parton states', Phys.Lett.B214(1988)604.

[49] B. Andersson, P. Dahlkvist and G. Gustafson, 'On local parton hadron duality. 1. Multiplicity', Z.Phys.C44(1989)455.

[50] Gerald Rudolph, Private communications.

[51] ALEPH Collaboration, 'The ALEPH Handbook Volume 1', edited by C.K.Bowdery, ISBN 92-9083-072-7.

[52] ALEPH Collaboration, 'The ALEPH Handbook Volume 2', edited by C.K.Bowdery, ISBN 92-9083-073-5.

[53] ALEPH Collaboration, 'Performance of the ALEPH detector at LEP', Nucl.Instrum.Meth.A360(1995)481-506

[54] ALEPH Collaboration, 'Measurement of the W mass in e^+e^- collisions at 183GeV', Phys.Lett.B453(1999)121-137.

[55] ALEPH internal note, 'WW cross-section and W branching ratios at 183GeV', (1998) ALEPH/98-078.

[56] Evelyn Thomson, 'Measurements of the W boson mass from $e^+e^- \rightarrow$ W$^+$W$^- \rightarrow l\overline{\nu}q\overline{q}$ events with the ALEPH detector', PhD thesis, University of Glasgow (1998).

[57] Imma Riu, 'Measurement of the W mass from the WW $\rightarrow q\overline{q}q\overline{q}$ channel with the ALEPH detector', PhD thesis, Universitat Autonoma de Barcelona, Barcelona (1998).

[58] ALEPH Collaboration, 'Measurement of W pair production in e^+e^- collisions at 183GeV', Phys.Lett.B453(1999)107-120.

[59] ALEPH Collaboration, 'Measurement of the W mass in e^+e^- collisions at production threshold', (1999) CERN-PPE/97-025.

[60] J. Allison, 'Multiquardric radial basis functions for representing multidimensional High-Energy Physics data', Comp.Phys.Commun.(1993)177.

[61] ALEPH's LEP2 Luminosity page, maintained by Brigitte Bloch-Devaux, http://alephwww.cern.ch/~sical/Wlumi.

[62] Glen Cowan, Private communications.

[63] ALEPH collaboration, 'QCD studies with e^+e^- annihilation data from 130 to 183GeV', submitted to ICHEP98, Vancouver, 23-29 July 1998, ALEPH 98-025 CONF 98-014.

[64] ALEPH collaboration, 'Studies of Quantum Chromodynamics with the ALEPH detector', Phys.Rep.294(1998).

[65] Bolek Pietrzyk, Private communications.

[66] ALEPH collaboration, 'Study of fermion pair production in e^+e^- collisions at 130-183GeV', submitted to ICHEP98, Vancouver, 23-29 July 1998, ALEPH 98-060 CONF 98-031.

[67] ALEPH collaboration, 'Study of fermion pair production in e^+e^- collisions at 130-183GeV', Euro.Phys.J.C.12(2000)183-207.

[68] ALEPH collaboration, 'Fermion pair production in e^+e^- collisions at 189GeV and limits on physics beyond the Standard Model', submitted to the 1999 winter conferences, ALEPH 99-018 CONF 99-013.

[69] Evelyn Thomson, Private communications.

[70] Rob Edgecock, Private communications.

[71] Helenka Przysiezniak, Private communications.

[72] ALEPH collaboration, 'Measurement of the charged particle multiplicity distribution in hadronic Z^0 decays', Phy.Lett.B.273(1991)181-192.

[73] ALEPH collaboration, 'A study of Bose-Einstein correlations in e^+e^- annihilations at 91GeV', Z.Phys.C.54(1992)75-85.

[74] ALEPH Collaboration, 'The ALEPH Handbook Volume 1', edited by C.K.Bowdery, ISBN 92-9083-072-7, Chap.5.11.6.

[75] Ursula Becker, talks on 'The Event Multiplicities of Z^0 Decays', to the ALEPH Colour Reconnection Group.

[76] Glen Cowan, 'Statistical Data Analysis', (1998) Oxford University Press, Oxford.

[77] B. Foster, 'Electron-Positron Annihilation Physics', Adam Hilger Publishing, Bristol.

[78] Alain Blondel, e-mail communication, 10^{th} October 1997.

[79] ALEPH WW jet pairing page, maintained by Ann Moutoussi, http://alephwww.cern.ch/~moutouss/ww/wpairs.ht

[80] ALEPH WW kinfit page, maintained by Andrea Valassi, http://alephwww.cern.ch/~valassi/kinfit/

[81] Matthew Donald Kennedy Chalmers, 'Measurements of the mass of the W boson in the $W^+W^- \to q\overline{q}q\overline{q}$ channel with the ALEPH detector', PhD thesis, University of Glasgow (2000).

[82] Ann Moutoussi, Private communications.

[83] Professor Terry Sloan, Private communications.

[84] L3 Collaboration, 'Colour Reconnection Studies in $e^+e^- \to W^+W^-$ Events at $\sqrt{s}$ =189GeV' submitted to ICHEP99, Tampere, Finland, 15-21 July 1999, L3 Note 2406.

[85] N.A. Robertson, 'Final State Interactions in WW events at LEP2', talk to the International Symposium on Multiparticle Dynamics (ISMD99), Brown University, Providence, RI, USA, August 9-13, 1999.

[86] J.D. Bjorken and S.J. Brodsky, 'Statistical model for electron - positron annihilation into Hadrons', Phys.Rev.D1(1970)1416.

[87] G.C Fox and S. Wolfram, 'Event shapes in e^+e^- annihilations', Nucl.Phys.B149(1979)413.

[88] G.C Fox and S. Wolfram, 'Observables for the analysis of event shapes in e^+e^-', Phys.Rev.Lett.41(1978)1581.